SELF-CLEANING SOLAR CELL COATINGS BASED ON TiO2/ZnO NANOCOMPOSITE PHOTOCATALYST

A THESIS SUBMITTED TO

THE GRADUATE SCHOOL OF NATURAL AND APPLIED SCIENCES

OF

ANKARA UNIVERSITY

by

Mohanad Hasan Hamdan AL-SAEDI

IN PARTIAL FULFILLMENT OF THE REQUIREMENTS

FOR THE DEGREE OF

MASTER OF SCIENCE

IN

ENERGY ENGINEERING

ANKARA
2023

ÖZET

Yüksek Lisans Tezi

TiO_2/ZnO NANOKOMPOZİT FOTOKATALİZÖRE DAYALI KENDİ KENDİNİ TEMİZLEYEN GÜNEŞ PİLİ KAPLAMALARI

Mohanad Hasan Hamdan AL-SAEDI

Ankara Üniversitesi
Fen Bilimleri Enstitüsü
Enerji Mühendisliği Anabilim Dalı

Danışman: Doç. Dr. Özcan KÖYSÜREN

TiO_2 ve ZnO nanoparçacıkları, sol-jel yöntemi kullanılarak başarıyla hazırlanmıştır. Damla kaplama yöntemiyle farklı ZnO içeriğine sahip bir dizi TiO_2/ZnO kompozit filmi hazırlanmıştır. TiO_2/ZnO kompozit filmlerdeki ZnO içeriğinin yapısal, morfolojik ve optik özellikler üzerindeki etkisi araştırılmıştır. TiO_2 ve ZnO filmlere ait XRD difraktogramı üzerinde görülen kırınım piklerinin, her iki yarıiletkene ait standart kartlarda verilen kırınım pikleri ile aynı kırınım açılarında olması nedeniyle; XRD ölçümleri, film numunelerini hazırlamak için uygulanan kaplama tekniğinin, hem TiO_2 hem de ZnO filmleri için malzemelerin yapısını etkilemediğini göstermektedir. FTIR analizi ile TiO_2, ZnO ve kompozit film numunelerinin başarılı bir şekilde sentezlendiği kanıtlanmıştır. FESEM analizi, TiO_2 nanopartiküllerinin ZnO nanopartiküllerinden daha büyük olduğunu göstermiştir. Bu durum ZnO filminin TiO_2 filminden daha pürüzsüz görünmesini sağlamıştır. ZnO'in küçük parçacıklarının TiO_2 filminin gözeneklerini kapatması ve filmi daha pürüzsüz hale getirmesi, bu iki nanopartikülün karıştırılmasının iyi sonuçlarını göstermiştir. TiO_2 filmi ve $0.75TiO_2/0.25ZnO$ kompozit filmi dolaylı bant aralığı geçişi gösterirken, ZnO filmi ve geri kalan kompozit numuneler doğrudan bant aralığı geçişi göstermiştir. Kendi kendini temizleme ve fotokatalitik etkiler için önemli ve gerekli olan sıfıra yakın su temas açısına, 15 dakikalık ışık uygulaması ile çok yaklaşılmıştır. Film kaplı güneş pilinin I-V karakteristik eğrisi, kaplanmamış güneş pilininki ile karşılaştırıldı, en iyi verim (10.529), $0.25TiO_2/0.75ZnO$ kompozit film ile kaplanmış güneş pili tarafından elde edilmiştir.

May 2023, 92 sayfa

Anahtar Kelimeler: Kendi kendini temizleyen kaplamalar, güneş hücreleri, fotokatalizör, nanokompozit

ABSTRACT

Master's Thesis

SELF-CLEANING SOLAR CELL COATINGS BASED ON TiO_2/ZnO NANOCOMPOSITE PHOTOCATALYST

Mohanad Hasan Hamdan AL-SAEDI

Ankara University
The Graduate School of Natural and Applied Sciences
Department of Energy Engineering

Supervisor: Assoc. Prof. Dr. Özcan KÖYSÜREN

TiO_2 and ZnO nanoparticles are successfully prepared using a sol-gel method. A series of TiO_2/ZnO composite films with varying ZnO content were prepared by the drop casting method. The influence of the ZnO content in TiO_2/ZnO composite films on the structural, morphological and optical properties was investigated. The XRD measurements indicate that the coating technique to prepare film samples did not affect the structure of the materials for both TiO_2 and ZnO films since the diffraction peaks appeared on the pattern in the same peak position as they appear in the standard cards for TiO_2 and ZnO powders. FTIR analysis confirmed the successful synthesis of TiO_2, ZnO and composite film samples. FESEM microscopy showed that the TiO_2 nanoparticles were larger than the ZnO nanoparticles, making the ZnO film appear smoother than the TiO_2 film. It indicated the good results of mixing these two nanoparticles because the small particles of ZnO closed the pores of the TiO_2 film and the film appeared more smother. The TiO_2 film and the $0.75TiO_2/0.25ZnO$ composite film exhibited indirect band gap transition while the ZnO film and the remaining composite samples showed direct band gap transition. The water contact angle was approached to almost zero angle with 15 min of illumination, which is important and necessary for self-cleaning and photocatalytic effects. The I-V characteristic curve of the film coated solar cell was compared with that of the uncoated solar cell. The best efficiency (10.529) was obtained by the solar cell coated with the $0.25TiO_2/0.75ZnO$ composite film.

May 2023, 92 pages

Key Words: Self-Cleaning coatings, solar cells, photocatalyst, nanocomposite

ACKNOWLEDGEMENTS

I would like to acknowledge and give all my best thanks to my supervisor Dr. Özcan KÖYSÜREN who made this achievement possible. I felt his full trust and guidance through the experimental work and writing of the thesis. I am so grateful we worked together.

I would also like to thank the employees of the Department of Energy Engineering at Ankara University for providing me with the opportunity to receive graduate education.

I would also like to thank the Iraqi Ministry of Environment and my colleagues because they also supported the successful completion of this study.

I am so grateful to Dr. Ameer F. Abulameer for his efforts and time that spent with me.

I would like to express my sincere love to my family especially my father, mother, brothers, sisters and my wife, who provided support and assistance throughout the research. I want to say that I love you forever and this achievement is dedicated to you.

I would also like to thank my friends, especially Mohammed, Sameer, Wissam, Ayad, Ahmed and Iman, who gave me support, advice and hope, thank you very much for everything they have given me.

Mohanad Hasan Hamdan AL-SAEDI
Ankara, May/ 2023

LIST OF CONTENTS

SYMBOLS AND ABBREVIATIONS

Ag	Silver
Au	Gold
Ce	Cerium
Co	Cobalt
Cr	Chrome
Dy	Dysprosium
Eu	Europium
Fe	Iron
Gd	Gadolinium
Ir	Iridium
ITO	Indium tin oxide
Mn	Manganese
Mo	Molybdenum
Nb	Niobium
Nd	Neodymium
Os	Osmium
PC	Personal computer
pH	Acidic function
Pr	Praseodymium
Ru	Ruthenium
Sm	Samarium
Sn	Tin
Ta2O5	Tantalum pentoxide
V	Vanadium
W	Tungsten
Yb	Ytterbium
Zn	Zinc
μm	Micrometer
μL	Microliter
A	Amper
A/d	Absorbance per film thickness
AOP	Advanced oxidation process
Approx.	Approximately
ARCs	Antireflection coatings
C	Celsius temperature
CAH	Contact angle hysteresis
CB	Conduction band
CdS	Cadmium sulfide
CdTe	Cadmium telluride
CIGS	Copper-Indium-Gallium-Diselenide

CIS	Copper-Indium-Diselenide
Cu	Copper
CZ	Czochralski
DSSC	Dye sensitized solar cell
e	Electron
Eg	Energy gap
Ep	Energy of an absorbed or emitted phonon
eV	Electron volt
F.F	Fill factor
Fe2O3	Ferric oxide
FESEM	Field Emission Scanning Electron Microscopy
FTIR	Fourier Transform Infrared
GaAs	Gallium arsenide
gm	Gram
h	Hole
h, k, l	Miller indices
H2O	Water
H2SO4	Sulfuric acid
Hetero-	heterogeneous
Homo-	Homogenous
h	Plank constant
Y	Frequency
I	Transmitted photon
Im	Maximum current
InP	Indium phosphide
Io	Incident photon
IR	Infrared ray
Isc	Short-circuit current
I-V	Current-Voltage
JCPDS	International Centre for Diffraction Data
Jm	Maximum current density
k	Extinction coefficient
k	Wave vector
KeV	kilo electron volt
KOH	Potassium hydroxide
KV	Kilo volt
KWh	Kilo watt hour
La	Lanthanum
Lab	Laboratory
LSC	Luminescent Solar Concentrators
M	Meter
mg/m2	Milligram per square meter
min	Minute

ml	Milliliter
mm	Millimeter
mmol	Millimole
MW/m2	Megawatt per meter square
n	Refractive index
ɳ	Efficiency
NCs	Nanocomposites
NH4OH	Ammonium hydroxide
Ni	Nickel
n-i-p	Negative-Intrinsic-Positive
Nm	Nanometer
NPs	Nanoparticles
n-type	Negative type
O2	Oxygen dioxide
OPV	Organic photovoltaic
Pd	Palladium
Pin	Power input
p-i-n	Positive-Intrinsic-Negative
p-n junction	Positive-Negative junction
Pout	Power output
Pt	Platinum
p-type	Positive type
PV	Photovoltaic
Rh	Ruthenium
SEM	Scanning electron microscopy
Si	Silicone
SiO2	Silicone dioxide
SNO2	Tin oxide
SO42−	Sulfur tetroxide
SOH	Superhydrophobic surface
TEM	Transmission electron microscopy
TiCl4	Titanium tetrachloride
TiO2	Titanium dioxide
UV	Ultra violet ray
VB	Valence band
Vm	Maximum voltage
Voc	Open circuit voltage
W	Watt
W/m2	Watt per square meter
Wt	Weight
XRD	X-ray Diffraction

$ZnC_4H_6O_4$	Zinc acetate
ZnO	Zinc oxide
ZnS	Zinc sulfide
ZrO_2	Zirconium oxide
α	Absorption coefficient
εi	Imaginary part of the dielectric constant
εr	Real part of the dielectric constant
θa	Advanced theta angle
θe	Theta angle
θr	Receding theta angle
λ	Wavelength symbol

LIST OF FIGURES

,

LIST OF TABLES

1. GENERAL INTRODUCTION

1.1 Introduction

Because of pollution caused by fossil fuel such as oil, natural gas and coal, and with increase of world population and with decrease of fossil fuel, it become necessary to seek on a renewable energy source like wind, hydrological, geothermal, tidal and solar energy sources. Solar energy is most abundant compared with other renewable energy sources. Sun send huge amount of power to the earth nearly $4000x10^{12}$ KWh, and the light intensity reaching the earth's surface is considered to be 1000 W/m^2 everywhere, which is 10,000 times more than the energy consumed by the world in a year. When sun rays reach to atmosphere, 26% of them are reflected and dispersed in the atmosphere and clouds (Ganesh et al. 2012, Smestad et al. 2020).

Depending on many factors, a photovoltaic (PV) module in a dusty environment can accumulate 80-300 mg/m^2 of dust per day, and each 100 mg/m^2 of dust accumulation leads to an additional output loss of 0.4-0.7%. A minimum of 20 mm of precipitation is required to clean the surface of PV systems, otherwise the systems will continue to lose power due to dust and soil (Guo et al 2013, Appasamy et al, 2020).

The cleaning methods of solar cell panels are summarized as natural methods, mechanical methods, electrostatic methods and self-cleaning nano-surfaces. The natural methods employ to remove the dusts using the wind power and gravitation as well as the scour of the rainwater. The mechanical methods use brushing, blowing, vibrating and ultrasonic driving. The third method for cleaning (dusts-removing) is electrostatic which is a simple electric method, and the last method is self-cleaning nano-film, which is made of super-hydrophilicity material or super-hydrophobic material. It means that the self-cleaning mechanism of the nano-film involve two strategies. The self-cleaning technology for solar cell array can promote the efficiency of electric power obtained and protect the solar cell (He 2014, Appasamy et al. 2020).

Photocatalysis is known as an effective process for converting any kinds of organic pollutants into small molecules like carbon dioxide and water in the presence of a photocatalyst. The most widely used heterogeneous photocatalysts are transition metal oxides and semiconductors like TiO_2, ZnO, SnO_2 and CeO_2 (Siwinska-Stefanska et al. 2018, Livage et al. 1988, Liao et al. 2004, Agbe et al. 2019).

Titanium dioxide is known as the most active among the transition metal oxides and semiconductors that have been studied. It is easy to synthesize TiO_2 nanoparticles in different crystal structures. In addition, TiO_2 is relatively cheap, non-toxic, easily UV-activated and insoluble in most reaction environments. It is also both chemically and photochemically stable. However, its photocatalytic application is limited due to its narrow photocatalytic region ($\lambda < 400$ nm) and its ability to be induced by only a small fraction (5%) of incident solar irradiation. The reason for the limited application of TiO_2 is its relatively large band gap (~3.2 eV) (Siwinska-Stefanska et al. 2018, Barakat et al. 2016). Many recent studies have focused on modifying the morphology and crystalline structure of TiO_2 to improve its photocatalytic activity. Modification may be performed by adding transition metal ions (Wang et al. 2017b), doping with non-metals (He et al. 2014), and using hybrid semiconductors such as TiO_2-ZnO (Chen et al. 2008) and TiO_2-SiO_2 (Yu et al. 2001). To increase the response of TiO_2 to solar radiation, it is coupled with ZnO (Chen et al. 2008), ZrO_2 (Qu et al. 2014) and SrO (Han et al. 2007), respectively. It has been proven that the formation of oxide hybrids is an appropriate tool for improving the photocatalytic ability of TiO_2 materials (Siwinska-Stefanska et al. 2018).

ZnO has been considered as an alternative photocatalyst material to TiO_2 as they have similar features as a semiconductor. In addition, ZnO possesses a higher electron mobility and longer photoinduced electron lifetime than that of TiO_2, which is beneficial for photocatalytic degradation of dyes (Huang et al. 2013). However, it can only absorb a very small ultraviolet part of the solar spectrum because of its wide band gap, which is similar to TiO_2. Therefore, it is essential to develop new photocatalysts with a smaller band gap to harvest visible light (Chen et al. 2009, Zhao et al. 2015).

1.2 Scope of the Study

In this study, TiO_2 and ZnO nanoparticles were prepared by sol-gel methods and then they were mixed with different ratios of (TiO_2/ZnO) weight percent (1/0, 0.75/0.25, 0.5/0.5, 0.25/0.75 and 0/1). As a photocatalyst material, the prepared samples were utilized for self-cleaning layer coated on solar cells, and the optimum composition of TiO_2/ZnO systems, providing the highest efficiency of the silicon solar cell, was investigated.

1.3 Objective of the Study

The study aims to investigate the effect of TiO_2/ZnO composition of film coatings on the efficiency of standard silicon solar cell. The potential of the prepared TiO_2/ZnO films to be used as a self-cleaning layer on standard silicon solar cells has been studied.

2. LITERATURE REVIEW

2.1 Concept of the Photovoltaic Cell

The photovoltaic (PV) effect is the basis for converting the sunlight into electricity in photovoltaic or solar cells. The PV effect is simply described as follows: Light, a kind of pure energy, enters a solar cell and gives enough energy to valence band electrons to release them. A built-in potential barrier in the solar cell acts on these photoinduced electrons to produce a voltage (the so-called photovoltage) that can be utilized to drive current through a circuit (Anonymous 2023c). More specifically, a PV cell includes a barrier formed by opposite electrical charges facing each other on either side of a dividing line. This potential barrier selectively separates the photoinduced electrons and holes, transferring more electrons to one side of the cell and more holes to the other. The specified mobile charge carriers, electrons and holes, which are separated, are less likely to recombine again and lose their electrical energy. This charge separation creates a voltage difference between both ends of the cell that can be used to drive electric current in an external circuit (Anonymous 2023c, Hersch and Zweibel, 1982).

The photovoltaic effect remained a laboratory curiosity from 1839 until 1959, when the first silicon solar cell was developed at Bell Laboratories (Chapin et al. 1954). It already had an efficiency of 6%, which was rapidly increased to 10%. The main application of the photovoltaic technology has been a power source for space applications for many years. Terrestrial application of photovoltaic (PV) systems developed very slowly. But still, PV systems fascinated not only the scientists, but also the general public. Its strong points can be summarized as: direct conversion of solar radiation into electricity energy, no mechanical moving parts on it, no noise, low temperature, no pollution, PV modules have a very long lifetime, and the energy source, which is the sun, is free, ubiquitous and inexhaustible (Anonymous 2023b, Slade 2003).

For real-world use, solar cells are packaged into modules including either a number of crystalline Si solar cells linked in series or layer of thin-films which are also internally series connected. The module has two purposes: It protects the single solar cell from the

ambient conditions and it supplies a higher voltage than a single cell, providing only a voltage of less than 1 Volt (Anonymous 2023b, Slade 2003).

Solar cell technology has benefited greatly from the high standard of silicon based technology, which was originally developed for transistors and later for integrated circuits. Also, the quality and availability of single crystal silicon of high purity has been important in terms of its application in the solar cell technology. In the first years, only single crystals grown through the Czochralski (Cz) method were utilized for solar cells. This single crystal still plays an important role in the photovoltaic industry. As the cost of silicon is a significant proportion of the cost of a solar cell, great efforts have been made to reduce this cost (Dietze et al. 1981).

The visual appearance of modules made of thin film makes them attractive for facade applications. In addition to silicon, there are many other possible solar cell materials satisfying the condition of light absorption and are therefore appropriate for thin film solar cells. They belong to the class of compound semiconductors like GaAs or InP, which are III–V compounds according to their position in the periodic table. Other important groups are II–VI and I–III–VII compounds, which have four bonds per atom similar to the elemental semiconductors. It is clear that an almost infinite number of compounds could be considered as a solar cell material. From the mostly empirical search, only very few promising materials have emerged. Foremost are copper indium diselenide (CIS) and cadmium telluride (CdTe). As early as the 1960s, cadmium sulfide/copper sulfide solar cells were being developed (Goetzberger and Hoffmann 2005). Problems with low efficiency and insufficient stability prevented further investigation of this material.

2.2 Generations of Solar Cells

PV cell technologies are usually classified into three generations, depending on the basic material used and the level of commercial maturity as shown in Figure 2.1.

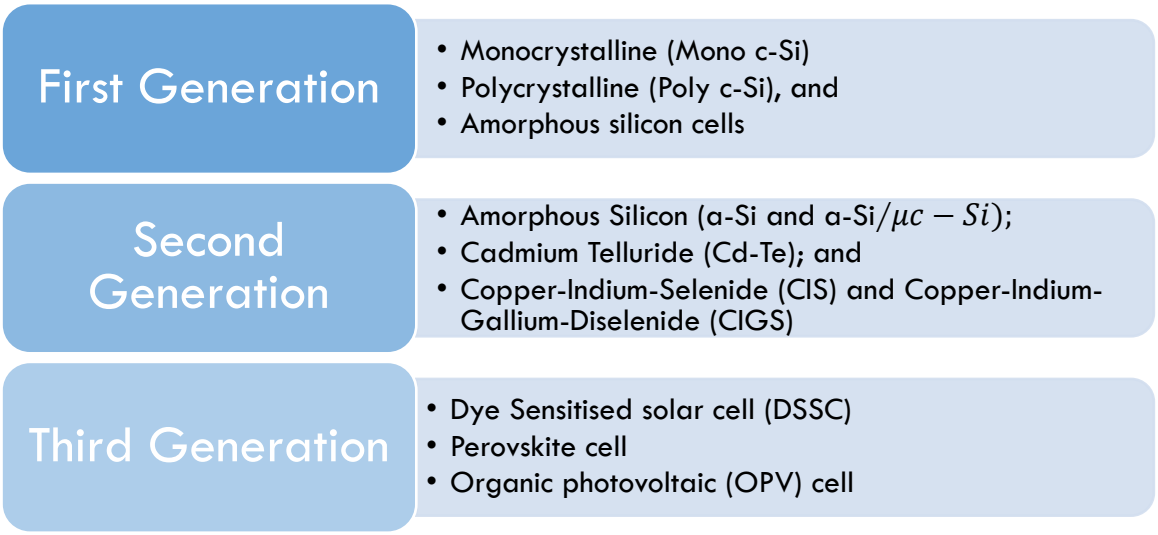

Figure 2.1 Classification of PV cells

2.3 Structures of Solar Cells

The structure of a solar cell device depends on the limitations of the used materials. There are four basic designs commonly used with materials:

1. Homo-junction.
2. Hetero-junction.
3. p-i-n /n-i-p.
4. Multi-junction.

2.3.1 Homo-junction

Crystalline silicon is the elementary example of a homo-junction cell. The crystalline silicon material is changed where one side is p-type, so that the majority charge carries are holes, and another side is n-type, where the majority charge carries are electrons. The p-n junction should be such that the biggest amount of light is absorbed near it. The free holes and electrons generated by light deep in the silicon diffuse to the p-n junction to generate a current if the silicon has sufficient high quality and purity. Some aspects of the homo-junction design, given below, can be altered to increase the conversion efficiency (Um and Kim 2014):

- Depth of the p-n junction under the cell's surface.
- Distribution and amount of dopant atoms on either side of the p-n junction.
- Purity and crystallinity of the silicon.

2.3.2 Hetero-junction

With the benefit of high efficiency, stationary and cost-effective, thin film solar cell, based on a hetero-junction structure, is a powerful candidate for renewable energy. The top layer and the bottom layer in a hetero-junction device have different tasks. The top layer is a high band gap material chosen for its light transmittance. The top layer allows nearly all of the incoming light to reach the bottom layer, where a low-bandgap material easily absorbs light most of the incoming photons present in the sunlight. Then, this light generates holes and electrons very near the junction, which will help to effectively separate the holes and electrons before they can recombine. Hetero-junction devices have advantage over homo-junction devices, where homo-junction require materials that can be doped both p and n type while hetero-junction do not require. Many photovoltaic materials can be doped either p-type or n-type, but not both. Due to hetero-junction devices do not have this constraint, many promising photovoltaic materials can be checked to produce optimal cells (Schmidt et al. 2007).

2.3.3 p-i-n and n-i-p

Amorphous silicon thin-film cells can be used to construct a p-i-n structure, while CdTe cells can be used to form a n-i-p structure. It consists of three regions; the middle is an undoped (intrinsic) semiconductor of sandwiched shape between p-region and n-region. This geometry constitutes an electric field between the n-type and p-type regions that extends across the middle intrinsic resistive region. Light generates free holes and electrons in the intrinsic region, which can be separated under the effect of the electric field. In the p-i-n type of amorphous silicon cell, the top layer is a p-type silicon, the middle layer is an intrinsic silicon, and the bottom layer is a n-type silicon. Amorphous silicon possesses many electrical defects in the atomic-level. Very little electrical current would flow if an amorphous silicon cell depends only on diffusion. However, in

a p-i-n cell, electrical current flows due to the mobile charge carriers, holes and electrons, generated with the effect of an electric field (Schmidt et al. 2007).

2.3.4 Multi-junction

This typical structure, also called a tandem or cascade cell, can provide higher amount of conversion efficiency by capturing a bigger portion of the solar spectrum. In the typical multi-junction cell, individual cells with different optical band gaps values are stacked one on top of another. Individual cells are stacked in such a way that the sunlight incidents first on the material with the largest optical band gap energy. Photons that are not absorbed in the first cell are transmitted to the second cell. The second cell absorbs the higher energy part of the remaining solar radiation while remaining transparent to the lower energy photons. These processes, which are selective absorption, continue until the last cell with the smallest band gap. Figure 2.2 demonstrates a multi-junction device with a many of individual single-junction cells in decreasing order of optical band-gap valus. The upper cell receives the high-energy photons of the incoming sunlight, and the upper cell passes the remaining photons to be absorbed by the lower band-gap cells (Anonymous 2023, Nakayama et al. 2008).

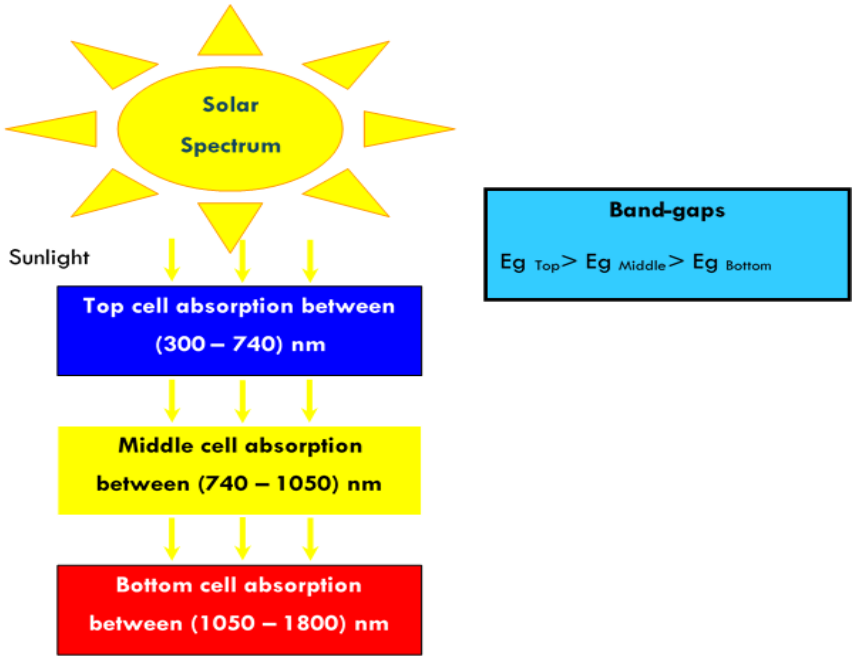

Figure 2.2 Multi-Junction Device (Anonymous 2023a)

2.4 Solar Spectrum

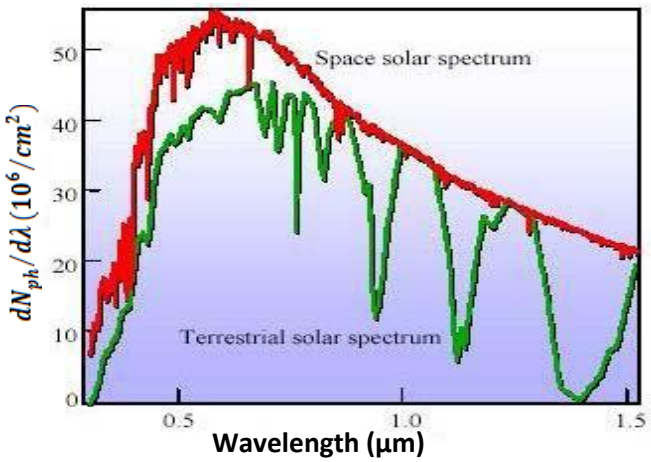

Figure 2.3 Spectrum of solar radiation in space and on the earth (Lansel 2010)

Solar cells are devices that are made of semiconductors. The solar cells are planned to generate electric power when they were subjected to electromagnetic radiation. The spectrum of radiation emitted by the sun is as shown in Figure 2.3. The distribution of solarlight in outer space looks like the theoretical radiation that provided by a black body. When light passes through the atmosphere, some of it is reflected or absorbed by gasses like water vapor and ozone layer. For this reason, the distribution of light in space is different from the distribution of light on the earth's surface (Figure 2.3). Since the solar spectrum is broad, the conversion efficiency of the solar cells is limited and it is less than 30%. To solve this problem, the whole spectrum needs to be considered as many spectral regions, and a cell whose band gap is tuned for each region needs to be used. The greater the number of spectral regions allowed, the higher the potential conversion efficiency (Lansel 2010).

2.5 Solar Radiation on the Earth's Surface

The intensity of radiation outside the Earth's atmosphere is called the extraterrestrial radiation. The total power density which is emitted by the Sun is very high (i.e., 64 MW/m^2), but only a small amount of it (0.001366 MW/m^2 or 1366 W/m^2) enters to Earth's atmosphere. Therefore, with an assumption that there is no huge absorption in

space, this value (1366 W/m^2) is called the solar constant (Brendel 2003). The annual mean of solar radiation that reaches to the Earth's surface is about 180 W/m^2, and it is a bit lower for oceans (170 W/m^2). The most intense portion of the spectral distribution exists in the area of visible light with a wavelength between 400 and 800 nm, and drops steeply to ultra-violet (UV) less than 400 nm, and the other side extends to infra-red (more than 800) radiation as shown in Figure 2.4 (Tanaka and Matsuo 2011).

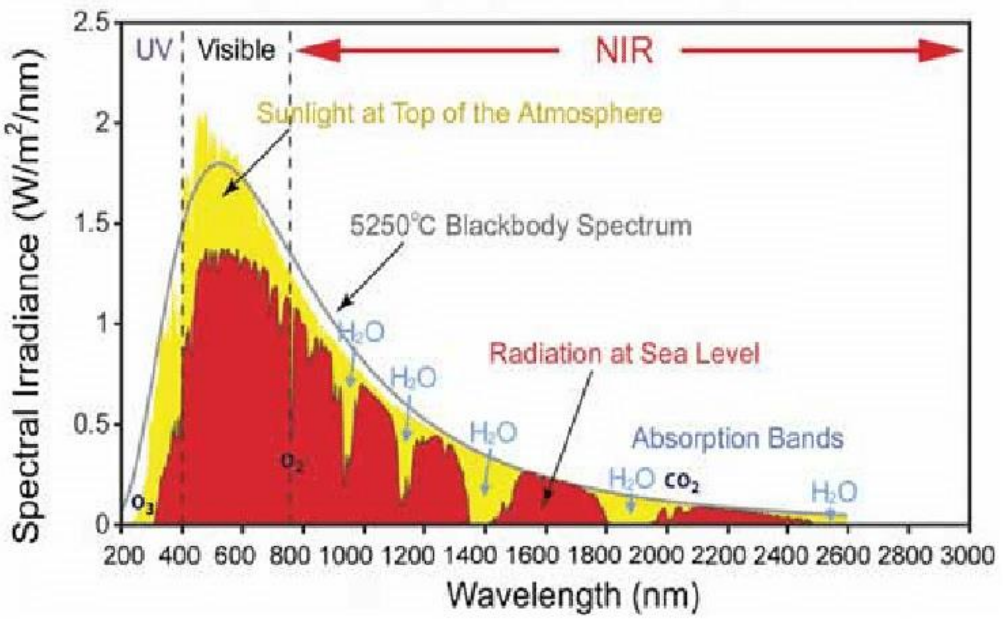

Figure 2.4 Spectral distribution of solar radiation (Tanaka and Matsuo 2011)

2.6 Reasons of Decreasing of PV Cell's Efficiency

There are two main reasons that cause the efficiency of a solar panel to decrease; dust and reflection (Elminir et al. 2006). Solar panels are installed in large area, where they are always exposed to dust storms, organic matters, water droplet and snow depending on location of installation. Any material deposited on top of the PV panels causes more reflection of incoming light, leading to a decrease in the intensity of the light penetrating the panel. With the decrease in the light intensity reaching the cell, the number of mobile charge carriers induced by the absorption of light decreases, leading to a decrease of the output power (Syafiq et al. 2018).

Large-scale PV installations already exist in many countries. These installations are usually located in open areas with a high intensity of sunlight. In these open areas, dry air and winds sweep dust into the air and deposit it on the surface of the solar panel. Just like dust on a glass window, this dust will can make a shadow on the solar panel, which will reduce the amount of sunlight that can get inside the solar panel and reduce the efficiency of that solar panel. It is expensive to use clean water for cleaning the solar panels because clean water tends to be scarce in areas that are rich with the sunlight. It is reported that the efficiency of converting solar power to electricity decreases by 40% when the solar panel is covered by a dust layer of 4 g/m^2 (Elminir et al 2006, Mazumder et al. 2007).

2.7 Principle of Self-Cleaning

To improve the efficiency of the solar cell and to protect the PV panel, different cleaning methods are used and they can be summarized as natural techniques, mechanical techniques, self-cleaning nano-film, and electrostatic techniques.

Wind power, gravitation and the scour of the rainwater are good examples for the natural techniques that are used to remove the dusts (Gaier et al. 1990). Gaier and Davis (1992) reported that this technique can be used for cleaning the solar cell array by turning the array to vertical or inclined position to remove the dusts easily when early morning, late evening, night and a rainy day. But the rotation of the large solar cell array is a hard problem to tackle (Gaier and Davis 1992).

The mechanical methods use brushing, blowing, vibrating and ultrasonic driving to remove the dusts. The brushing methods use a broom or brush that is driven by the machine and is designed just like windscreen-wiper. But there are some problems following this method:

1. The cleaning method is inefficient because of the small size and the strong stickiness of the dusts.

2. The harsh working environment of the solar cell makes the maintenance of the machine difficult. Due to the large area of the solar cell array, a powerful cleaning machine is required.
3. The surfaces of the solar cell could be damaged by the brush when wiping.

The blowing method uses wind power for cleaning the solar cell. However, it has low efficiency, high energy-consumption and poor maintenance of the blower.

Williams and his coworkers (2007) discussed the use of vibrating and ultrasonic driving to remove the dust particles from the surface of the PV panels. They have researched the vibration characterization of the self-cleaning solar panels with the effect of the piezoceramic actuation. Their study is yet at the initial stage of exploration (Williams et al. 2007).

Electrostatic dusts-removing is a simple electric method. Clark and his coworkers (2007) studied the dust mitigation strategy that works on the lunar surface. So, they came up with the suggestion that there are possibly two mechanisms of particles charging on moon, the first one is triboelectric charging and the second is photoemission of electrons from the surface of the particles by UV radiation. Because of the electrostatic forces, charged and uncharged dusts will be attracted to the panels if there are a high potential on the surface of the solar panels. The dust particles will be charged by the solar panels. Hence, the dust particles will possess the same electric charge as the solar panel, and the electrostatic forces between the dust particles and the solar panel will be repulsion. Finally, the dust particles will float away from the solar panels. This method cannot be used in PV system because of the effect of the rain on the earth (Clark et al. 2007).

In self-cleaning nano-film, hydrophilic and hydrophobic coatings are used. Both drive the same ultimate purpose which is to clean the solar panel from pollutants. Hydrophilic coatings are basically the opposite of hydrophobic coatings (He et al. 2014). The hydrophilic coating forms a uniform layer of water on the surface compared to the round droplet made by the hydrophobic coating as shown in Figure 2.5.

Figure 2.5 Hydrophilic panel (left) and hydrophobic panel (right)

2.8 Hydrophobic Surfaces

A lotus leaf has the property of “never wetting” or “ultra-ever dry”. Water can roll around freely on the leaf’s outer surface if it does not wet the surface. The water droplet will have an almost spherical shape, which ensures this rolling behavior. Self-cleaning property is introduced due to this rolling behavior and contaminants can be then removed by the rolling drop (Barthlott and Neinhuis 1997).

Hydrophobicity is commonly known as water repellency. This property is due to the non-polarity of the material. As water is polar, the non-polar surface of a material will repel water (Oliveira et al. 2015, Ahmad et al. 2018). Non-polar surfaces of materials do have an affinity with other non-polar surfaces of materials, which makes hydrophobic materials/coatings usable to attract alkanes (fats and oils), noble gasses and other homonuclear diatomic elements (Ahmad et al. 2018).

2.9 Hydrophilic Surfaces

Any substance that is readily dissolved in water is categorized as hydrophilic. This is the opposite for hydrophobic substances, in which substances are poorly soluble in water. The substance is defined as hygroscopic in terms of the ability of hydrophilic

solids to absorb water from the air. Table salt and sugar exhibit hydrophilic behavior, as they can be easily dissolved in water (Ahmad et al. 2018).

Another way to know whether or not a substance can be dissolved in water is that polar molecules can be dissolved in water as water is a polar molecule. This can also be applied to liquids spreading on surfaces. Surfaces with polar groups have an electric dipole or multipole moment. This is a qualitative method to define a hydrophilic surface or ‘‘polar spreads on polar’’ (Ahmad et al. 2018). Polar liquids like water prefer to spread on hydrophilic surfaces. The water contact angle on a hydrophilic surface is always less than 90° in a solid–water–air system. Any contact angle higher than 90° describes the system to have water on a hydrophobic surface (Ahmad et al. 2018).

When a solar panel is coated with a hydrophilic material, it forms a polar film coating onto the applied surface, which can attract polar molecules like as water. The film coating can attract and absorb moisture from the air, which can wet the surface. when the surface of the solar panel becomes wet, the film coating on the solar panel can start the photocatalytic degradation reactions. During the photocatalytic degradation reactions, water molecules are converted to active hydroxyl radicals (Ahmad et al. 2018).

2.10 Contact and Slide Angles

The terms of hydrophilic surface and hydrophobic surface have been widely utilized in literature for several years, describing opposite effects of the behavior of water on the surface of a solid. The hydrophilic surface of a material has strong affinity to water molecules, whereas the hydrophobic surface of a material repels water (Ahmad et al. 2018).

To classify the wetting behavior of fluid as hydrophilic or hydrophobic, it is necessary to measure the contact angle, which is an important indicator of the class of the material. The surface contact angle is the angle formed at the intersection of the liquid-

solid and liquid-vapor interface. Depending on the water droplet contact angle, the material is classified as:

1. Hydrophilic if the contact angle (θ_e) is less than 90°.
2. Superhydrophilic if contact angle (θ_e) is less than 5º.
3. Hydrophobic if the contact angle (θ_e) is between 90° and 150°.
4. Superhydrophobic if the contact angle (θ_e) is greater than 150°.

The strength of the liquid-liquid interaction increases, as the contact angle increases, making the material more hydrophobic (Ganesan et al. 2016, Wang et al. 2017a, Ahmad et al. 2018). The contact angle images for each wetting and non-wetting scenario is illustrated in Figure 2.6.

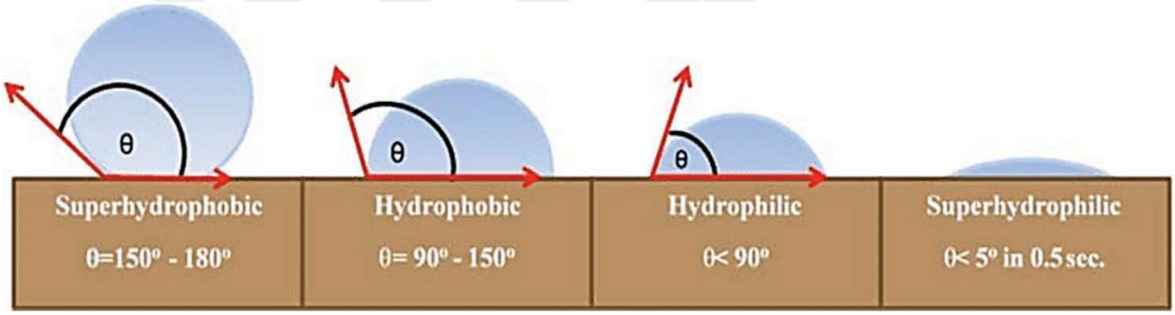

Figure 2.6 Schematic of water droplet's contact angle with different surface wettability (Abdulaziz et al. 2016, Ahmad et al. 2018)

The hydrophobicity feature can be characterized by three properties: contact angle of the water droplet (θ_e), hysteresis and the surface roughness. The water contact angle of a droplet describes the angle between the liquid-solid and liquid-vapor interfaces. The greater the contact angle becomes, the more hydrophobic the material is (Ahmad et al. 2018). Hydrophilic, hydrophobic and superhydrophobic (SHO) materials can either present the ''lotus effect'' or the ''petal effect''. The description of these specified effects depends on the contact angle hysteresis (CAH). The CAH defines the surface adhesion in which a small CAH value means weak surface adhesion. This can be attributed to the lotus and petal effect, as both effects contribute to superhydrophobic

feature but in the petal effect, the water droplets adhere very strongly to the surface and this is not the case in the lotus effect. Therefore, the CAH value is bigger in materials with the petal effect than in materials with the lotus effect (Wang et al. 2017a, Ahmad et al. 2018).

The CAH value can be obtained by measuring the advancing angle (θ_a) and the receding angle (θ_r). With a small CAH value ($\theta_a > \theta_r$), the water droplet can slides down on the inclined platform, which is known as lotus effect. With a high CAH ($\theta_a < \theta_r$), the water drop cannot slide down on the inclined platform, known as the petal effect. Figure 2.7 illustrates the water droplet with the specified advancing and receding angles on an inclined platform (Wang and Jiang 2007, Wang et al. 2017a, Ahmad et al. 2018). Both the CAH value and the water contact angle value are determined by surface heterogeneity and surface roughness. The surface roughness can be grouped into micro or nanoscale roughness, both of which help increase the contact angle of the water droplet. (Ganesan et al. 2016, Oliveira et al. 2015, Ahmad et al. 2018).

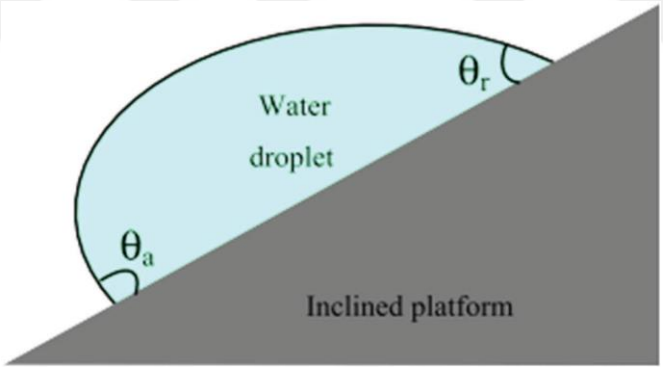

Figure 2.7 An experimental set-up of how the CAH can be measured (Ahmad et al. 2018)

2.11 Photocatalytic Activity

Photolysis is a kind of chemical reaction in which chemical compounds are degraded into smaller molecules by absorbing the incoming light. For the photocatalysis, the chemical compounds need to absorb the necessary energy from the photon of the incoming light (Khan and Yadav 2021). The interaction of the light with molecules

causes the molecules to degrade into simpler fragments (Cuerda et al. 2020). The processes of this method include UV/photolysis, UV/H_2O_2, and UV/ozone (Khan and Yadav 2021).

Photocatalysis is a heterogeneous advanced oxidation process (AOP) under light irradiation using a semiconductor photocatalyst that absorbs light. The photocatalysis differs from other treatment techniques because this process performs oxidation and reduction simultaneously (Khan and Yadav 2021, Mishra et al. 2017). There are many semiconductor materials like TiO_2, ZnO, Fe_2O_3, SnO_2, ZrO_2, CdS and ZnS that have been used as catalysts for the degradation of organic pollutants and dyes.

Photocatalysis is a photochemical reaction, where light activates the photocatalyst material to an excited state, leading to form mobile charge carriers. The photogenerated charge carriers, electron-hole pairs, react with surface adsorbed water and oxygen molecules, and convert them into active radicals. These active radicals then react with all kinds of organic compounds and convert them into harmless small molecules. The preferred photocatalytic reaction is one in which the catalyst returns to its original state after the reaction. Figure 2.8 shows a simplified photocatalytic degradation reaction (König 2013).

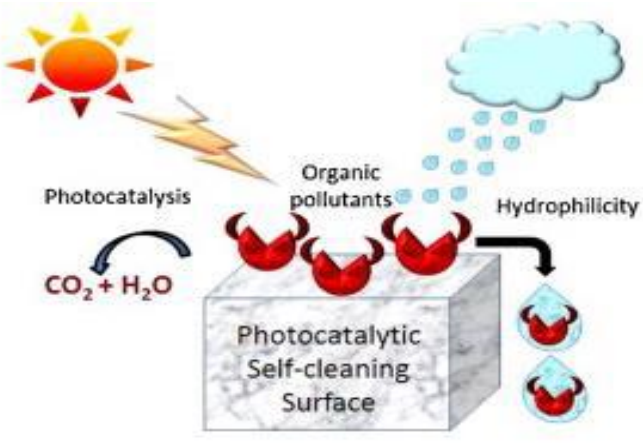

Figure 2.8 Photocatalytic reaction on a self-cleaning surface

Photocatalysis combines the photochemistry and the catalysis in which both light and a catalyst are required to initiate or accelerate a chemical transformation (Haider et al. 2011). The photocatalytic decomposition reactions start with the absorption of electromagnetic radiation of the incoming light, which leads to transfer of a valence band electron to the conduction band, resulting in formation of a hole in the valence band. Figure 2.9 is a schematic illustration of the photocatalytic degradation process. In this process, UV light radiation is utilized with the photon energy equal to or greater than the optical band gap energy of the material, such as TiO_2 ($h\nu \geq 3.20$ eV at $\lambda \leq 380$ nm). Then, electron-hole pairs, which are mobile charge carrier, are formed (Haider et al. 2011). The photoinduced electron and hole take part in the reduction and oxidation reactions, respectively. The photogenerated electron reduce surface adsorbed oxygen molecules to superoxide radical and the photogenerated hole oxidize surface adsorbed water molecules to hydroxyl radical. In the natural environment, the UV light is all around in the form of sunlight. The hydroxyl radicals have strong oxidation properties and have the ability to kill microorganisms, viruses and other organic contaminants. On the other hand, superoxide radicals can decompose organic materials (Martemucci et al 2022).

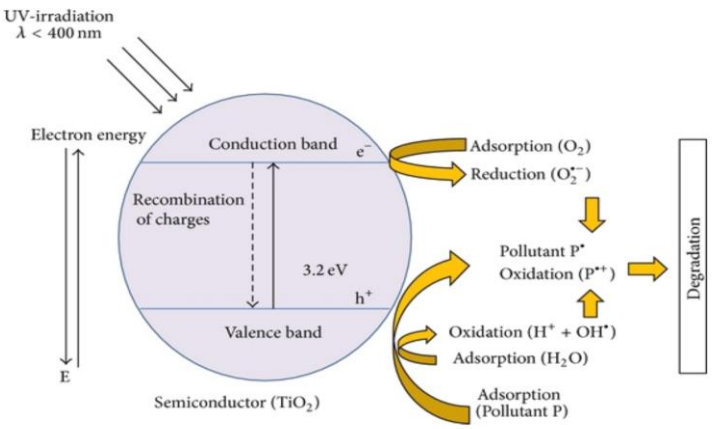

Figure 2.9 Principal photocatalytic process on the TiO_2 photocatalyst

In a case where the photogenerated electron-hole pairs are not separated through the reduction-oxidation reactions, recombination of the charge carriers takes place, and the energy is released in the form of heat. This causes a large decrease in the photocatalysis efficiency of the material (Kotani et al. 2001, Cho and Choi 2001). The electron-hole

recombination is a competitive reaction with hole-donor, electron-acceptor and electron-transfer reactions. The recombination can take place either on the surface or in the bulk of the photocatalyst material, which results in the release of heat or light. The recombination of the photogenerated electron-hole pairs is detrimental to the photocatalytic efficiency of the material as the redox properties of the semiconductor are quenched (Mills and LeHunte 1997, Nyamukamba 2011, Matsunaga 1985).

The photocatalytic efficiency of a photocatalyst material is affected by several factors like mass/concentration, light intensity and wavelength of the incoming light, pH and temperature of the reaction medium, the nature of photocatalyst materials, particle size, surface area, the adsorption nature and concentration of the substrate (Wong et al. 2010, Foster et al. 2011).

2.12 Titanium Dioxide (TiO_2) Photocatalyst

Titania (TiO_2) is an ideal semiconductor for terrestrial solar cell applications. It is chemically and physically stable, transparent, antireflective and capable of self-cleaning itself due to its superior physicochemical features, and TiO2 has been widely investigated in applications such as high efficiency solar cells (O'Regan and Grätzel 1991), photocatalysis (Fujishima et al. 2000) and especially photooxidative self-cleaning (Muraca et al. 2019). The typical mechanism of photocatalysis on the TiO_2 photocatalyst is given below:

$$TiO_2 + hv \rightarrow h^+(VB) + e^-(CB) \quad (2.1)$$

$$H_2O + h^+(VB) \rightarrow H^+ + \bullet OH \quad (2.2)$$

$$O_2 + e^-(CB) \rightarrow \bullet O_2^- \quad (2.3)$$

$$2H_2O + 2\bullet O_2^- \rightarrow H_2O_2 + 2HO\bullet + O_2 \quad (2.4)$$

$$H_2O_2 + e^-(CB) \rightarrow 2HO\bullet \quad (2.5)$$

2.13 Improving of the Photocatalytic Efficiency of TiO_2

Modification of TiO_2 with cationic dopants, in particular precious metal atoms such as Au (Ayati et al., 2014, Oros-Ruiz et al. 2012, Hou et al. 2011, Scarisoreanu et al. 2020), Ag (Scarisoreanu et al. 2020, Pan et al. 2014, Nanaji et al 2019), Ru (Tian et al. 2016), Rh (Kohno et al. 1999), Pd (Chen and Hsu 2021), Os (Kuvarega et al. 2014), Ir (Subramanian et al. 2001), Pt (Scarisoreanu et al. 2020), transitional metal atoms such as Cu (Hinojosa-Reyes et al. 2019), Co (Savio et al. 2013, Ganesh et al. 2012), Ni (Wang et al. 2018a, Hinojosa-Reyes et al. 2019, Mohseni-Salehi et al. 2018), Mn (Binas et al. 2019), Mo (Manojkumar et al. 2020), V (Han et al. 2019, Han et al. 2018, Manojkumar et al. 2020), W (Manojkumar et al. 2020), Fe (Savio et al. 2013, Zafar et al. 2020, Safari et al. 2014, Ismael 2020, Hinojosa-Reyes et al. 2019), Sn (Bhange et al. 2016), and rare earth metal atoms La, Ce, Pr, Nd, Sm, Eu, Dy, Gd (Štengl et al. 2009, Saqib et al. 2016) have been widely studied. Doping of semiconductor nanoparticles with metal atoms is an important factor in achieving maximum efficiency of the photocatalytic reaction (Bumajdad and Madkour 2014). Dopants change the chemical nature and electronic structure of the semiconductor material. The performance of TiO_2 can be improved by narrowing its energy band gap, which leads to increased photoactivity in the visible region of the spectrum (Rahimi et al. 2016, Kumaravel et al. 2019).

Doping of TiO_2 with non-metal atoms is more effective than metal doping due to the reduction of recombination centers (Agbe et al. 2019). Various non-metals, such as nitrogen atom (Quesada-Cabrera et al. 2017, Smirniotis et al. 2018, Osin et al. 2018, Zhang et al. 2018, Marques et al. 2019, Acayanka et al. 2019), boron atom (Lee et al. 2015, Shindume et al. 2018, Abdelraheem et al. 2019, Hoşgün et al. 2019), carbon atom (He et al. 2014, Klaysri et al. 2017, Ratova et al. 2018, Ovodok et al. 2018), phosphorus atom (Guo et al. 2013, Niu et al. 2016, Gul et al. 2017, Feng et al. 2018) , sulphur atom (Devi and Kavitha 2014, Boningari et al. 2018, Modanlu and Shafiekhani 2019), florine atom (Lee et al. 2019) and bromine atom (Wang et al. 2017b) have been used to improve the photocatalytic activity of TiO_2 in the range of visible light (Devi and Kavitha 2013, Abdullah et al. 2017, Agbe et al. 2019). As an example to non-metal

atom doping, Smirniotis and his coworkers (2018) first successfully synthesized N-doped TiO_2 with a novel single-stage flame method. This synthesis method directs nitrogen atoms mainly to the interstitial positions of the TiO_2 lattice, which narrows the band gap (from 3.12 to ~ 2.51 eV) of TiO_2 (Smirniotis et al. 2018).

The coupling of different semiconductor oxides induces the efficient separation of electron hole pairs and is useful to achieve high photocatalytic efficiency (Noorjahan et al. 2013). To enhance the photocatalytic efficiency of titanium dioxide, a coupled semiconductor photocatalyst of titanium dioxide and zinc oxide has been investigated.

2.14 ZnO Photocatalyst

As in the case of TiO_2, the ZnO surface becomes energetically unstable after the hydroxyl adsorption. Oxygen adsorption is thermodynamically favored and it is more strongly bonded on the defect sites than the hydroxyl group. The superhydrophilic-hydrophobic transition is due to the gradual replacement of adsorbed hydroxyl groups by oxygen atoms when the UV-exposed films are kept in the dark (Barshilia et al. 2010, Yang et al. 2012), which returns the surface geometric and electronic structures similar to the native metal-oxide surfaces. Oxygen bridging sites also play an important role in the surface wettability transition. The typical mechanism of photocatalysis on the ZnO particle is given below:

$$ZnO + 2h\upsilon \rightarrow 2h^{+}(\text{valence band}) + 2e^{-}(\text{conduction band}) \quad (2.6)$$

$$O^{-2} + h^{+} \rightarrow O^{-} (\text{surface trapped hole}) \quad (2.7)$$

$$O^{-} + h^{+} \rightarrow \tfrac{1}{2}O^{-} (\text{oxygen vacancy}) \quad (2.8)$$

2.15 TiO_2/ZnO Composite

ZnO has been considered as an alternative photocatalyst to TiO_2 as they have similar properties as a semiconductor. Moreover, ZnO exhibits a higher electron mobility and

longer photogenerated electron lifetime than that of TiO_2, which is beneficial for photocatalytic degradation of dyes (Huang et al. 2013). In addition, similar to TiO_2, ZnO can only absorb a very small ultraviolet portion of the solar spectrum due to its wide band gap. Therefore, it is essential to develop new photocatalysts with a narrow band gap to harvest the visible light. Tian and his coworkers (2009) reported the synthesis of TiO_2/ZnO nanocomposite film via a sol-gel process. The TiO_2/ZnO nanocomposite film exhibited good photocatalytic activities for the degradation of methyl orange (Tian et al. 2009). ZnO/TiO_2 polycrystalline powders prepared by different methods also showed good photocatalytic degradation ability for 4-nitrophenol in aqueous solution (Marci et al. 2001). Wang and his coworkers (2018b) prepared TiO_2/ZnO composite powders by combining nanoscale TiO_2 and ZnO powders. The TiO_2/ZnO composite powders had high sonocatalytic activities for the degradation of acid red B under ultrasonic irradiation (Wang et al. 2018b). Pei and coworkers (2016) synthesized zinc oxide and titanium dioxide composite nanorods by the hydrothermal process using zinc acetate and titanium butoxide as the raw materials, and they investigate the photocatalytic properties of the composite nanorods. By examining the products obtained using different hydrothermal conditions, the formation process of zinc oxide and titanium dioxide composite nanorods was analyzed. Photocatalytic activities of composite nanorods were investigated under UV light irradiation using rhodamine B (RB) degradation as the probe reaction. The results showed that zinc oxide and titanium dioxide composite nanorods have great application potential for the treatment of organic pollutants (Pei et al. 2016).

2.16 Previous Work

Toghan and his coworkers (2021) reported a facile synthesis of zinc oxide coupled with 5, 10, 15, and 20 wt.% titanium oxide nanoparticles in gelatin under ultra-sonication. The photocatalytic activity of the prepared nanocomposites was examined using Rhodamine B dye. The prepared nanocomposites exhibited improved photodegradation efficiency under visible light irradiation. The reaction mechanism study revealed the dominance of the active species (h^+ and $\bullet O_2^-$) during the photocatalytic dye degradation reactions. The results of this study indicated the potential application of the gelatin

stabilized nanoparticles for the dye removal from aqueous solutions under sunlight irradiation (Toghan et al. 2021).

Mohsin (2020) prepared TiO_2 and ZnO/TiO_2 nanocomposites (NCs) using a simple sol-gel method at calcination temperatures of 400, 500, 600 and 700°C, respectively. XRD patterns and FTIR spectra confirmed the presence of TiO_2 and ZnO nanoparticles (NPs) without any change in the main peaks of the FTIR spectrum and the XRD diffractogram. UV-Vis spectra exhibited a shift of absorption edges towards the visible region. ZnO/TiO_2 NPs showed an increase in the antibacterial activity against bacteria strains Staphylococcus aureus. Increasing effectiveness of NCs could pave the way for important medical breakthroughs in the future (Mohsin 2020).

Firdaus and his coworkers (2012) prepared ZnO and $ZnO:TiO_2$ thin films on glass substrates through the sol-gel spray-spin coating technique. The current-voltage measurements showed that the conductivity of $ZnO:TiO_2$ thin films was higher than that of ZnO film. The structural analyses revealed that the surface morphology of $ZnO:TiO_2$ thin films exhibited high surface area as the thickness of thin films increased. The optical property analysis showed that the band gap for $ZnO:TiO_2$ thin films decreased as the film thickness increased (Firdaus et al. 2012).

Liao and his coworkers (2004) prepared a novel binary oxide ZnO/TiO_2 photocatalyst system through a new modified sol-gel method by using citric acid as a complex reagent, and the photocatalytic activity of the prepared photocatalyst sample was investigated in terms of the dye degradation efficiency of the photocatalyst. Several factors, such as the ratio of amount of doped zinc ion, the precursors, and the calcination temperature on the activities of ZnO/TiO_2 photocatalyst were studied. The dry gels of ZnO/TiO_2 was reacted with H_2SO_4 solution to prepare $SO_4^{2-}/ZnO/TiO_2$. It was showed that combining TiO_2 with ZnO could enhance the photocatalytic activity significantly, and sulfating ZnO/TiO_2 with sulfuric acid resulted in significant enhancement in the photocatalytic activity. The degradation rate of the model dye, methyl orange, could be

up to 71.9% compared to the 55% degradation rate of the ZnO/TiO_2 catalyst (Liao et al. 2004).

Johansson and his coworkers (2019) studied transparent ZnO and TiO_2 thin films, which were coated by spray pyrolysis on soda lime silicate float glass, as functional layers on PV cover glass. The ZnO film extended the optical bandgap to longer wavelengths, leading to a reduction of the transmittance of destructive UV radiation by up to ~85%. Photoluminescence peaks at 377 nm and at 640 nm were observed on the spectrum of the ZnO film sample. The TiO_2 coated glasses also exhibited an increased UV cutoff, leading to a decrease of transmittance of destructive UV radiation by up to 75%. However, no photoluminescence peaks were observed with the TiO_2 films at the excitation of 325 nm. The absence of the photoluminescence peaks was attributed to the fact that only indirect interband transitions are accessible at this specified excitation wavelength. Coating of both ZnO and TiO_2 films on the glass slide gave rise to a reduction of the transmitted light that could be converted by the PV modules by up to 12.3% and 21.8%, respectively. The implication of the results was discussed in terms of lifetime expectancy and efficiency of PV modules (Johansson et al. 2019).

2.17 Structural Properties and Surface Morphology

2.17.1 X-Ray diffraction

In 1919, Hull wrote a paper titled “A New Method of Chemical Analysis”. There, he pointed out that “every crystalline substance gives a pattern; the same substance always gives the same pattern; and in a mixture of substances each produces its pattern independently of the others.” (Hull 1919).

The orientation and interplanar spacing of crystal planes can be defined by the three integers (h, k, l), known as Miller indices. A given set of crystal planes with the Miler indices h, k, l cut the a, b and c axes of the unit cell in h, k and l sections, respectively.

In order to obtain a detailed understanding of the physics of semiconductors, knowledge of the structure arrangement of the solid is needed. The most common method for probing the arrangement of atoms in a solid is via the scattering or diffraction of waves from the atoms themselves. It is stronger when the wavelength of the waves is of the order of the size of the diffracting objects. For this reason, the scattering x-rays has become one of the principal means of structure determination (Jenkins 1995). The inter planer distance d_{hkl} for different planes was determined by using Bragg's law (Peierls and Peierls 1955):

$$n\lambda = 2d\sin\theta \quad (2.9)$$

where λ is the wavelength of the incoming X-ray, d is the spacing of the crystal planes, θ is the incident angle, and n is an integer. Each reflection is fully defined if the d-spacing, the diffraction intensity and the indices h, k, l are known. After determination of the d-spacing and the corresponding indices h, k, l, the dimension of a unit cell can be determined. The average crystalline size can be estimated using Debye-Scherrer formula (Pecharsky and Zavalij 2009):

$$D = K\lambda / \beta \cos\theta \quad (2.10)$$

where D is the mean crystalline size, K is a factor, λ is the wavelength of incoming X-ray, β is the full width at half maximum intensity of the main diffraction peak, and θ is the Braggs' angle.

2.17.2 Field Emission Scanning Electron Microscopy (FESEM)

Nanotechnology has strongly driven the development of the latest electron microscopy, with demands not only for increasing resolution but also for more information from the sample. Electron microscopes use a beam of highly energetic electrons to probe objects on a very fine scale (Koerkamp et al. 1998, Kaech 2013). The required electrons can be generated by "heating" a tungsten filament, which is an electron gun. They can also be generated from a crystal of LaB_6. The use of specified LaB_6 crystal leads to a higher electron density in the beam and also a better resolution than that of the conventional

instrument. In a field emission (FE) electron microscope, there is no heating but a so-called "cold" source is utilized. Field emission is the emission of electrons from the surface of a conductor resulted from a strong electric field. An extremely thin and sharp tungsten needle, which has a tip diameter of 10–100 nm, works as a cathode. The FE source was integrated into scanning electron microscopes (SEMs) whose development has been supported by advances in secondary electron detector technology. The acceleration voltage between the anode and the cathode is in the order of magnitude ranging from 0.5 to 30 kV, and the equipment needs an extreme vacuum (~10^{-6} Pa) in the column of the microscope. Since the electron beam produced by the FE source is about 1000 times smaller than that of a standard microscope with a thermal electron gun, the image quality has been markedly improved. The resolution is on the order of ~2 nm at 1 keV and ~1 nm at 15 keV. Hence, the FE scanning electron microscope (FE-SEM) is a very useful instrument for high resolution surface imaging in the field of nanomaterials science (Ramkumar et al. 2018, Huggett and Shaw 1997).

Because the gold plating used in conventional SEM is very rough and a mosaic-like pattern is formed on the sample surface, it can obscure morphological features. Therefore, before SEM analysis, samples should be coated with 30-40 nm thick gold-palladium or platinum coatings (Huggett and Shaw 1997).

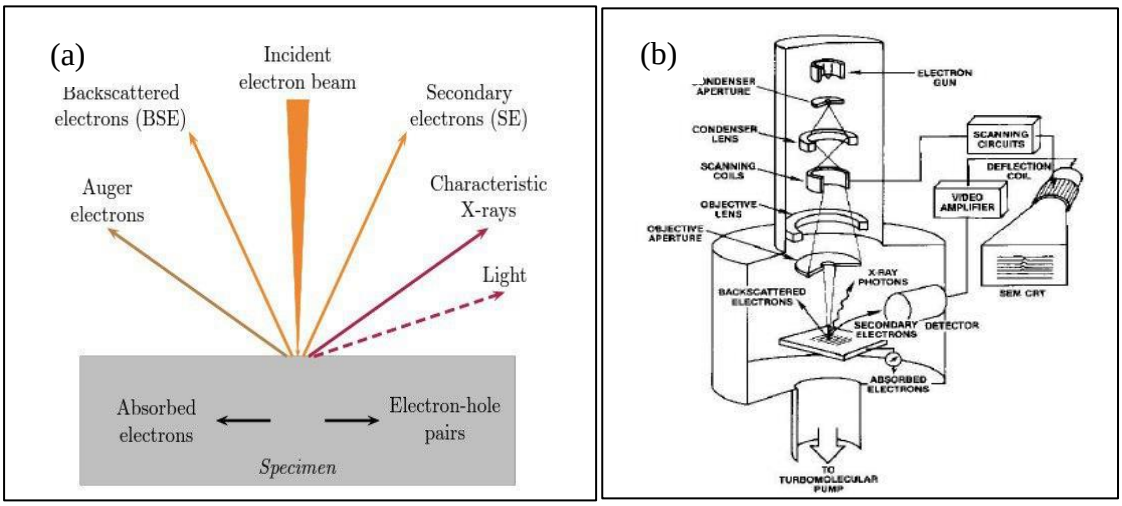

Figure 2.10 (a) The emission of electrons from the surface of a conductor (Koerkamp et al 1998), (b) schematic diagram of a typical SEM system (Pawley 1997)

In FE-SEM analysis, a beam of electrons with a small spot is directed pixel-by-pixel over the surface of a sample. In each pixel, the beam remains for a defined time and produces a signal (for example, secondary electrons) that is detected, amplified, and displayed on a computer screen. The scanning of the specified beam is synchronized with the image of the computer screen. The signal obtained from each pixel on the sample is simultaneously displayed on the corresponding pixel of the computer screen and finally forms the image (Figure 2.10) (Anonymous 2023e, Jenei 2012).

2.18 Optical Properties

The optical properties of a semiconductor are related to intrinsic effect. Based on the intrinsic location of the top of the valence band (V.B.) and bottom of the conduction band (C.B.) in the band structure, the electron-hole pair generation occurs directly or indirectly (Grenier 1961).

2.18.1 Optical absorption and absorption edge

Fundamental absorption is the most crucial absorption process involving the transition of electrons from the valence band to the conduction band, and this is manifested by a rapid increase in absorption, which can be used to determine the optical energy gap of the semiconductor (Grenier 1961).

If the photon energy (hν) of the incoming light is equal or greater than the optical energy gap (E_g) of the material, then the photon can interact with a valence band electron, inducing the electron into the conduction band and forming the photoinduced electron-hole pairs. The maximum wavelength (λ_c) of the incident photon which forms the electron-hole pairs is defined as (Millman 1979):

$$\lambda(\text{nm}) = hc/E_g = 1240/E_g(\text{eV}) \quad (2.11)$$

The intensity of the photon flux decreases exponentially with distance through the semiconductor according to the following equation (Elliot and Gibson 1974):

$$I = I_o \exp(-\alpha t) \quad (2.12)$$

where I_o and I are the incident and the transmitted photon intensity, respectively, α is the absorption coefficient, which is defined as the relative number of the photons absorbed per unit distance of semiconductor, and t is the thickness of the material.

There are two types of the optical transitions (Figure 2.11), discussed below:

a) Direct Transitions: The direct transition in general occurs between the top energy state of the valence band and the bottom energy state of the conduction band (vertical transition) at the same wave vector $\overrightarrow{\Delta k} = 0$ for the conservation of momentum. This type of this transition is known as the allowed direct transition at which the wave vector equals to zero ($\vec{k} = 0$) (Figure 2.11a). The specified transition is described by the following relation (Kazmarski 1980):

$$\alpha h\nu = B(h\nu - E_g)^{1/2} \quad (2.13)$$

in which B is inversely proportional to amorphicity. If the transition occurs between the states of the valence band and the conduction band with the same wave vector, which is not equal to zero, then the transition is called as forbidden direct transition (Figure 2.11b). The specified transition obeys the following relation (Burns 1985):

$$\alpha h\nu = B(h\nu - E_g)^{3/2} \quad (2.14)$$

b) Indirect Transitions: In an indirect transition, there is a big momentum difference between the states of the valence band and the conduction band where the transition occurs. It means that the bottom energy state of the conduction band is not at the same value of $\vec{k}$ as the top energy state of the valence band. Therefore, the assistance of a phonon is necessary to maintain momentum:

$$h\nu = E_g \pm E_p \quad (2.15)$$

where E_p refers the energy of an absorbed or emitted phonon (Burns 1985). On the other hand, the transition occurs from the top energy state of the valence band to the bottom energy state of the conduction band for an allowed indirect transition (Figure 2.11c). The optical band gap energy can be calculated using the following equation (Kazmarski 1980):

$$\alpha h\nu = B(h\nu - E_g)^2 \quad (2.16)$$

On the other hand, the forbidden indirect transitions take place from any energy state near the top of the valence band to any energy state other than the bottom energy state of the conduction band (Figure 2.11d). For the forbidden indirect transition, the optical band gap energy can be determined using the following relation (Kazmarski 1980):

$$\alpha h\nu = B(h\nu - E_g)^3 \quad (2.17)$$

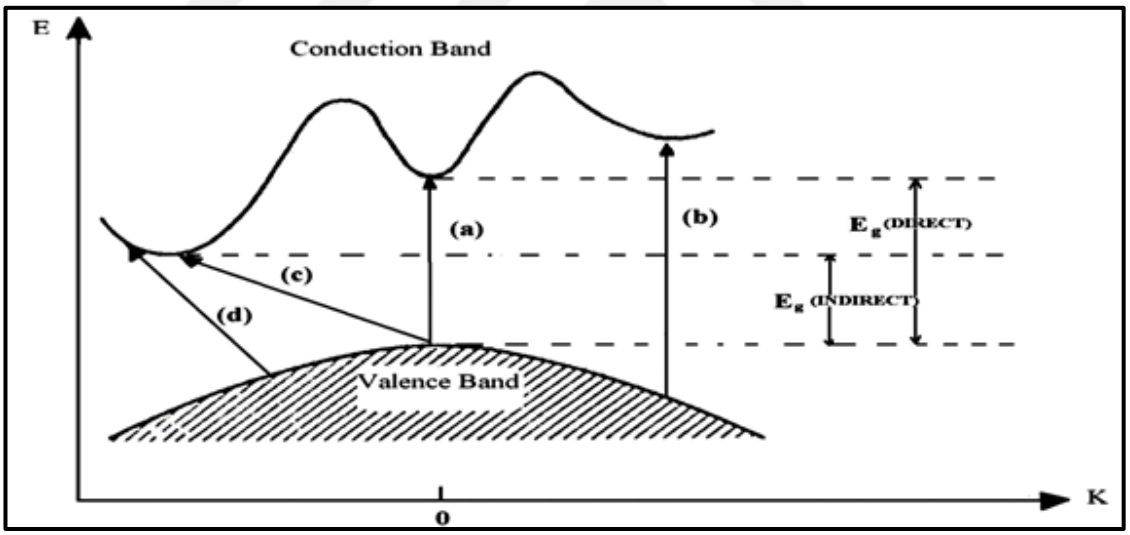

Figure 2.11 The optical transitions: (a) Allowed direct, (b) Forbidden direct; (c) Allowed indirect, (d) Forbidden indirect (Ray 1969)

2.18.2 Complex refractive index

To determine the optical constants of the films, the relationship between various optical constants was determined. The complex refractive index n_c, which is related to the

velocity ($v = c/n_c$) of the radiation propagation, is defined by the following relation (2.18) (Chopra 1969):

$$n_c = n - ik \tag{2.18}$$

where n and k are the real and imaginary parts of the complex refractive index. The dielectric constant (ε), known complex relative permittivity, can be introduced as follows (Pankove 1971):

$$\varepsilon = \varepsilon_r - i\varepsilon_i \tag{2.19}$$

where ε_r is the real part of the complex relative permeability and ε_i is the imaginary part of the complex relative permittivity. The real part of the complex relative permittivity is a measure of the energy stored within a material from an external field, and the imaginary portion of the complex relative permittivity is a measure of the energy lost (Pankove 1971). On the other hand, the relative permittivity is used in Maxwell's equations following the relation (Kazmerski 1980):

$$(n - ik)^2 = \varepsilon_r - i\varepsilon_i \tag{2.20}$$

In the Maxwell's equation, the real part and the imaginary part are related by the following relations, respectively (Kazmerski 1980):

$$\varepsilon_r = n^2 - k^2 \tag{2.21}$$

and

$$\varepsilon_i = 2nk \tag{2.22}$$

2.18.3 Fourier transform infrared (FT-IR) spectroscopy

IR spectroscopy is known as the measurement of the wavelength and intensity of the absorption of infrared light by an unknown sample. Infrared spectrum can be generated by the characteristic twisting, bending, rotating and vibrational motions of atoms in a molecule. All of the specified motions can be described in terms of two types of

molecular vibrations. The first type of vibration, which is a stretch, can produce a change of the bond length. A stretch is a rhythmic movement along the line between the atoms. The second type of vibration, which is a bend, leads to a change in the bond angle. A stretch can be symmetric or asymmetric. Bending can occur in the plane of the molecule or out of plane (Figure 2.12) (Garip 2005, Amir et al. 2013).

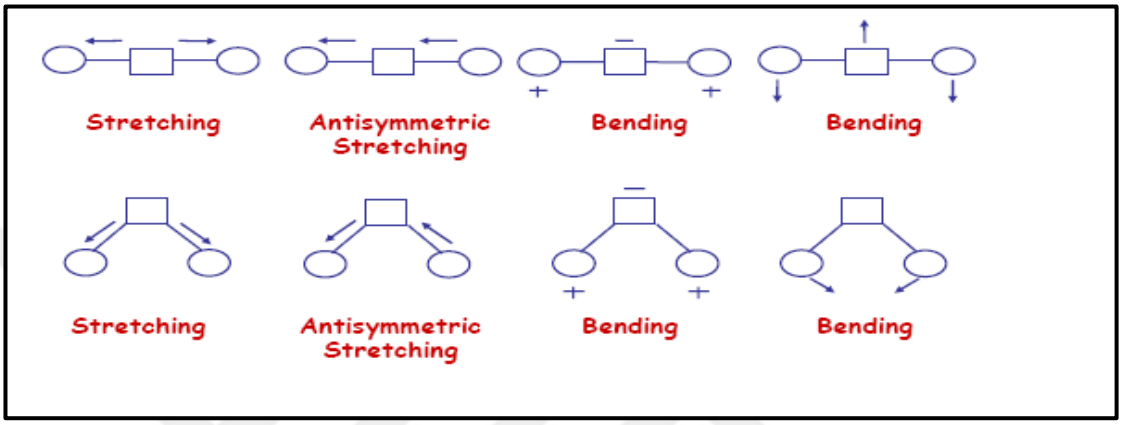

Figure 2.12 Types of normal vibrations in a linear and non-linear triatomic molecule (Garip 2005)

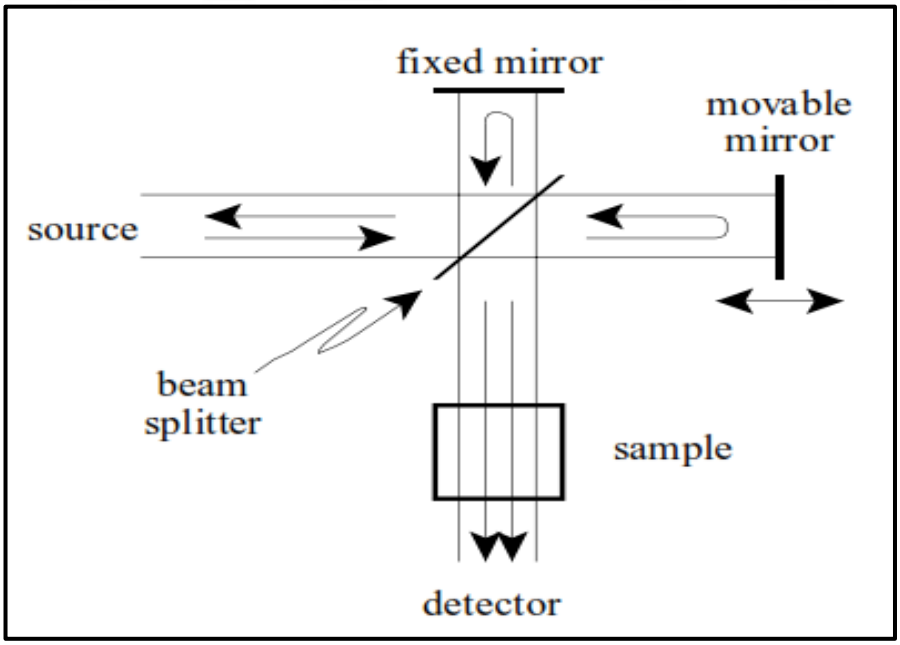

Figure 2.13 Schematic representation of FT-IR spectrophotometer (Garip 2005)

During FTIR analysis, the light is directed at the sample of interest and the intensity is measured using an infrared detector. The intensity of light hitting the detector is measured as a function of mirror position, which is then Fourier transformed to generate a graph of intensity versus wavenumber (Figure 2.13) (Garip 2005, Harris and Bertolucci 1989, Rodriguez 2000).

3. MATERIALS AND METHODS

3.1 Introduction

This chapter presents the description of the method implemented in this work for the preparation of TiO_2 and ZnO nanoparticles. TiO_2 and ZnO were coupled in varying weight ratios (75/25, 50/50 and 25/75 wt%) to prepare TiO_2/ZnO nanocomposites. Field emission scanning electron microscopy (FE-SEM) was carried out for pure TiO_2 and ZnO films to investigate the size and shape of nanoparticles. The structure properties were studied by X-ray diffraction and Fourier transform infrared (FTIR) spectroscopy. Optical studies (absorption spectroscopy and luminescence spectroscopy) were performed for all thin film samples prepared. As well as, contact angle measurements were performed to test the photocatalytic activity of pure TiO_2, ZnO and TiO_2/ZnO composite (TiO_2/ZnO: 75/25, 50/50 and 25/75 wt./wt.) films. Finally, I-V test was performed for pure TiO_2, ZnO and TiO_2/ZnO composite (TiO_2/ZnO: 75/25, 50/50 and 25/75 wt./wt.) films on the silicon solar cell surface to investigate their effects on the solar cell efficiency.

3.2 Preparation of Nanoparticles

3.2.1 Preparation of colloidal TiO_2 nanoparticles

The schematic diagram for preparation of TiO_2 nanoparticles is shown in Figure 3.1. Three necked flask was used for the synthesis reaction: one neck for adding titanium tetrachloride ($TiCl_4$) and the second closed, and the third for thermometer. Hot plate heater with magnetic stirrer was used to homogenize the chemical mixture under controlled reaction temperature (Figure 3.2).

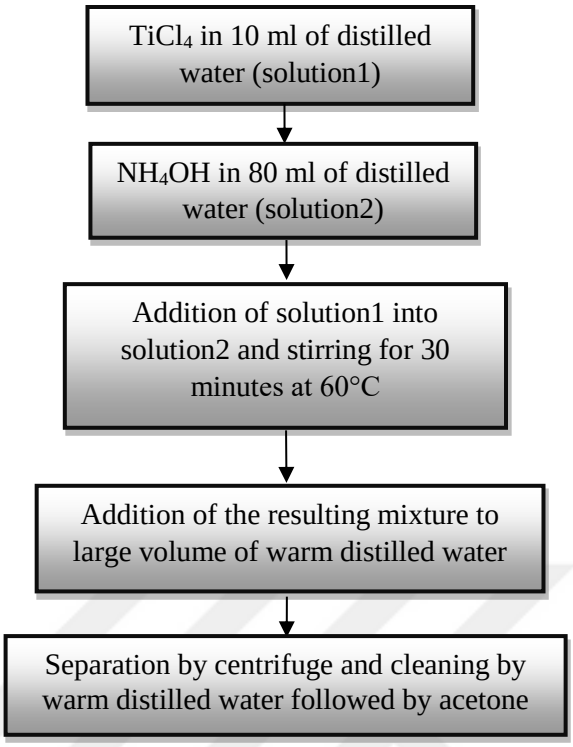

Figure 3.1 Schematic diagram for preparation of TiO_2 nanoparticles

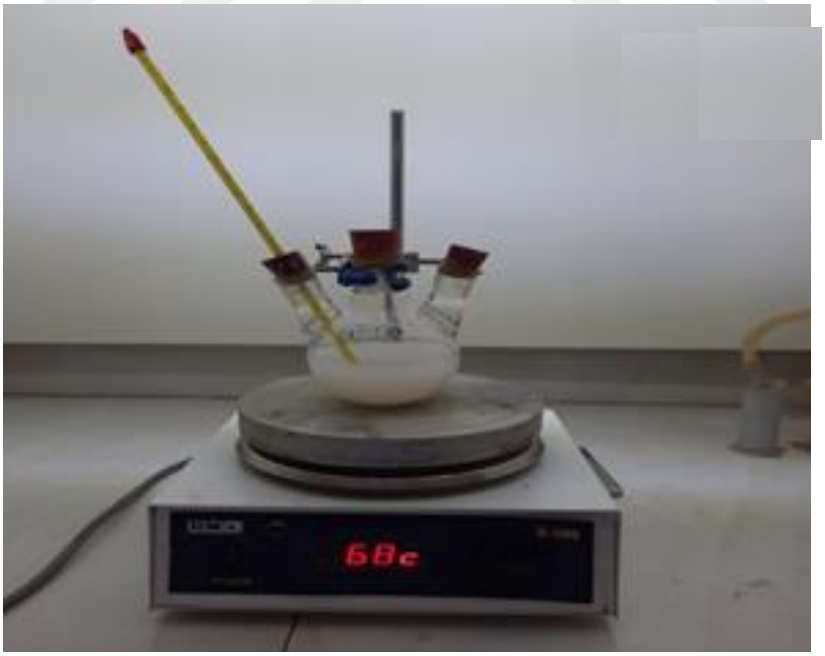

Figure 3.2 Experimental setup for TiO_2 nanoparticles preparation

To prepare the TiO_2 nanoparticles according to a wet chemical method, the first solution was prepared using $TiCl_4$. 1.5 ml of $TiCl_4$ had been diluted with cold distilled water in 10 ml. The second solution was prepared using ammonia (NH_4OH). 20 ml of NH_4OH had been diluted with cold distilled water to 80 ml. The second solution was kept under magnetic stirring to homogenize the solution. After dissolving, the first solution (titanium tetrachloride) was added into the second solution (ammonia solution) by slow addition. Then, the resulting solution was kept under stirring. The hydrolysis reaction of $TiCl_4$ was carried out at 60ºC for 30 minutes. When the solution was vigorously stirred, amorphous TiO_2 precipitates were obtained, as show in Figure 3.2. Then, TiO_2 nanoparticles were separated by centrifugation and cleaned by rinsing with distilled water and acetone (Desai et al. 2011).

3.2.2 Preparation of ZnO nanoparticles

Three-necked flasks were used for the preparation of the ZnO nanoparticles: one neck for inserting the thermometer, the second for inserting the condenser and the third locked. Hot plate with magnetic stirrer was used for homogenizing the chemical mixture and to control the reaction temperature (Figure 3.3).

ZnO nanoparticles were synthesized by mixing two solutions following a one-step synthesis method. The first solution was prepared by dissolving potassium hydroxide (KOH) (3.22 mg) with a concentration of 2 mmol in 65 ml of methanol at 30°C for 15 min. pH of the solution was adjusted to 8.2 using ammonium hydroxide. The resulting solution was kept under stirring to homogenize the solution. The second solution was prepared by dissolving zinc acetate ($ZnC_4H_6O_4$) (2.014 mg) of a concentration of 1.25 mmol in 125 ml of methanol on a hot plate magnetic stirrer at 60ºC until it dissolved. Afterward, the first solution was added to the second solution by drop wise and the resulting solution was kept under stirring at 60 ºC for 1 hour (Figure 3.4). Finally, the solution was centrifuged and the as-prepared precipitates were washed with ethanol for 15 min until the ZnO nanoparticles were formed (Khan et al. 2020).

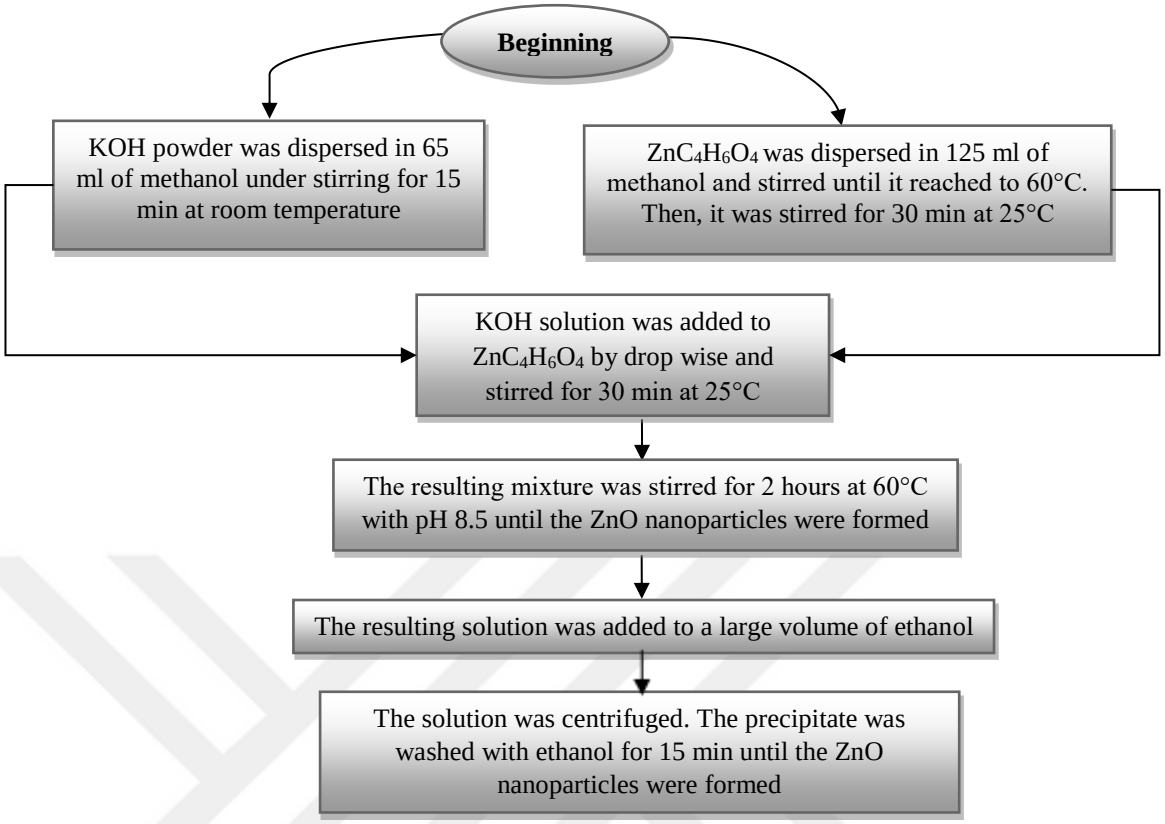

Figure 3.3 Schematic diagram for preparation of ZnO nanoparticles

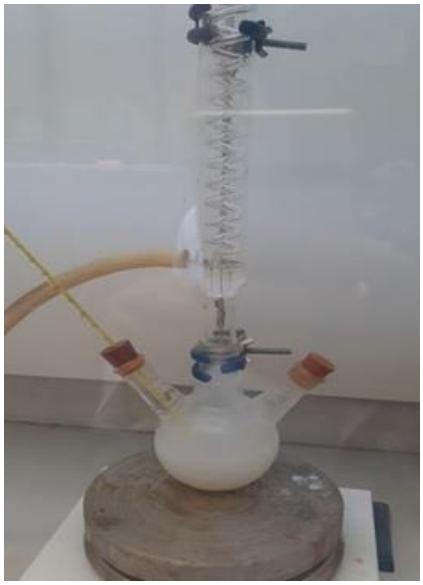

Figure 3.4 Experiment setup for synthesis of the ZnO nanoparticles

3.3 Cleaning of the Glass Substrates

The cleaning procedure of glass substrate (using commercial microscopic glass slides) can be summarized as follows:

1. The glass slides were cleaned by using detergent with tap water to remove any dust or oil that can be attached to the glass surface, and the glass slides were held under tap water with gentle rubbing for 15 minutes.
2. The glass slides were held in a clean beaker including distilled water and then they were rinsed with distilled water in ultrasonic bath for 15 minutes.
3. Repeating step 2, replacing distilled water with a pure alcohol solution that can remove contaminants such as grease and some oxides.
4. Finally, the substrates were put in a furnace at 400ºC for 15 minutes in order to remove residual organic contaminants.

3.4 Preparation of TiO_2, ZnO and TiO_2/ZnO film

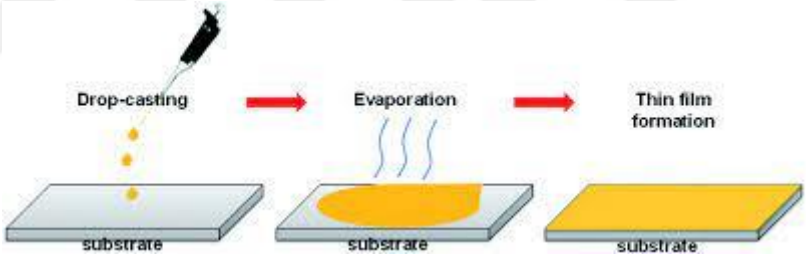

Figure 3.5 Drop casting steps

The simple, easy, low cost and rapid technique of “drop casting” is widely used to prepare the film surface whose layer consists of particles such as nanotubes or nanoparticles. This coating technique is affected by different factors such as the surface tension and volatility of the solvent utilized to prepare the solution, the wettability of the surface to be coated, the composition of the solution, or the drop impact velocity. In addition, the size of the droplet has to be considered depending on the dimensions of the surface. The needle used to drop the solution has to be close enough to the substrate surface since the deposited droplets are tiny (~50 μl) to coat. Otherwise, it can remain at the end of the needle. Hence, it is necessary to position the needle quickly and accurately on the substrate surface. Figure 3.5 shows the drop casting steps.

TiO_2, ZnO and TiO_2/ZnO composites (TiO_2/ZnO: 75/25, 50/50 and 25/75 wt./wt.) were deposited on the microscopic glass slide or the silicon (Si) solar cell by drop casting (gravitational force) method as follows: First the colloidal solution of TiO_2, ZnO and TiO_2/ZnO composites were prepared. As mentioned before (3.2.1 and 3.2.2), after the colloidal solutions of TiO_2 and ZnO nanoparticles separated by centrifugation and washing for several times to purify the materials, the yields were dried in vacuum oven at 80°C for 24h, then the TiO_2 and ZnO nanoparticles in powder form were obtained. The different ratios of nanocomposite solutions (TiO_2, 0.75TiO_2/0.25ZnO, 0.5TiO_2/0.5ZnO, 0.25TiO_2/0.75ZnO and ZnO wt.%/wt.%) were prepared by mixing the as-prepared powders (100 mg TiO_2, 75 mg TiO_2/25 mg ZnO, 50 mg TiO_2/50 mg ZnO, 25 mg TiO_2/75mg ZnO and 100 mg ZnO) with deionized water to form 10 mg/ml suspensions and then stirred for 6h on magnetic stirrer. Then, the microscopic glass slide or the Si solar cell was coated with the as-prepared colloidal solution. For this purpose, the microscopic glass slide or the Si solar cell was located horizontally on a flat table, and the colloidal solution of the prepared nanoparticles was drop casted onto it. The films were dried in the lab for 24 hours. The structure and the image of the coated film are shown in Figure 3.6. The composite film samples prepared in the presence of 25, 50 and 75 wt.% ZnO were named as: 075TiO_2/0.25ZnO, 0.5TiO_2/0.5ZnO and 0.25TiO_2/0.75ZnO, respectively.

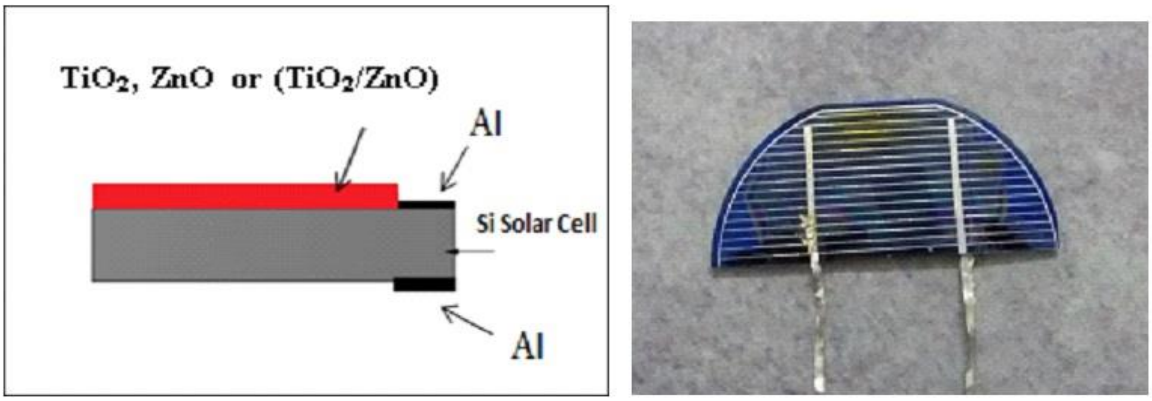

Figure 3.6 Structure and image of the coated film (TiO_2, ZnO or TiO_2/ZnO) on the Si solar cell

Optical interference fringes method was used to measure the films thickness. Fizaeu fringes of equal thickness, resulting from the interference of two beams occurring near a thin film layer, are obtained in an optical apparatus with an accuracy of 0.4%. The film thickness (d) can be given by the following equation (Chopra 1969):

$$d = (\lambda * \Delta X) / (2 * X) \quad (3.1)$$

where ΔX is the shift between interference fringes, λ is the (Na) wave length (5893 A°) and X is the distance between interference fringes.

3.5 Solar Module Analyzers

Solar panel analyzer (Prova 200), used for the professional testing and maintenance of solar panels and modules, was utilized to analyze the solar cell performance. During the installation of solar panels, the specified solar panel analyzer helps to determine the proper inverter size as well as optimum power output position of panels, and assists in identifying the defective cells or panels that have worn out over time. The solar panel analyzer provides current and voltage (I-V) test curves, the current and voltage at the maximum power point as well as the maximum solar power. Solar cell efficiencies are also easily determined using the testing unit. Test results can be saved and downloaded to a PC for later analysis using the application software that is supplied with the portable solar panel analyzer, as shown Figure 3.7.

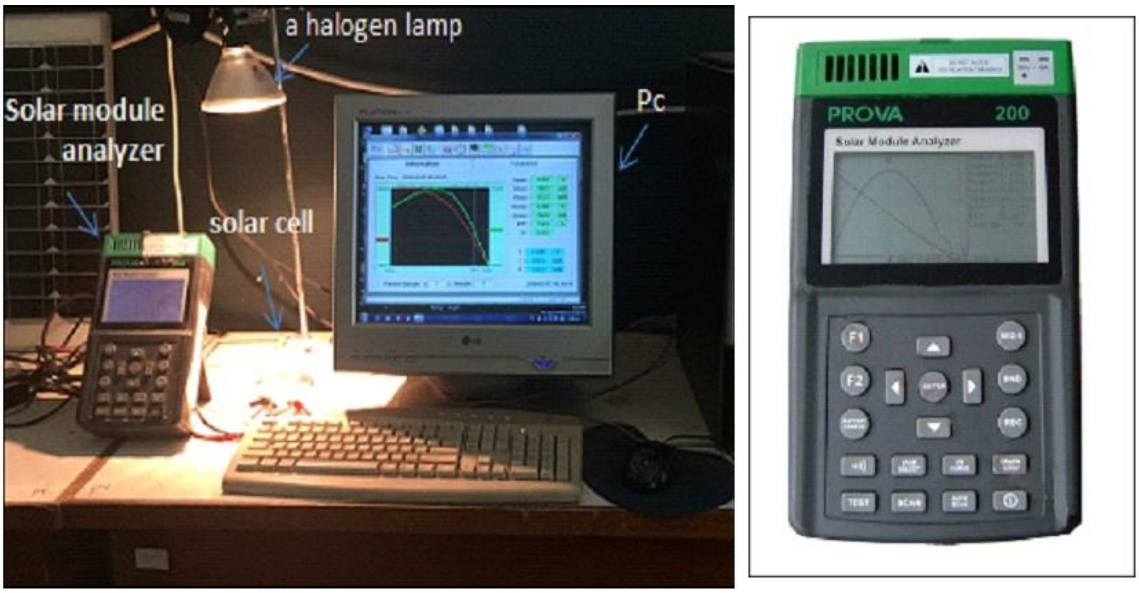

Figure 3.7 Solar module analyzer and the experimental setup to analyze the efficiency of the solar cell

The solar cell efficiency (η) is known as the percentage of incident power (P_{in}) that can be converted into electricity by the solar cell. The solar cell efficiency can be calculated using the following relation:

$$\eta = (V_{OC} * I_{SC} * FF)/P_{in} \quad (3.2)$$

where V_{OC} is the open circuit voltage, I_{SC} is the short circuit current and FF is the fill factor. An important parameter exhibiting the quality of the solar cell is the fill factor (FF), which can be determined using the following relation:

$$FF = P_m/(V_{OC} * I_{SC}) \quad (3.3)$$

where P_m is the maximum power point. The solar cell, which was coated with the as-prepared films, was analyzed by using a halogen lamp, which is a solar light simulator. Under the halogen lamp, certain values of the solar cell, such as the short circuit current, the open circuit voltage, the voltage of maximum power and the current of maximum power, were obtained. These values were utilized to calculate the fill factor, the maximum power point and the solar cell efficiency of both uncoated and film coated solar cells.

3.6 Measurements and Characterization

Different measurements were carried out on the pure and composite film samples in order to characterize, classify and optimize them according to the main goal of this work. UV-Visible spectroscopy, X-ray diffraction (XRD) analysis, field emission scanning electron microscopy (FESEM), and energy-dispersive X-Ray (EDX) spectroscopy were employed. Finally, the contact and sliding angle tests were done to investigate the self-cleaning property of the prepared film surfaces.

3.6.1 X-Ray diffraction measurement

Figure 3.8 LabX XRD-6100 Shimadzu model XRD diffractometer

The X-ray diffraction is a widely used method to determine the dimensional parameters of crystals and to estimate average crystalline size using the well-known Scherrer equation. To study the crystalline structure of TiO_2 and ZnO film samples, X-ray diffraction measurements were performed using a LabX XRD-6100 Shimadzu (Cyoto, Japan) model diffractometer with CuKα radiation source (Figure 3.8).

3.6.2 Fourier transform infrared (FTIR) spectroscopy

Fourier transform infrared (FTIR) spectroscopy was performed to analyze the chemical structure of the pure and the composite film samples. The transmittance peaks in the FTIR spectrum of the prepared film samples were analyzed and compared with the data in the literature. The position and the intensity of the transmittance peaks are a sign of successful synthesis of the film samples. FTIR spectrum for prepared films was recorded using Nicolet iS10 (Thermo Scientific) model spectrophotometer. FTIR spectrum was measured over the range of 400-4000 cm^{-1} with a resolution 4 cm^{-1} at room temperature and recorded in the transmittance mode.

3.6.3 Field emission scanning electron microscopy (FESEM)

Field emission scanning electron microscopy (FESEM) provides topographic and elemental information at a magnification from 10x to 300000x with virtually unlimited depth of field. A field-emission cathode in the electron gun of a scanning electron microscope provides narrower probing beams at both low and high electron energies, leading to enhanced spatial resolution, minimized sample damage and sample charging. FESEM analyzes were performed by MIRA3 TESCAN model field emission scanning electron microscope. Prior to analyzes, the film samples were coated with a thin layer of gold, inhibiting charging, reducing thermal damages and improving the secondary electron signal required for topographic examination in the FESEM analysis.

3.6.4 Optical properties

The optical properties of the prepared film samples were also studied. Within this context, UV-Vis absorption spectroscopy and photoluminescence spectroscopy analyzes were performed.

3.6.4.1 UV-Vis absorption

Figure 3.9 UV-Vis spectrophotometer

The absorbance of the prepared film samples was measured using Optima SP-3000 model UV-Vis spectrophotometer (supplied by Optima Company) covering a range from 200-1200 nm, as shown in Figure 3.9. The measured absorbance as a function of wavelength was used for the calculation of several parameters such as: absorption coefficient (α) and optical energy gap (E_g) of TiO_2, ZnO and TiO_2/ZnO films. The optical energy gap can be calculated using the Tauc relations (2.13-17). The absorption coefficient (α) can be calculated using the following relation:

$$\alpha = 2.303\ A/d \qquad (3.4)$$

where d is the film thickness and A is the absorbance. The absorbance data were obtained from the UV-Vis spectrophotometer and the film thickness was calculated using the optical interference fringes method (3.1).

3.6.4.2 Photoluminescence

Photoluminescence spectrum of the prepared film samples was measured using a Shimadzu RF-5301PC model fluorescence spectrophotometer with the spectrum range from 200-1100 nm, as shown in Figure 3.10. In addition to the Tauc relation, the

photoluminescence spectrum was also utilized to estimate the optical band gap energy using the following relation:

$$E_g^{opt} = 1200/\lambda \quad (3.5)$$

where λ is wavelength of the incoming light.

Figure 3.10 Shimadzu RF-5301PC model fluorescence spectrophotometer

3.6.5 Self-cleaning measurements

3.6.5.1 Contact angle measurement

Contact angle measurements are utilized to evaluate surface cleanliness, and the effects of surface treatments applied to surfaces as a part of fundamental study in surface science. The hydrophilic behavior of the prepared film surface was evaluated by measuring the water contact angle as shown in the Figure 3.11. A homemade device to measure the water contact angle is composed of a camera (Huawei y7 model mobile phone with 13 megapixels camera resolution), which captures the image of the water droplet, a dispensing unit and a light source. The camera was positioned at about 12 cm away from the sample. A commercial lamp with a power of 350 watts was used as the light source. The lamp was placed behind the sample to make the drop of liquid appears black. It is essential to perform the measurements in a closed environment (in a covered

box) for accurate measurements and image processing to prevent stray light. A droplet (5μL) of deionized water was injected on the surface of the film using a micro-injector. The syringe was pointed vertically down onto the sample surface.

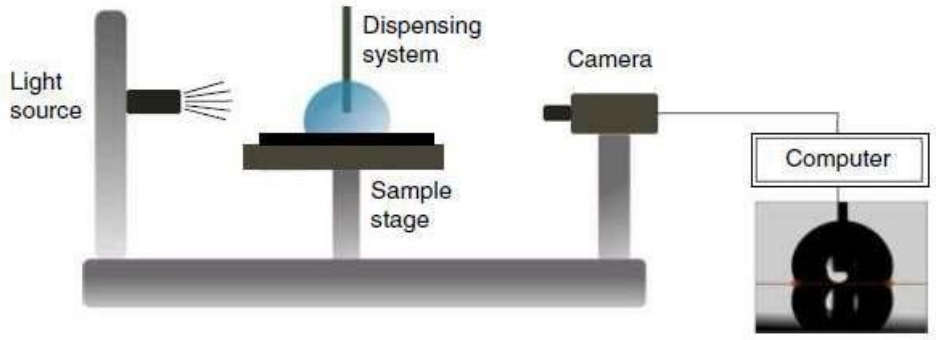

Figure 3.11 Contact angle measurement unit

3.6.5.2 Sliding angle measurement

Slide angle, measured using a homemade device, is an empirical data for a specific description of a surface and its wettability. The low slip angle is of great importance for self-cleaning. The slip angle, also known as the "roll angle", is one of the inclinations when the water drop is completely rolling off the surface without external force. In the experiment, the contact angle measuring instrument was equipped with an adjustable tilt angle plate from 0˚ to 360˚. The angle of inclination was increased continuously from 0˚ to 90˚, and the angle was recorded as y_{SA} as the droplet slides away or rolls off the surface (Figure 3.12).

Figure 3.12 Sliding angle device

Usually, water droplets (of a certain size) are placed on a hard surface and tilted plate, and then begin to tilt at a constant speed. When a drop of water slides or rolls off the surface, the angle of inclination is the angle of sliding, suitable for microscopically flat surfaces. For macroscopic rough surfaces where water droplets of a given size are released onto the substrate from some height, the critical angle is the sliding angle at which the substrate is to be tilted for the drop to roll off the surface.

4. RESULTS AND DISCUSSION

4.1 Introduction

This chapter will investigate the experimental results details (structural, composition analysis, surface morphology, optical and electrical characteristics) of titanium oxide and zinc oxide, and their composites with varying ZnO content as films. All prepared films were used to coat the standard silicon solar cell to test the change in its efficiency before being used as the self-cleaning coating. The thickness of all prepared films was between 5-6 μm according to the optical interference fringes method (3.1).

Finally, self-cleaning properties have been achieved with the films prepared, their hydrophilic property and photo-catalytic activity were studied by measuring the contact angle, and the sliding angle was also measured for all films.

4.2 Structural Analysis (X-ray Diffraction Measurement)

The crystal structure of TiO_2 film was examined by XRD diffraction measurement and its result is shown in Figures 4.1. The anatase TiO_2 phase was observed in this pattern, with five diffraction peaks all assigned to the anatase TiO_2 crystal phase (Thamaphat et al. 2008). The spacious diffraction peak belonging to the amorphous phase was not found in the XRD pattern. The prominent peaks were compared with JCPDS data (PDF No: 21-1272) and the peaks obtained in the pattern coincides well with the literature. All the characteristic peaks of TiO_2 were observed at 25.82°, 43.07°, 48.72°, 55.47° and 62.44°, which correspond to the (101), (210), (200), (211) and (204) planes, respectively. The XRD pattern revealed that the crystals were well matched to the TiO_2 tetragonal lattice (Deng et al. 2001).

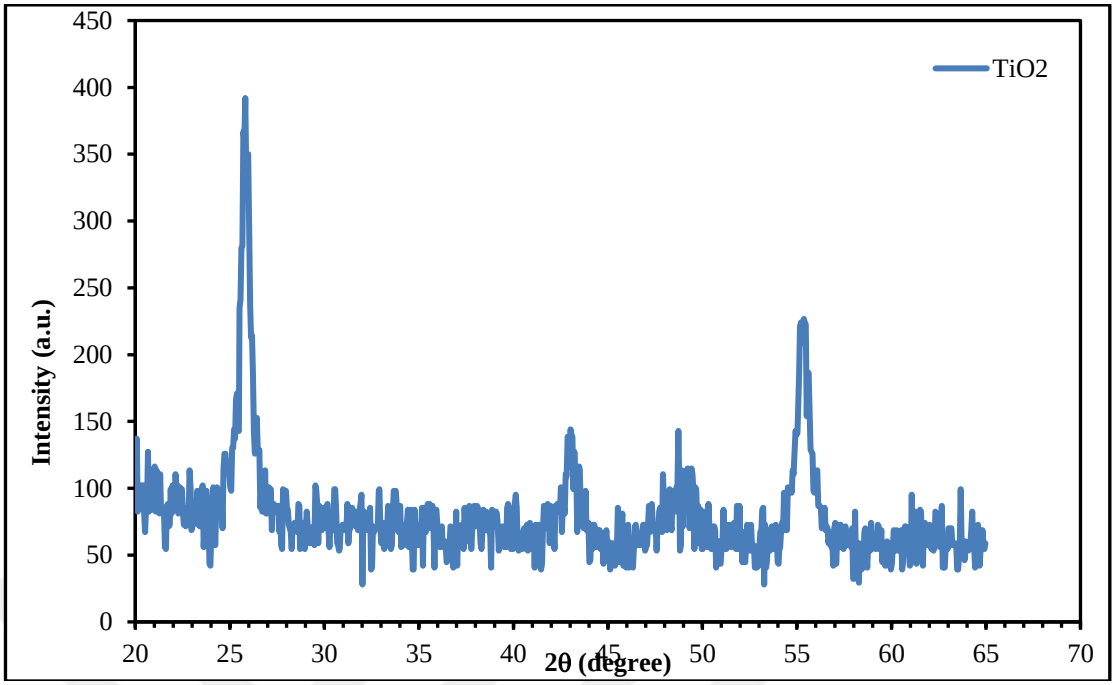

Figure 4.1 XRD diffractogram of TiO_2 film

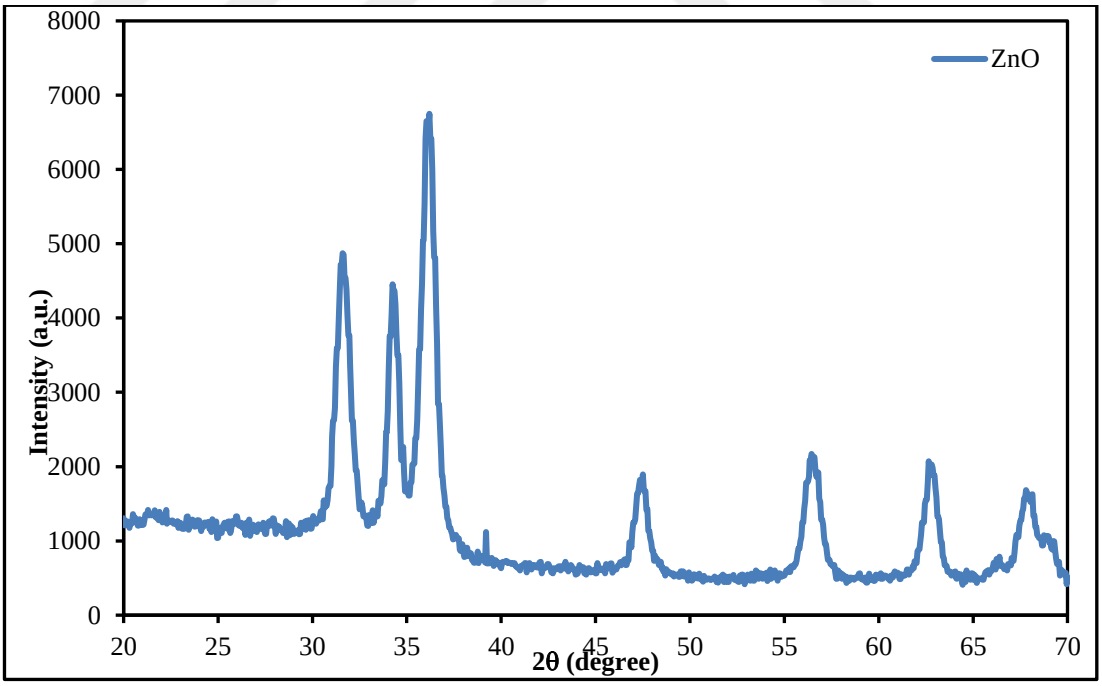

Figure 4.2 XRD diffractogram of ZnO film

The XRD pattern of the ZnO film sample is illustrated in Figure 4.2. The entire XRD pattern is in excellent conformity with the JCPDS card No. 36-1451. The diffraction peaks observed at 31.65°, 34.35°, 36.20°, 47.50°, 56.60°, 62.85° and 68.1° belonging to the (100), (002), (101), (102), (110), (103) and (112) planes, can be attributed to the hexagonal wurtzite structure of ZnO (Ismail et al. 2018). The sharp diffraction peaks of the synthesized film sample indicated its high crystallinity. The ZnO nanoparticles have grown in polycrystalline nature, which is exhibited in the appearance of a number of XRD peaks attributed to different crystalline orientations.

4.3 Compositional Analysis

4.3.1 FTIR measurement

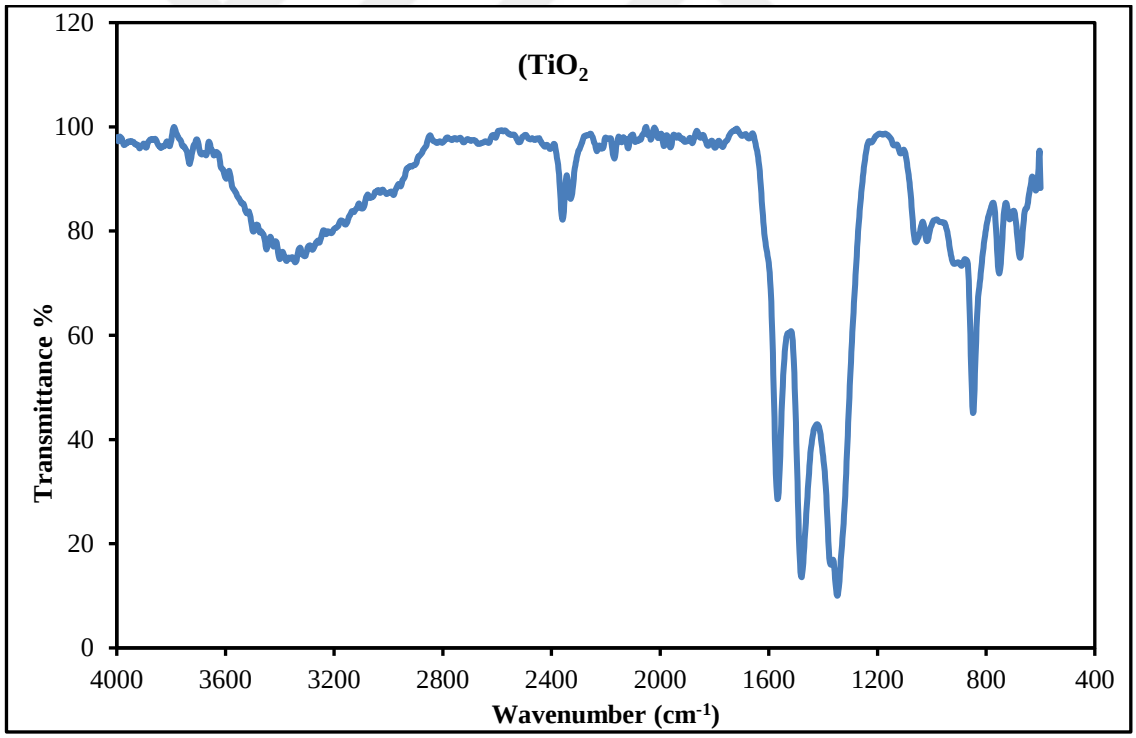

Figure 4.3 FTIR transmittance spectrum of TiO_2 film

FTIR was performed in order to study and determine the functional groups of synthesized TiO_2 and ZnO films, and their composites with varying compositions. The

FTIR spectrum of TiO_2 film clearly shows its characteristic bonds as shown in Figure 4.3. The peaks at 667 cm^{-1}, 505 cm^{-1} and 447 cm^{-1} are attributed to Ti–O bond. The peak at 667 cm^{-1} refers to the symmetric O–Ti–O stretching vibration while the peaks at 447 cm^{-1} and 505 cm^{-1} are due to the vibration of the Ti–O bond. A prominent peak at 1383 cm^{-1} is related to the Ti-O vibration modes. Two more transmittance bands appeared at about 1600 cm^{-1} and 3400 cm^{-1}. One of these two transmittance bands at 3400 cm^{-1} is attributed to the characteristic vibration of hydroxyl group O-H bond in water molecules, indicating that the drying process did not completely trap the water molecules from the pores of TiO_2 structure, and the other transmittance band at 1600 cm^{-1} is attributed to the bending modes of water (Livage 1988, Kwon 2000, Abazovic et al. 2006, Hamza et al. 2013, Mugundan et al. 2015).

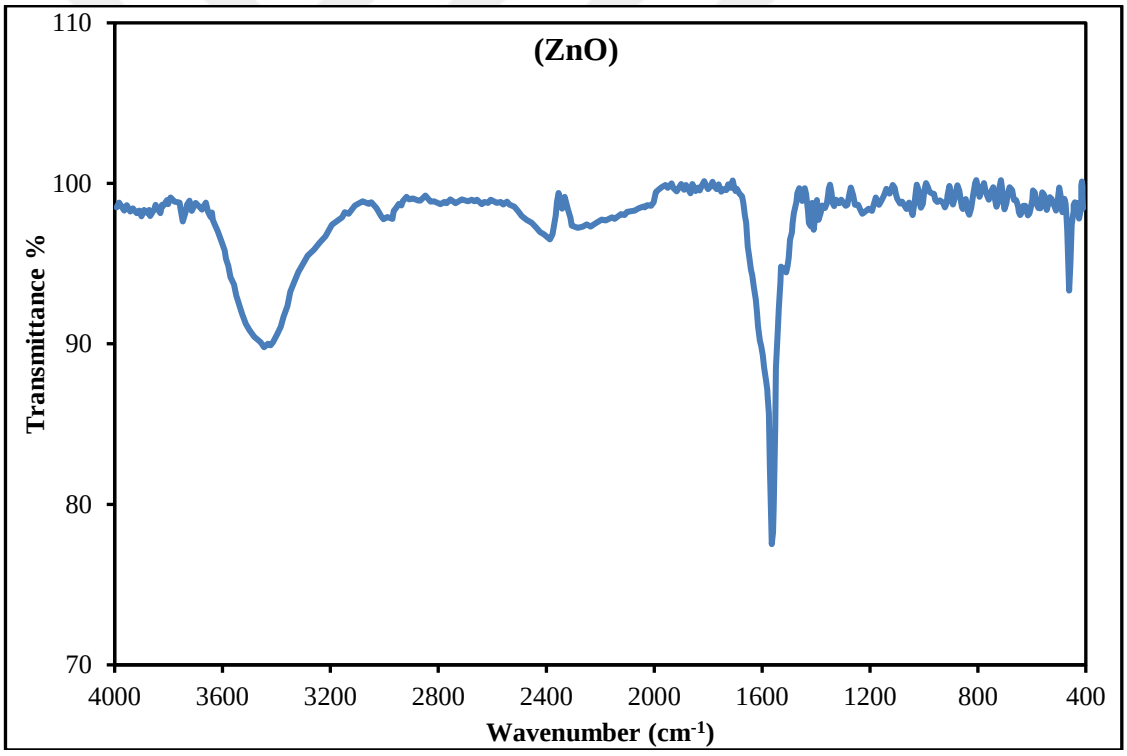

Figure 4.4 FTIR transmittance spectrum of ZnO film

Figure 4.4 shows the FTIR spectrum of the ZnO film. A series of transmittance peaks from 400 to 4000 cm^{-1} can be found on the FTIR spectrum, corresponding to the ZnO structure, carboxyl and hydroxyl groups in materials. To be more specific, the peak at 451 cm^{-1} is due to the characteristic transmittance of Zn–O bond, and a broad band at

3500 cm^{-1} is assigned to the OH stretching mode of hydroxyl group. The peaks between 2830 cm^{-1} and 3000 cm^{-1} are due to the C-H stretching vibration of alkane groups. The peaks present at 1630 cm^{-1} and 1384 cm^{-1} are attributed to the asymmetrical and symmetrical stretching of the zinc carboxylate, respectively. The carboxyl group probably results from reactive carbon-containing plasma species, arising during the synthesis, and the hydroxyl group results from the hygroscopic nature of ZnO. These impurities identified by FTIR are mainly found near ZnO surfaces (Kaschner et al. 2002, Xiong et al. 2006).

Figures 4.5-4.7 show the FTIR spectra of the TiO_2/ZnO nanocomposite films with varying ZnO content (TiO_2/ZnO: 0.75/0.25, 0.5/0.5 and 0.25/0.75). The effect of coupling ZnO with TiO_2 to prepare the TiO_2/ZnO composite film was clear as shown in the FTIR spectra. The FTIR spectra of the nanocomposite films show transmittance peaks for ≡Ti−O−Ti≡ bonds at 550 cm^{-1}, for Zn−Ti−O bonds at 650 cm^{-1}, and for –OH groups at 3400 cm^{-1}. Analysis of the FTIR spectra for the TiO_2/ZnO film samples reveals significant changes in the peak intensities of the relevant bands depending on the ZnO content of the composites. The characteristic features from 447 cm^{-1} to 667 cm^{-1} belonging to the TiO_2 structure and the characteristic feature at 451 cm^{-1} for the ZnO structure also appear on the spectra of the composite films, confirming the presence of both TiO_2 and ZnO in the composite structure. An increase in the ZnO content of the composite gave rise to the following increase in the intensity of the specified peak related to the ZnO structure.

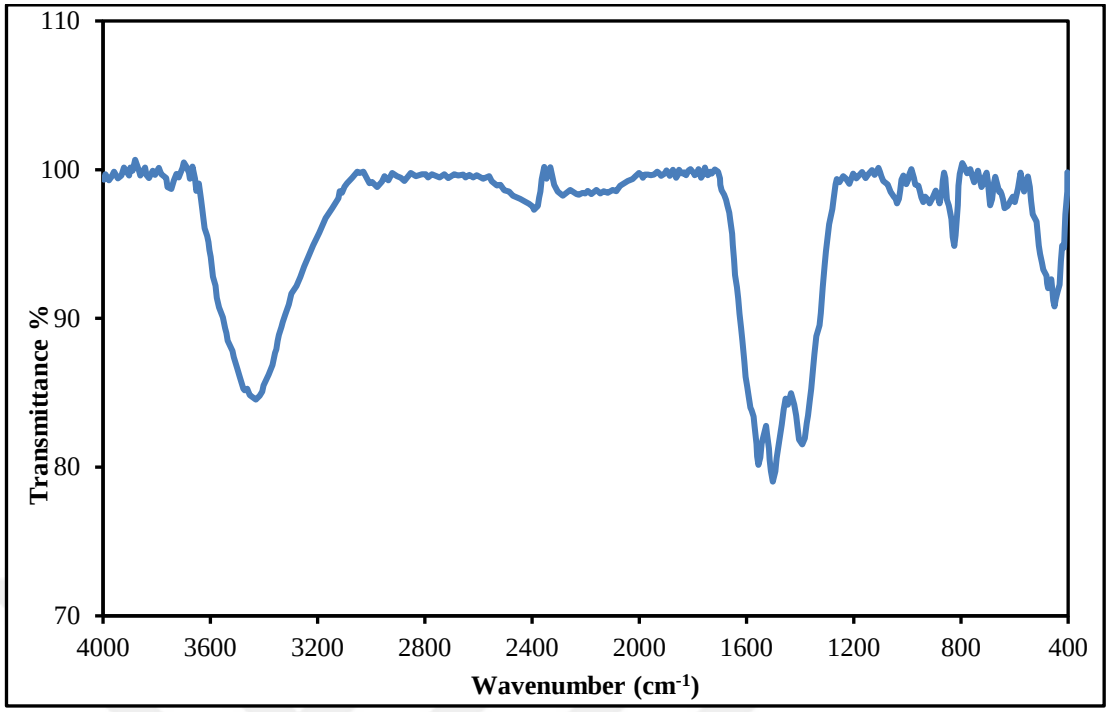

Figure 4.5 FTIR transmittance spectrum of the $0.75TiO_2/0.25ZnO$ composite film sample

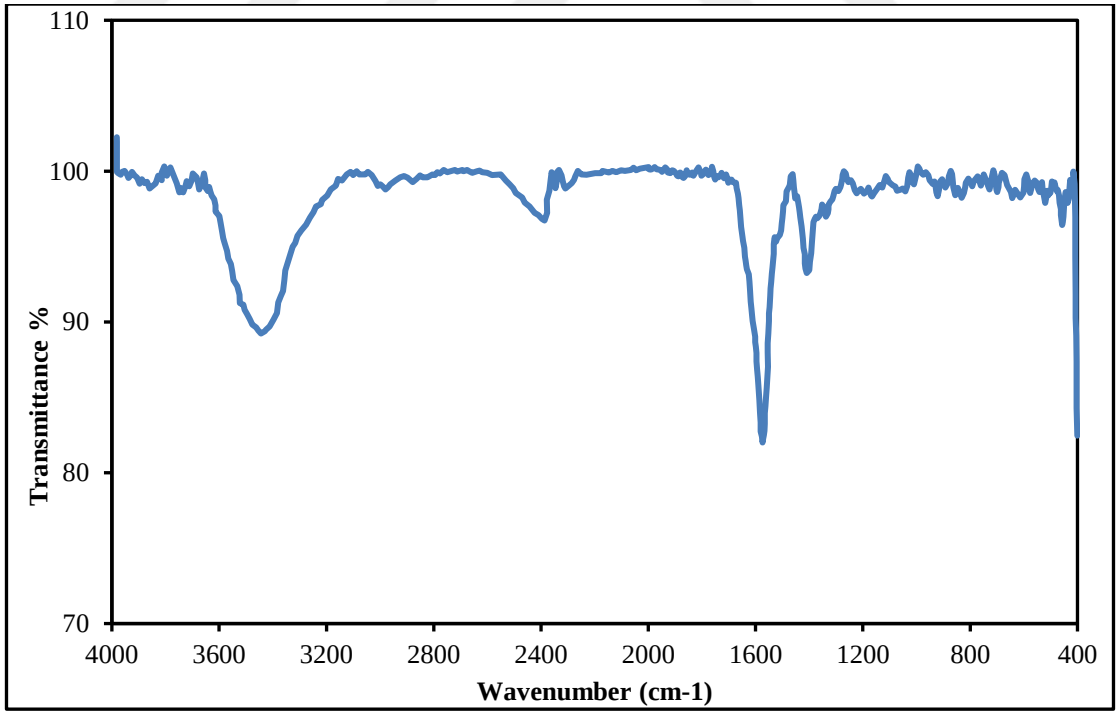

Figure 4.6 FTIR transmittance spectrum of the $0.5TiO_2/0.5ZnO$ composite film sample

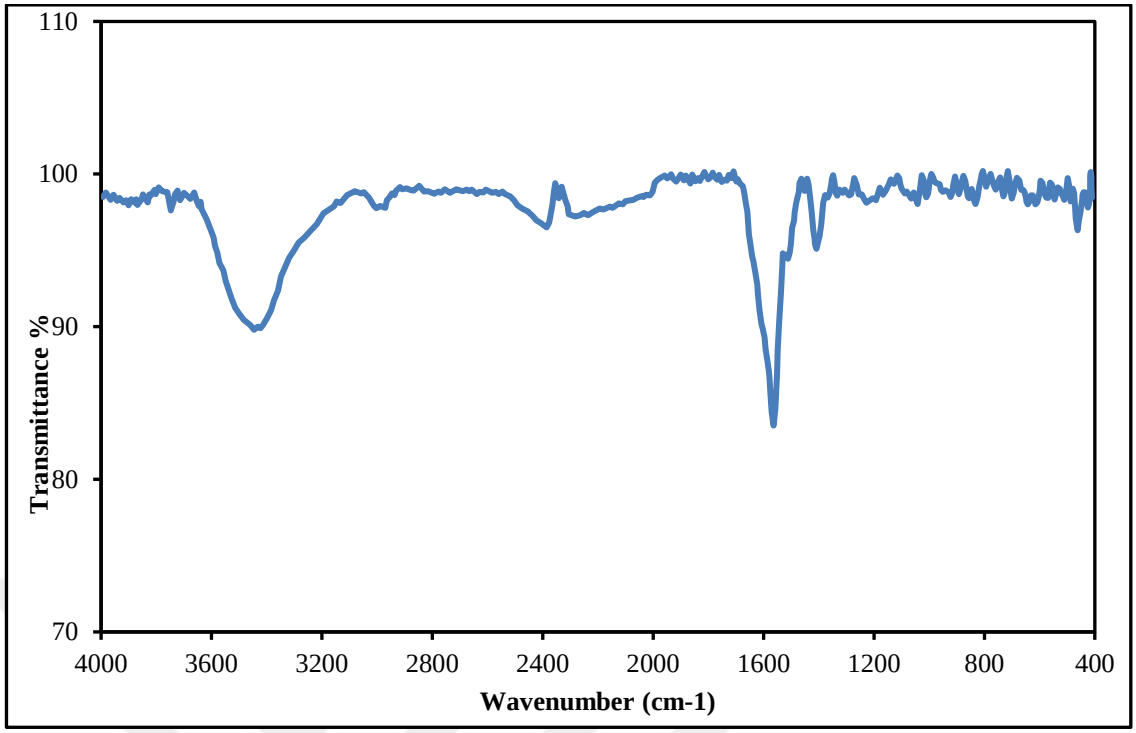

Figure 4.7 FTIR transmittance spectrum of the $0.25TiO_2/0.75ZnO$ composite film sample

4.4 Surface Morphology Analysis (FESEM Measurement)

Scanning electron microscopy (SEM) performs morphological investigation of surfaces with direct visualization. This technique, which is based on electron microscopy, offers several advantages in morphological and sizing analysis. But, this technique provides limited information about the particle size distribution. For the SEM analysis, in this work, the nanoparticles solution was first converted into a film by drop casting method, then mounted on a sample holder and then coated with a conductive metal, gold, using a spray coater. SEM analysis was performed to investigate the nanoparticle size and its distribution in the film structure. In addition, the porosity of the coated film material was investigated by the SEM analysis.

Figure 4.8 shows the field emission scanning electron microscopy (FESEM) images of TiO_2 and ZnO films with two magnifications scale (200 and 500 nm). The particles of these two film samples almost have a spherical shape with high homogeneity. The

FESEM images of the examined samples confirmed the presence of particles of similar size.

Aggregated TiO_2 particles, composed of dozens of nanospheres, can be observed on the FESEM images of TiO_2, revealing the agglomeration tendency of TiO_2 nanoparticles. TiO_2 aggregates with a diameter ranging from 100 nm to 400 nm can be observed on the FESEM images of the sample (Figure 4.8.a). Also, the FESEM images show the existence of various particles of TiO_2 with diameters of around 25-60 nm. On the FESEM images, it can be seen that there are so many voids between TiO_2 particles in its film that it becomes difficult for the mobile charge carriers to travel from one particle to another neighboring particle. The specified voids can suppress the mobility of the charge carriers to travel from particle to particle. Hence, TiO_2 needs be combined with another material suitable for the required application (self-cleaning). This material is ZnO. Combining TiO_2 with ZnO in the composite structure bounces electrons to facilitate the flow of electricity.

The FESEM images of the ZnO film exhibits a more compact film structure compared to the TiO_2 film. According to the FESEM image, the void fraction of the ZnO film should be less than that of the TiO_2 film, which simplifies the stepping process of electrons and causes electric current to occur easily. The ZnO film appears relatively smooth and uniform. It consists of compactly packed and randomly oriented nanocrystallites surface. The FESEM images also illustrate spherical ZnO nanoparticles with diameters of around 10 nm. Compared to TiO_2 nanoparticles, it is seen that the agglomeration tendency of ZnO nanoparticles is weak (Figure 4.8.b).

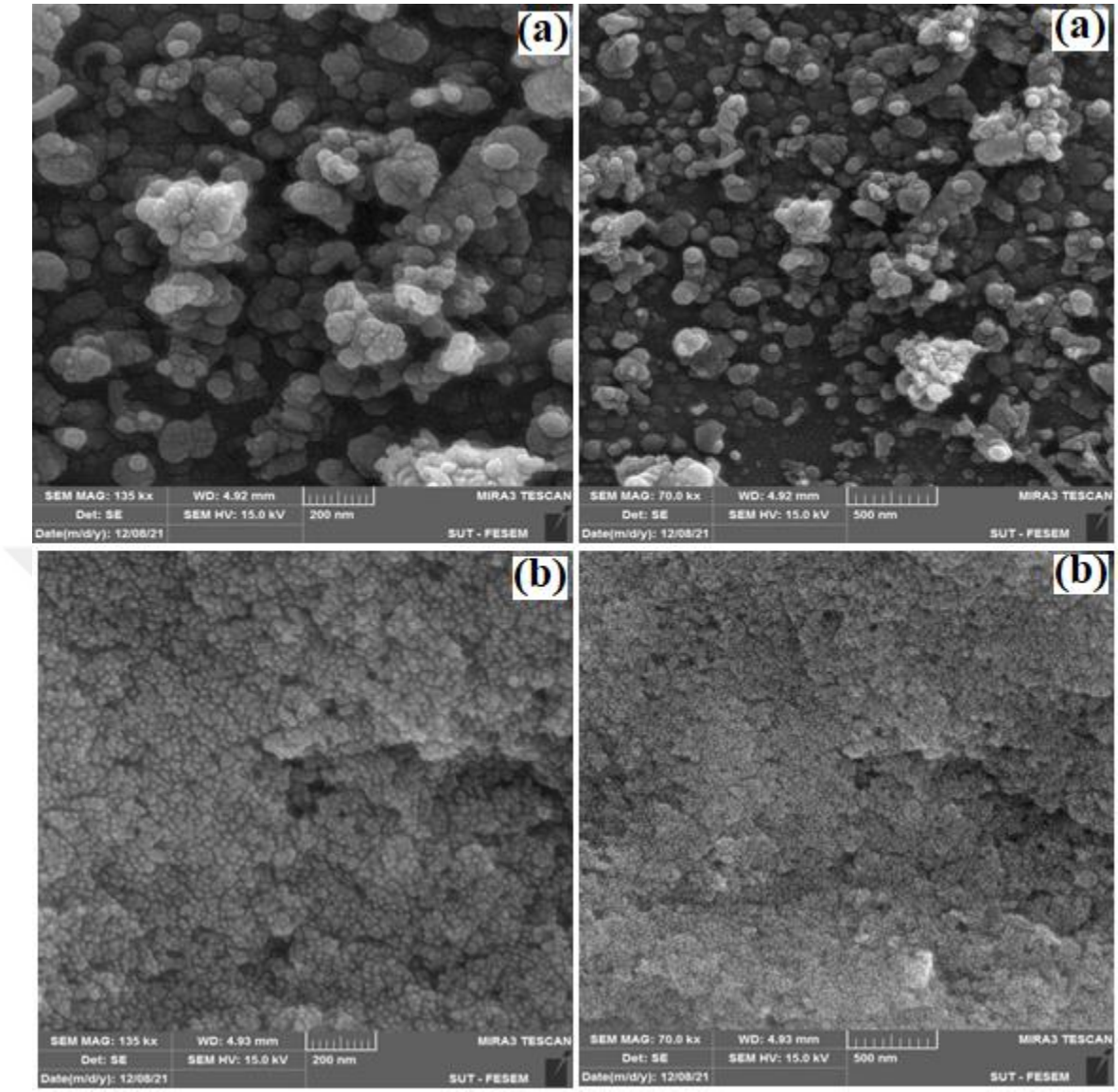

Figure 4.8 Field emission scanning electron microscopy (FESEM) images of (a) TiO_2 and (b) ZnO films

The combination of two materials with different properties will improve the performance of the thin film, which was actually confirmed by the FESEM results of previous studies. According to the previous studies, the surface morphologies of the composite TiO_2/ZnO thin film are more homogeneous, less porous, and the particles are more densely packed, so it does not affect the electron mobility between particles (Retnaningsih and Muliani 2016, Pintilie et al. 2018).

4.5 Optical Properties Analyses (UV-Vis Measurement)

This section describes the effect of mixing ratios of ZnO to TiO_2 on the optical properties of the nanocomposite films, which were prepared by drop casting on glass substrate. The common optical parameters like absorption coefficient (α) and optical energy gap ($E_g^{opt.}$) can be determined by studying the UV-visible absorption spectra.

According to the absorbance spectrum (Figure 4.9), pure TiO_2 and pure ZnO films absorbed the incoming light below 400 nm. When comparing both pure film samples, the absorbance of pure ZnO film in the UV visible region is slightly higher than that of pure TiO_2 film. The composite film samples exhibited similar absorbance trend. The incident light was absorbed by at least the $0.25TiO_2/0.75ZnO$ composite film sample, especially between 400-600 nm.

Figure 4.10 exhibits the transmittance spectrum of the film samples. The average transmittance and the average reflectance of the $0.25TiO_2/0.75ZnO$ film is the highest and the lowest percentages, respectively, in the range of 300-900 nm (Figure 4.10 and 4.11). This transmittance of the $0.25TiO_2/0.75ZnO$ composite film is followed by the TiO_2 film. Among the film samples, the $0.75TiO_2/0.25ZnO$ composite film exhibits slightly lower transmittance and higher reflectance. As the ZnO content of the composite increases, both the visible and the UV light that could be transmitted through the samples increase significantly. As the wavelength of the incoming light increases, the transmittance increases and the reflectance decreases for all samples and become constant throughout the irradiation until 900 nm. The composite film samples were highly transparent with more than 80% transmittance and with less than 15% reflectance in the visible light region (4.10 and 4.11). The composite film samples appear to have the potential to be applied as self-cleaning coatings on solar cells, as their self-cleaning property requires low reflectivity and higher transmittance.

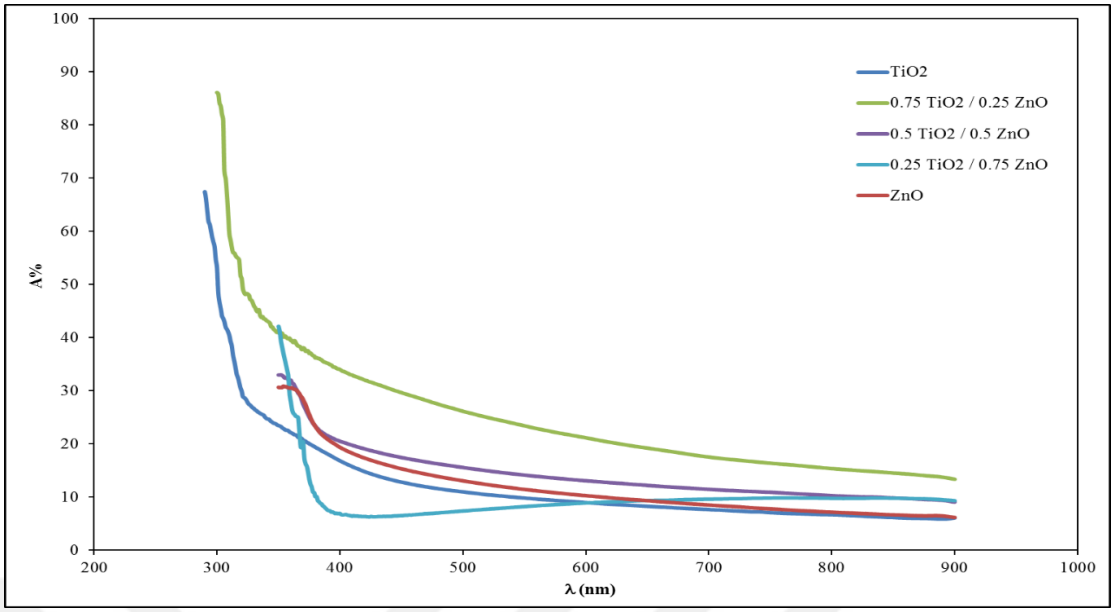

Figure 4.9 Absorption spectra of TiO_2, ZnO and TiO_2/ZnO films

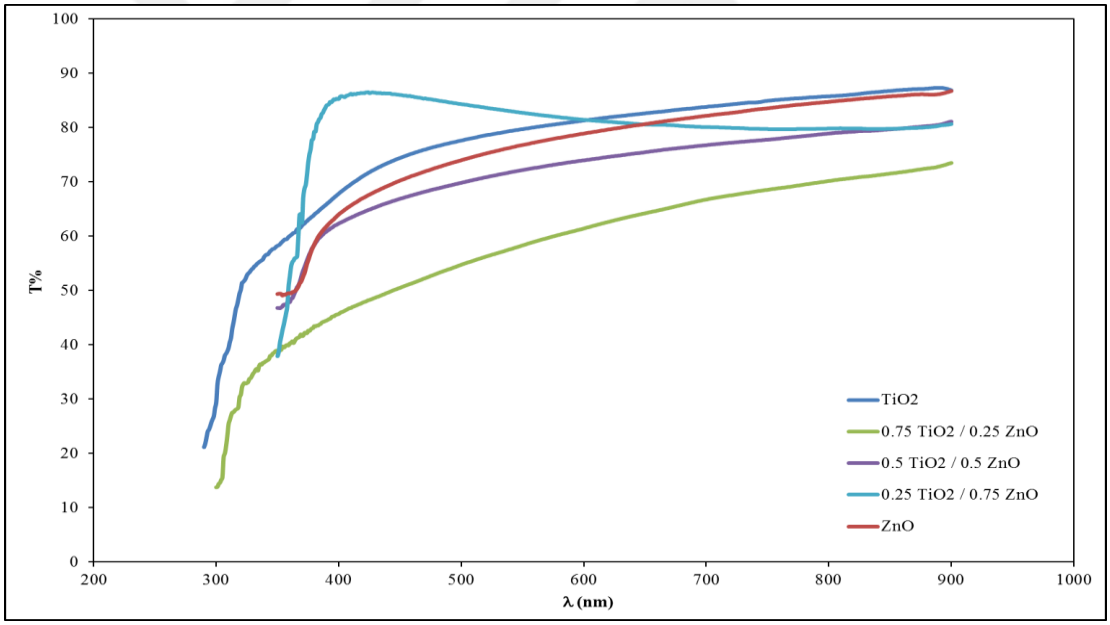

Figure 4.10 Transmittance spectra of TiO_2, ZnO and TiO_2/ZnO films

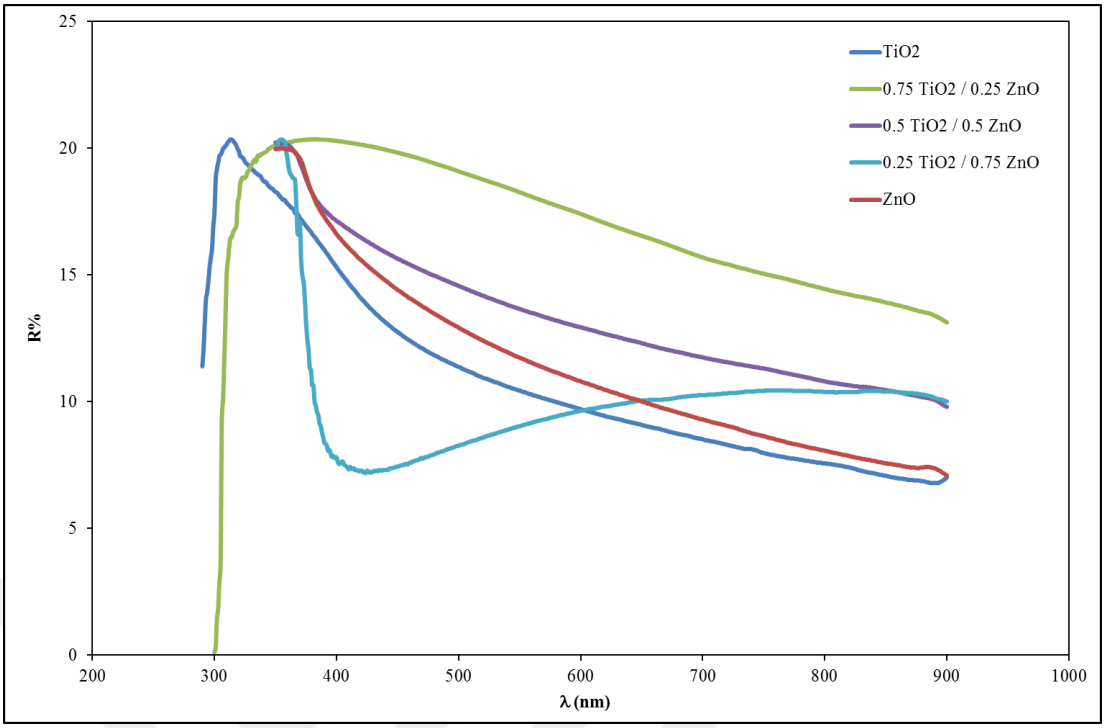

Figure 4.11 Reflectance spectra of TiO_2, ZnO and TiO_2/ZnO films

The absorption coefficient α was determined from the high absorption region, that is, at the principal absorption edge of the films. The calculated optical absorption coefficient using the UV-visible absorption spectrum of the prepared samples is illustrated in Figure 4.12. Pure TiO_2 film responded to the UV light. Coupling TiO_2 with ZnO shifted the absorption threshold of TiO_2 slightly towards the visible regime. The $0.75TiO_2/0.25ZnO$ composite exhibits slightly high absorption both in the UV light region and in the visible light region. Figure 4.12 shows that both ZnO and the remaining TiO_2/ZnO composites exhibited relatively low visible light absorption. Coupling TiO_2 with ZnO suppressed the absorption performance of pure TiO_2 film. The reduction in the visible light absorption of the composite film samples confirmed that combining TiO_2 with ZnO tuned the optical band gap of the composite films and made them less sensitive to the visible light.

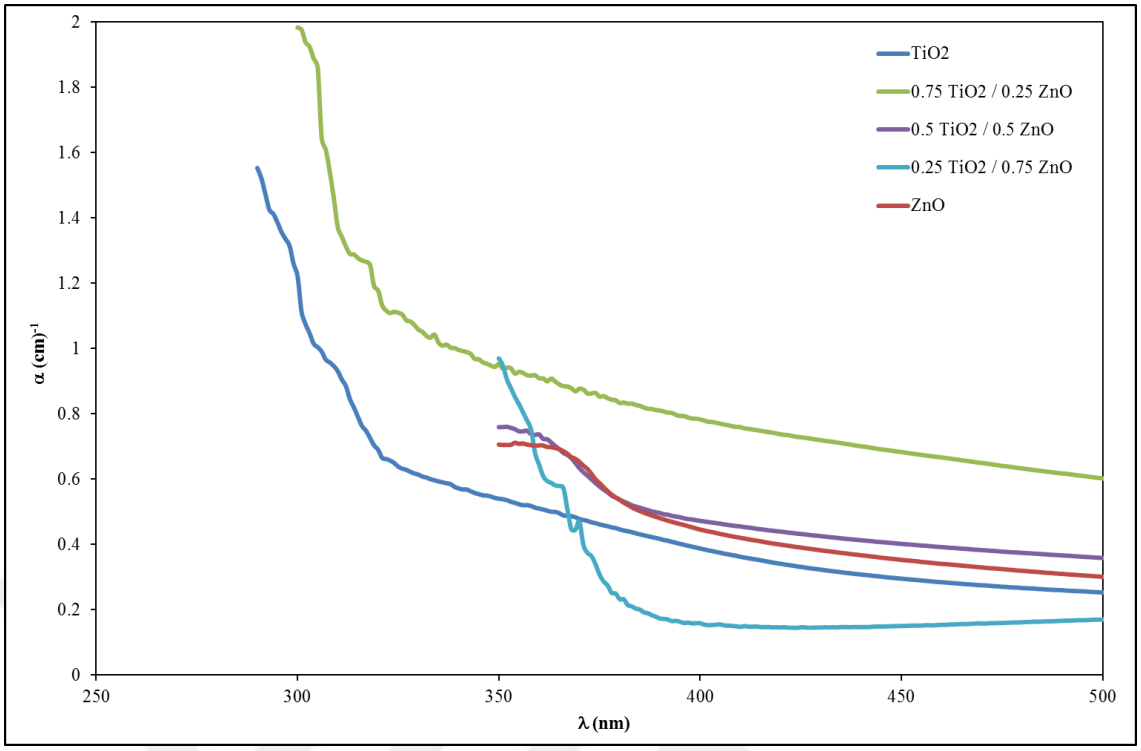

Figure 4.12 Absorption coefficient of TiO_2, ZnO and TiO_2/ZnO films

The effective red shift of the optical absorption edge for the composite films might be one of the indicators for the enhanced photocatalytic activity of the prepared composite films (Khan and Cao 2013). The increase in photocatalytic activity can help the film sample get rid of organic pollutants on the solar cell through photocatalytic degradation reactions. In addition, the red shift is also important for the photoinduced superhydrophilicity. On the other hand, the red shift has the potential to lower the amount of the transmitted light that needs to be absorbed by the solar cell. Therefore, the red shift can be detrimental to the efficiency of the solar cell.

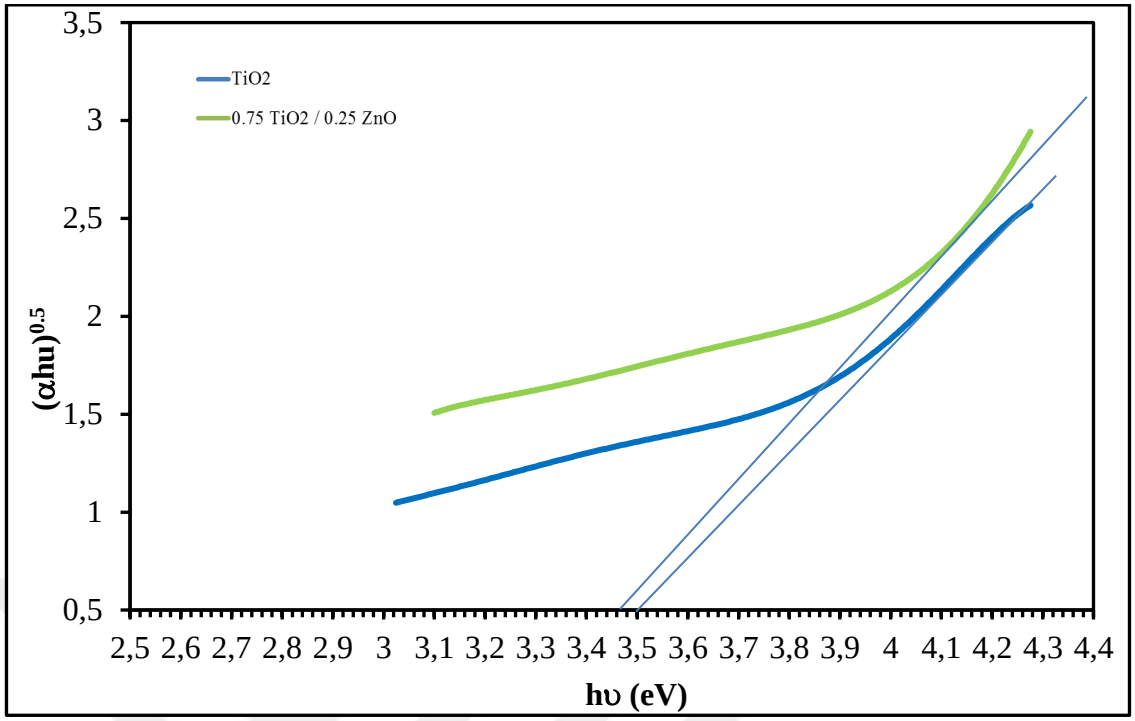

Figure 4.13 Indirect optical energy gap of TiO_2 and $0.75TiO_2/0.25ZnO$ film

The optical energy gap values ($E_g^{opt.}$) for prepared films have been determined by using the Tauc equation. Since the prepared material is a composite of TiO_2 and ZnO in which ZnO is a direct band gap material and TiO_2 is an indirect band gap material, the calculation of the optical band gap energy was done for both conditions, namely for the direct and indirect band gaps. It was realized that the indirect band gap calculation was more suitable for the optical band gap calculation of the samples with low ZnO concentration (0 and 25 wt.%). By using the indirect band gap calculation, the optical band gap of the TiO_2 film and the $0.75TiO_2/0.25ZnO$ composite film was determined as 3.5 eV and 3.46 eV, respectively (Figure 4.13). This is because of the presence of TiO_2 as major component in the sample, which is an indirect band gap material. As the composite content of ZnO increased to 50, 75 and 100 wt.%, the direct band gap calculation was more suitable to calculate the optical band gap energy, and the value of the band gap for the $0.50TiO_2/0.50ZnO$ composite film, the $0.25TiO_2/0.75ZnO$ film and the ZnO film was found to be 3.23 eV, 3.98 eV and 3.20 eV, respectively (Figure 4.14). Thus, the variation of ZnO content in the film sample caused a change in the optical band gap energy. With increasing the ZnO content, the optical band gap has a value

between 3.5eV to 3.98eV. This indicates that tuning in band gap is possible with the variation of the ZnO content in the TiO_2/ZnO nanocomposite. The values of the optical band gap energy are listed in Table 4.1.

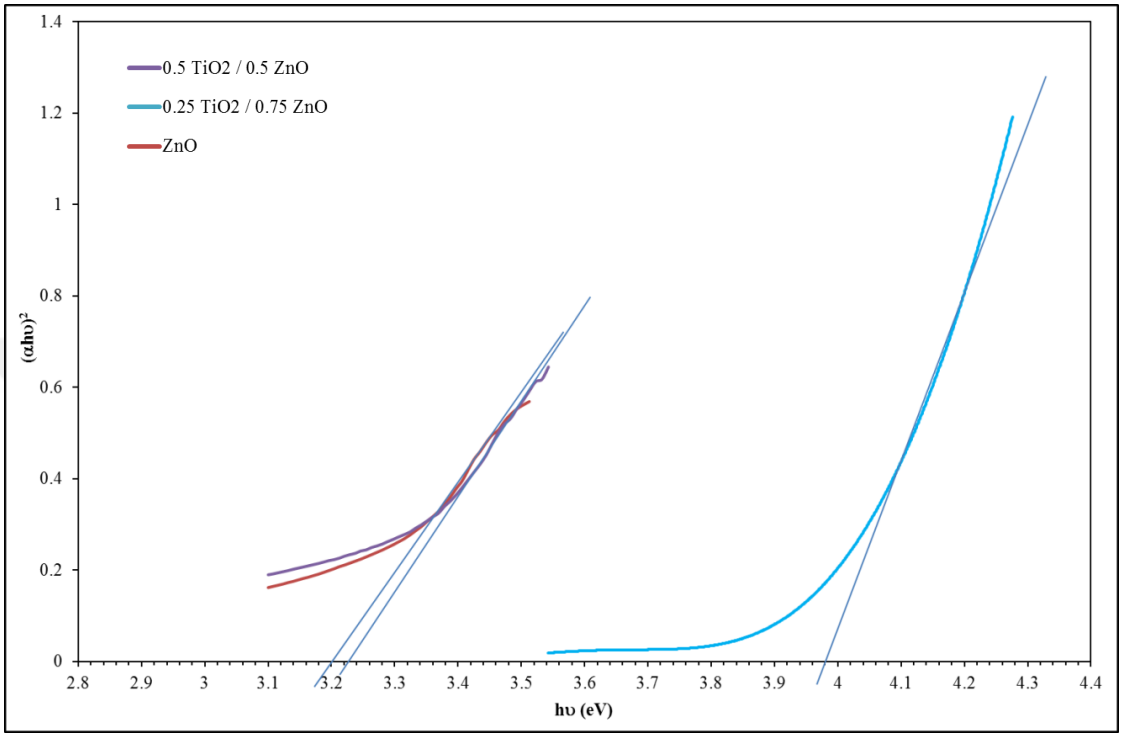

Figure 4.14 Direct optical energy gap of ZnO, 0.5TiO_2/0.5ZnO and 0.25TiO_2/0.75ZnO films

Table 4.1 Optical energy gap of TiO_2, ZnO and TiO_2/ZnO films with varying ZnO content

Sample	Energy gap (eV)	Transition type
TiO_2	3.5	indirect
0.75TiO_2/0.25ZnO	3.46	
0.50TiO_2/0.50ZnO	3.23	direct
0.25TiO_2/0.75ZnO	3.98	
ZnO	3.2	

From the absorption spectrum of the film samples prepared using the drop casting technique, the optical parameters such as the refractive index (n) and the extinction coefficient (k) have been calculated. It was observed that the refractive index of the films generally decreased with the increase of the wavelength of the incident light, except for the $0.25TiO_2/075ZnO$ film sample, where the refractive index increased with increasing the wavelength of the incoming light (Figure 4.15). The low value of packing density of the film samples might be the possible reason for the observed decrease in the refractive index value with decreasing the photon energy of the incoming light (Bhandari and Panwar 2021). At 600 nm wavelength, the refractive index value of the TiO_2, ZnO, $0.75TiO_2/0.25ZnO$, $0.5TiO_2/0.5ZnO$ and $0.25TiO_2/0.75ZnO$ film samples were found out to be almost 1.9, 2.0, 2.5, 2.2 and 1.9, respectively (Figure 4.15). The refractive index mainly depends on impurities and voids in the films. The specified imperfections in the film structure might have been incorporated during the film growth process. The combined effect of crystal structure, imperfections, film-substrate interaction and film coating conditions might be responsible for the changes in refractive index values of the prepared film samples (Bhandari and Panwar 2021).

To improve the performance of solar cells, the coated film layer might also act as an antireflection coating (ARC). The refractive index contrast between air and the coated film on the solar cell leads to reflection losses. The objective of an antireflecting coating is to reduce the refractive index contrast between the coated film and air. An alternative to reducing reflection losses when the incident light enters the coated film is to cover the solar cell surface with a single-layer coating with a medium refractive index between that of air (1.0) and glass (1.5) (Tsakalakos 2012). According to the refractive index values (Figure 4.15), pure TiO_2 and pure ZnO films do not seem to be suitable to act as an antireflection coating on the solar cell. Another alternative to improve the solar cell efficiency is to cover its surface with a layer of graded refractive index (Tsakalakos 2012). TiO_2 and ZnO with different refractive index values might form a composite layer on the solar cell with a graded refractive index, which enables the composite layer to act as an anti-reflective coating and improve the solar cell efficiency.

The extinction coefficient is a measure of the incoming light lost due to scattering and absorption per unit volume of the coated film. The relation between the extinction coefficient and wavelength for the TiO_2, ZnO, TiO_2/ZnO composite films is shown in Figure 4.16. From this figure it is found that the extinction coefficient (k) takes the similar behavior of the corresponding absorption coefficient. The extinction coefficients did not change much in the 500-900 nm and increased slightly at the lower wavelengths due to absorption (Mohamed et al. 2013). High values of the extinction coefficient for the film samples in the UV light range exhibit that these films are opaque in this range and absorbed or scattered more amount of the incoming photons of the light. Only, the extinction coefficient of the $0.25TiO_2$/0.75ZnO composite sample exhibited a different trend with the wavelength. The extinction coefficient decreased with an increase in the photon energy of the incoming light. At 600 nm wavelength, the extinction coefficient (k) value of the TiO_2, ZnO, $0.75TiO_2$/0.25ZnO, $0.5TiO_2$/0.5ZnO and $0.25TiO_2$/0.75ZnO film samples were found out to be almost 0.01, 0.012, 0.023, 0.015 and 0.01, respectively (Figure 4.15). Based on the extinction coefficient values, the $0.25TiO_2$/0.75ZnO composite film seems to be a more suitable candidate for the self-cleaning surface coating application on solar cells.

Knowledge of the optical properties like the dielectric constant is also important in the design of instruments in optoelectronic as well as solar cell applications. The absorption data can also be utilized to obtain the dielectric constant. This optical property is another basic parameter of a material because it is strongly related to the electronic of the materials (Akin and Sonmezoglu 2012). Figure 4.17 and 4.18 show the variation of the real (ε_r) and imaginary (ε_i) parts of the dielectric constant with the wavelength for the TiO_2, ZnO and TiO_2/ZnO composite films. The behavior of ε_r and ε_i is the same as that of refractive index (n) and extinction coefficient (k), respectively, with the wavelength. According to Figure 4.17, the real part of the dielectric constant for all samples is found to decrease slightly with the wavelength except the $0.25TiO_2$/0.75ZnO composite sample, at which the real part of the dielectric constant increased with the wavelength. The imaginary part of the dielectric constant behaves similarly to the real part of the dielectric constant. It was observed that the values of the real part of the dielectric constant were considerably higher than the values of the imaginary part (Akin

and Sonmezoglu 2012). The real part of the dielectric constant (ε_r) varies depending on the difference between the square of the refractive index (n) value and the square of the extinction coefficient (k) value. Since the refractive index value is greater than the extinction coefficient value, the refractive index value has been more decisive in calculating the real part of the dielectric constant. On the other hand, the imaginary part (ε_i) of the dielectric constant mainly depends on the product of the refractive index and the extinction coefficient, which is related to the variations of the absorption coefficient.

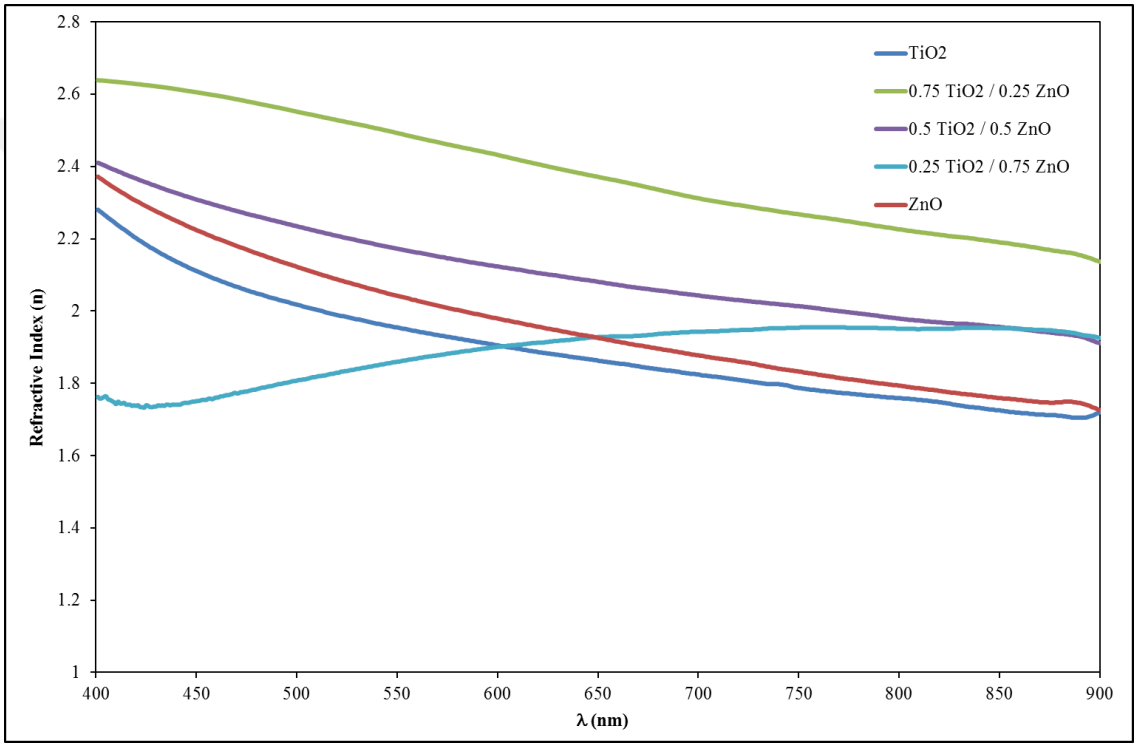

Figure 4.15 Refractive index of TiO_2, ZnO and TiO_2/ZnO films

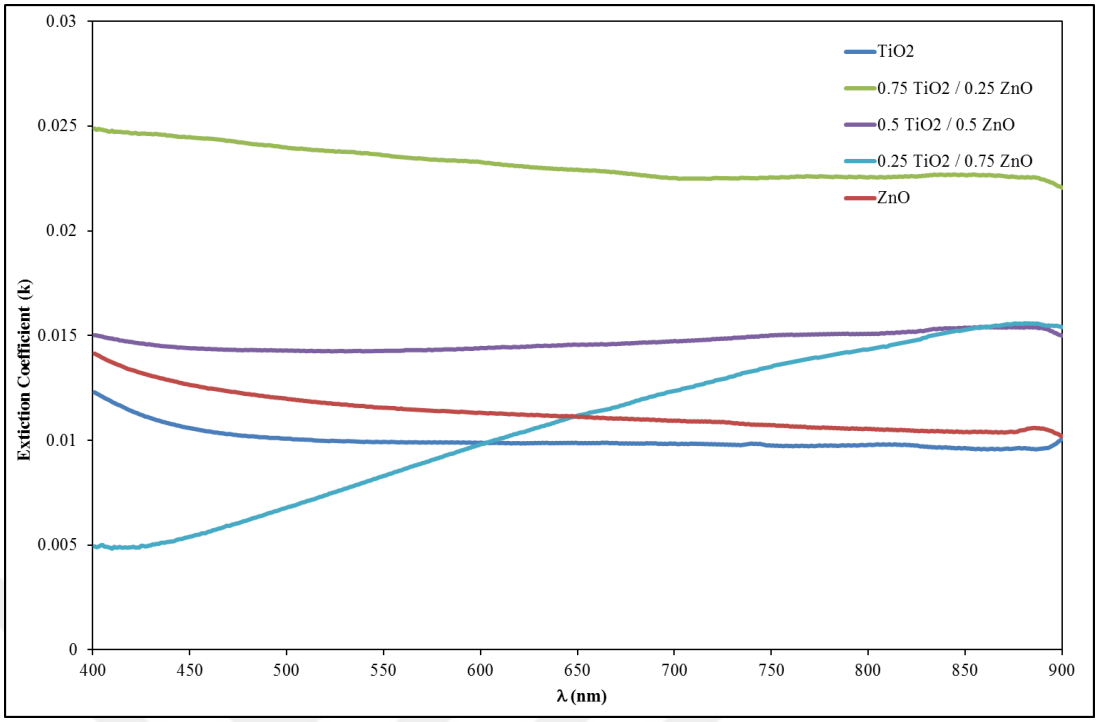

Figure 4.16 Extinction coefficient of TiO_2, ZnO and TiO_2/ZnO films

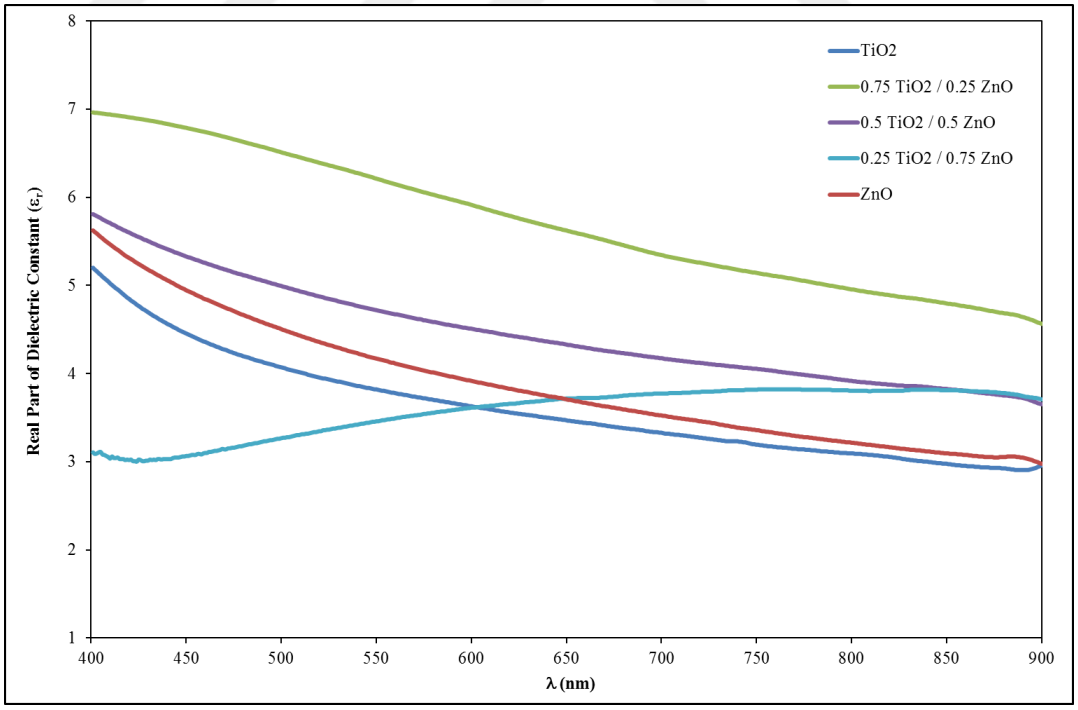

Figure 4.17 Real part of dielectric constant of TiO_2, ZnO and TiO_2/ZnO films

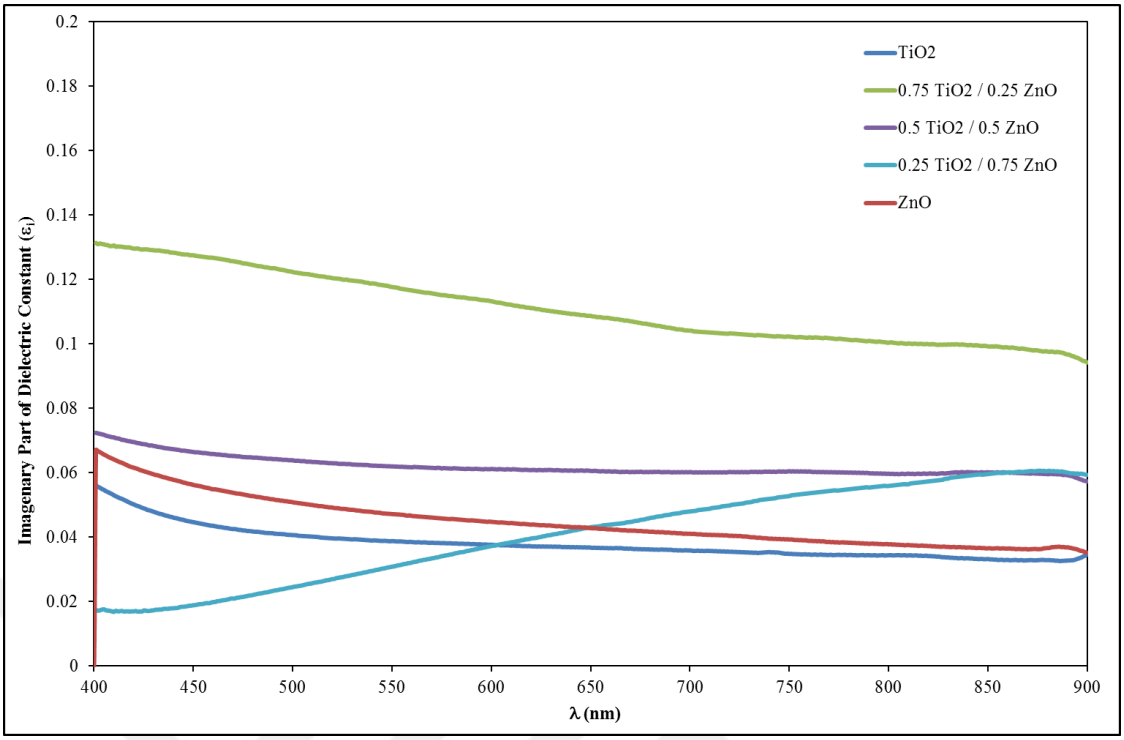

Figure 4.18 Imaginary part of dielectric constant of TiO_2, ZnO and TiO_2/ZnO films

4.6 Photoluminescence Analysis

In addition to UV-Vis spectroscopy to get more accurate values of the optical energy band gap, the photoluminescence spectrum of TiO_2 and ZnO films were also studied. Photoluminescence spectrum or emission spectrum has great significance since it provides information about the optical energy band gap and trapping energy levels in the optical energy gap. The optical energy gap value, obtained from the photoluminescence spectrum, is more accurate than that of the optical band gap value, calculated using the Tauc equation. The behaviour of variation of the optical energy gap obtained from the photoluminescence spectrum is similar to the behavior of the optical energy gap obtained from the UV-Vis spectrum. The optical energy gaps were calculated using equation (3.5) and the values of E_g^{opt} of TiO_2 and ZnO were 3.406 eV (Figure 4.19) and 3.179 eV (Figure 4.20), respectively. These values are also consistent with the optical band gap values from the literature.

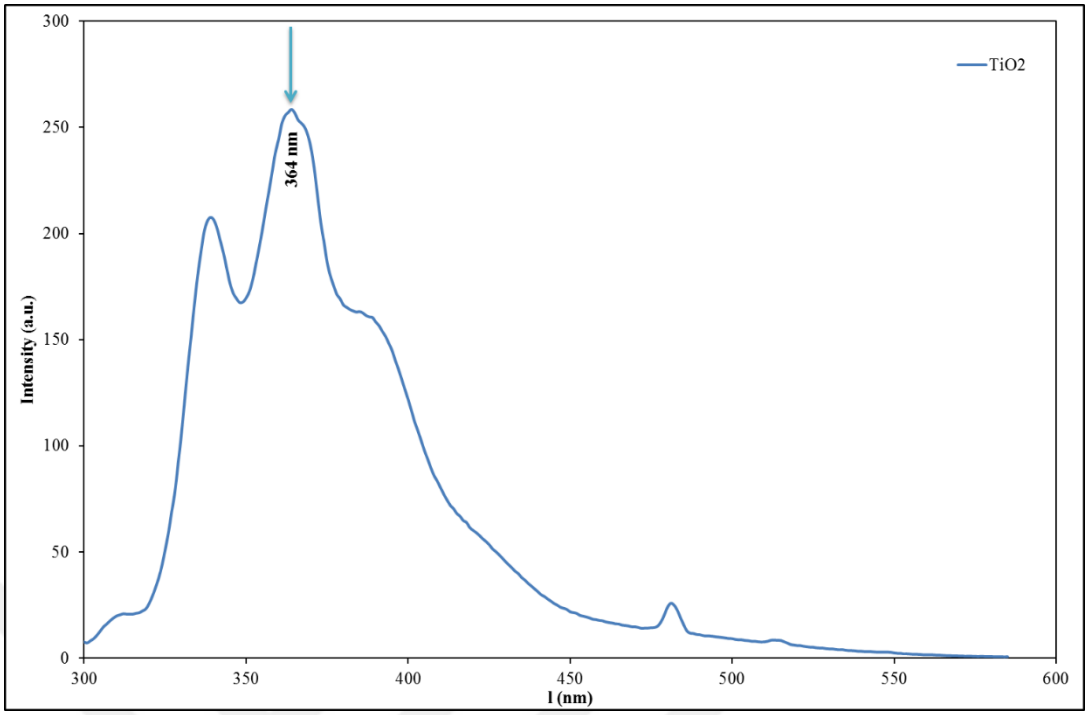

Figure 4.19 Photoluminescence spectrum of TiO_2

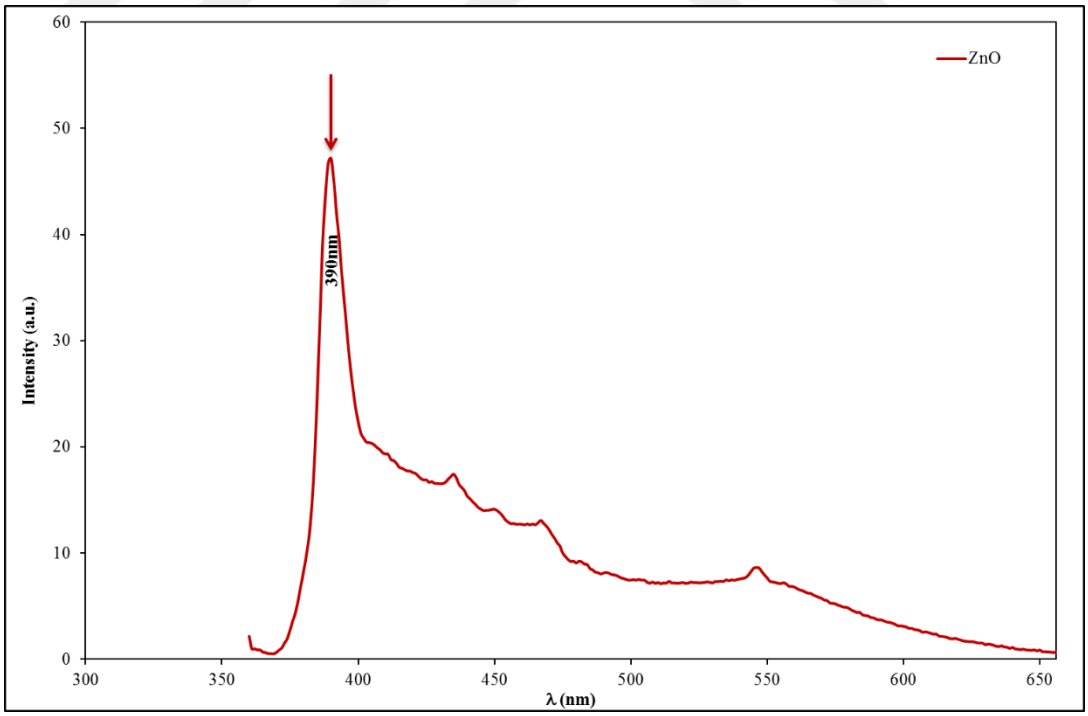

Figure 4.20 Photoluminescence spectrum of ZnO

4.7 Contact Angle Analysis

Water contact angles of the film samples, TiO_2, ZnO and TiO_2/ZnO with varying ZnO content, were measured before and after UV light irradiation supplied from a UV source (18 W) using the low-projection method. In this work, the water contact angles of the film samples exposed to UV light irradiation in different time periods were evaluated using the image J analysis software as shown in Figures 4.21-4.23 and the results were listed in Table 4.2. The contact angles of each group of the prepared samples were evaluated after storing the samples in the dark for ten days.

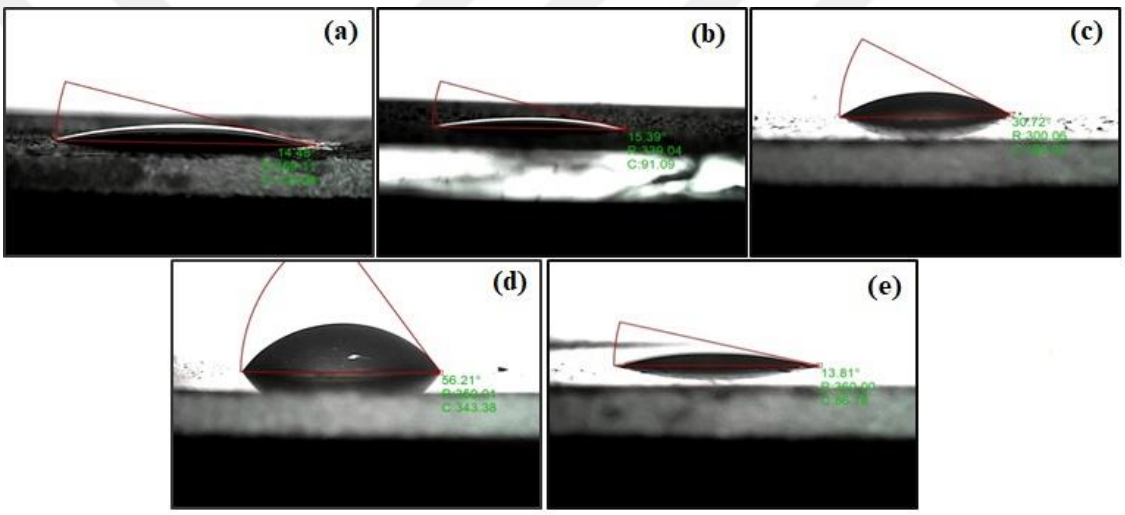

Figure 4.21 Images of water droplet on (a) TiO_2 (b) ZnO (c) $0.75TiO_2$/0.25ZnO (d) $0.50TiO_2$/0.50ZnO and (e) $0.25TiO_2$/0.75ZnO films before UV light irradiation

The wettability of the as-prepared film samples is a significant feature for analyzing the self-cleaning property. The wettability of the film samples can be evaluated by measuring the water contact angle (Appasamy et al. 2020). The contact angle results show that all the films have hydrophilic surface character because the contact angles are less than 90° and approach to superhydrophilic feature in certain samples such as the TiO_2 film and the ZnO film after 15 min of UV light illumination and the $0.25TiO_2$/0.75ZnO composite film after 15 min of UV light illumination.

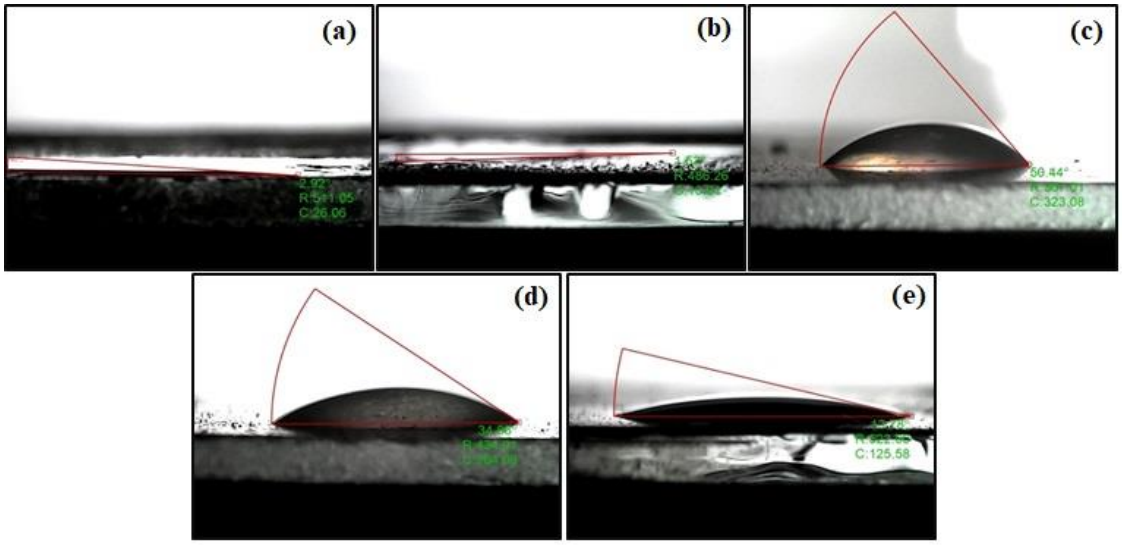

Figure 4.22 Images of water droplet on (a) TiO_2 (b) ZnO (c) $0.75TiO_2/0.25ZnO$ (d) $0.50TiO_2/0.50ZnO$ and (e) $0.25TiO_2/0.75ZnO$ films after UV light irradiation for 15 min

It was realized that all the film samples became more hydrophilic after exposure to UV light irradiation for 15 and 30 min, respectively. The contact angles of the film samples with TiO_2, ZnO, $0.75TiO_2/0.25ZnO$, $0.50TiO_2/0.50ZnO$, $0.25TiO_2/0.75ZnO$ were 14.48º, 15.39º, 56.21º, 30.72º and 13.31º, respectively, prior to UV light irradiation. The contact angle value of the specified samples decreased to 7.85º, 8.31º, 36.67º, 28.90º and 7.95º, respectively, after UV light irradiation for 30 min. On the other hand, the composite film samples, $0.75TiO_2/0.25$ ZnO and 0.50 $TiO_2/0.50$ ZnO, revealed higher water contact angle than that of TiO_2 and ZnO. The rough surface structure that can be obtained with the composite structure might cause an increase in the water contact angle. According to the water contact angle results, it can be concluded that the wettability property enhanced with the content of ZnO in the composite structure. In addition, all the film samples possess the self-cleaning feature.

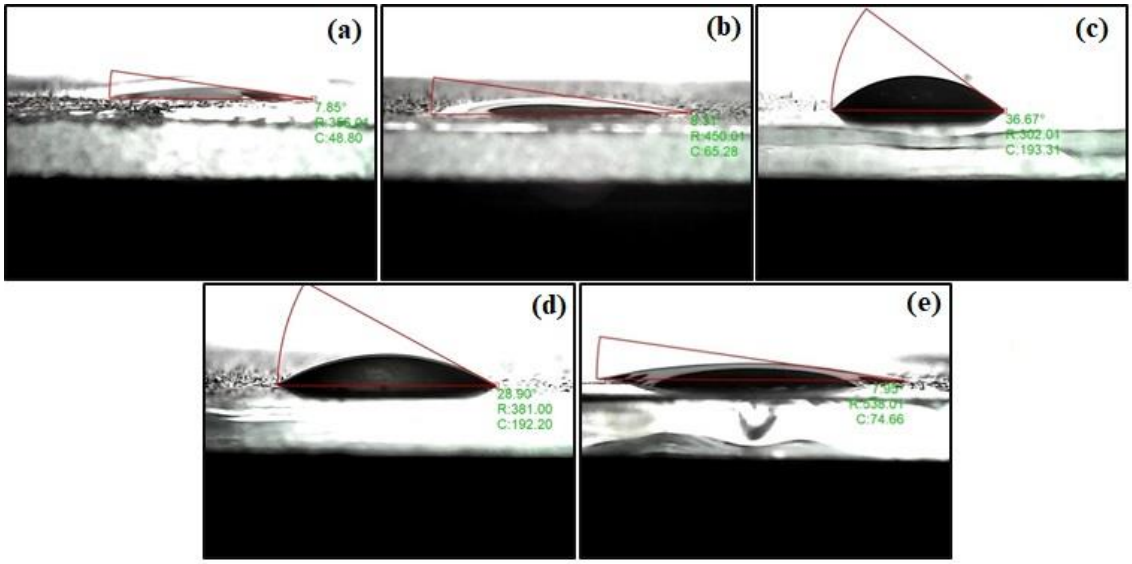

Figure 4.23 Images of water droplet on (a) TiO_2 (b) ZnO (c) $075TiO_2/0.25ZnO$ (d) $0.50TiO_2/0.50ZnO$ and (e) $0.25TiO_2/0.75ZnO$ films after UV light irradiation for 30 min

Table 4.2 Water contact angle values of the film samples before and after UV light illumination

Sample	**Before UV-illumination**	**15 min UV-illumination**	**30 min UV-illumination**
TiO_2	14.48	2.92	7.85
ZnO	15.39	1.52	8.31
$0.75TiO_2/0.25ZnO$	56.21	50.44	36.67
$0.50\ TiO_2/0.50$ ZnO	30.72	34.96	28.90
$0.25\ TiO_2/0.75$ ZnO	13.31	13.78	7.95

4.8 Sliding Angle Analysis

The sliding angle of the film samples was another important feature to characterize the self-cleaning property of the surfaces. In the outdoor environment, the pollutant particles on the film surface can be cleaned with rain droplets run off. The low sliding angle indicates that the droplets can easily flow on the film surface and remove the pollutants from the film surface (Yang et al. 2014). The sliding angles of the prepared

films were measured. In this experiment, an inclined plate was used with a pitch from 0 to 90 degrees. The droplet volume of 5 µl was placed by the method of low projection. The results examined during this study indicated that the sliding angles are strongly affected by the surface morphology, surface area and water contact angle, where sliding angles for water droplets increase with decreasing the water contact angle. Table 4.3 shows the sliding angle measurement results of TiO_2, ZnO and TiO_2/ZnO films with varying ZnO content. All the sliding angles are below 90º. The optimum result was also for the $0.25TiO_2/0.75ZnO$ composite sample. The 5 µl water droplet can run off from the surface of the $0.25TiO_2/0.75ZnO$ composite film when the plate was inclined 46º. The sliding angle of the composite films decreased with the increasing the content of ZnO in the composite. On the other hand, the sliding angle of water droplets on the composite film surface were consistently lower than that on the ZnO film surface. It might also be attributed to the surface roughness of the composite films. According to the study carried out by Miwa and her coworkers (2000), surface microstructures that can trap air are important to obtain surfaces with low sliding angle (Miwa et al. 2000).

Table 4.3 Sliding angles of water droplets on TiO_2, ZnO and TiO_2/ZnO films with varying ZnO content

Sample	**Sliding Angle**
Glass substrate	35º
TiO_2	69º
ZnO	84º
$0.75TiO_2/0.25ZnO$	80º
$0.50TiO_2/0.50ZnO$	77º
$0.25TiO_2/0.75ZnO$	46º

4.9 Solar Cell Efficiency Analysis

Amorphous silicon solar cells are subject to degradation over time, intrinsic instability, and low efficiency. In addition, silicon reflects almost 36% of light at a wavelength of 550 nm, leading to a significant loss in solar cell efficiency. Anti-reflective coatings

(ARCs) not only help to capture incoming multi-directional light, but also play an important role in surface passivation, reducing reflection to <4% in the 300-800 nm wavelength range. Due to the distinctive physical physiognomies of metal oxides, the researchers used a combination of different inorganic metal oxides with high, low and medium refractive indices to model AR coatings in the desired wavelength range in the literature (Anonymous 2023d, Khan et al. 2019).

Some of the metal oxides like TiO_2, ZnO, Al_2O_3, indium tin oxide (ITO), Ta_2O_5 and various nanostructured metal oxide films possess an excellent antireflective property, and they are used as antireflective coatings owing to their well matching refractive index, low coating cost, stability and hardness. The specified metal oxides also exhibit excellent transmittance and mechanical resistance (Anonymous 2023d, Richards et al. 2000, Zallen and Moret 2006, Shinde et al. 2008)

Solar panels are mainly utilized for outdoor applications, and the solar panels are mostly exposed to dust, fog and haze pollution including various organic contaminants (Appasamy et al. 2020). The water contact angle results revealed the self-cleaning efficiency of the as-prepared composite films before and after UV light irradiation. It is expected that the prepared films will not adversely affect the efficiency of the solar cells they are coated with, as well as having a self-cleaning feature. By examining the I-V characteristics of the solar cell on which the as-prepared films were coated, the effect of the as-prepared films on the efficiency of the solar cell was investigated.

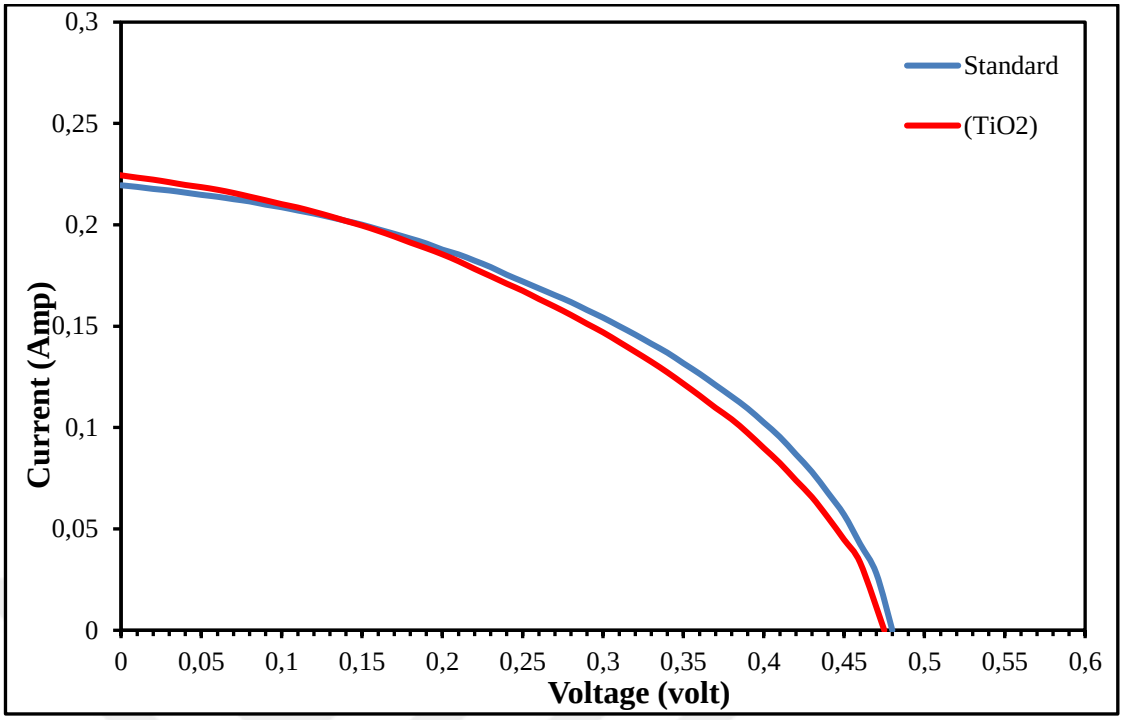

Figure 4.24 I-V characteristics curve of TiO_2/a-Si compared to a-Si

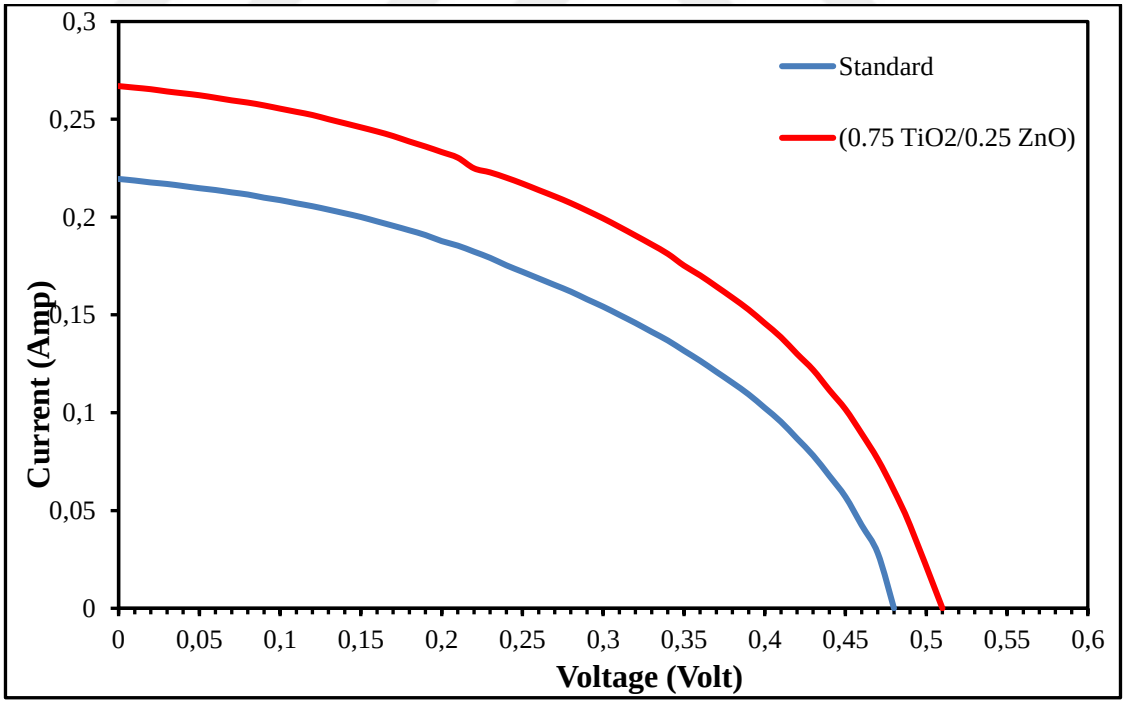

Figure 4.25 I-V characteristics curve of 0.75TiO_2/0.25ZnO/a-Si compared to a-Si

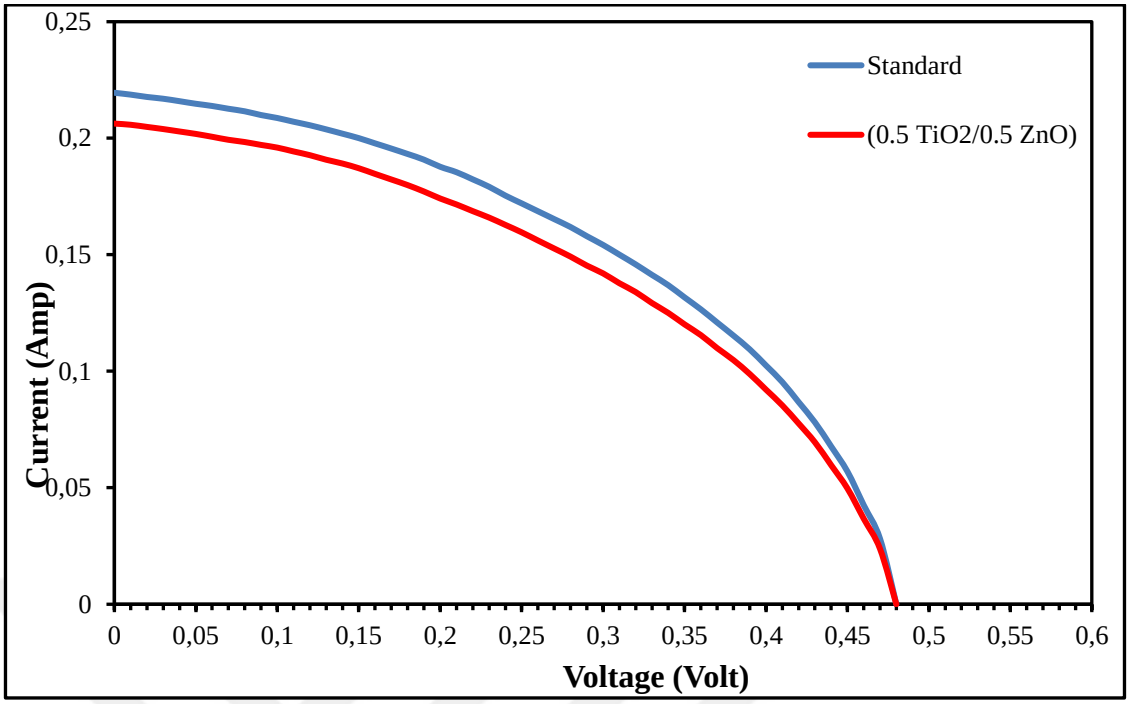

Figure 4.26 I-V characteristics curve of $0.5TiO_2/0.5ZnO$/a-Si compared to a-Si

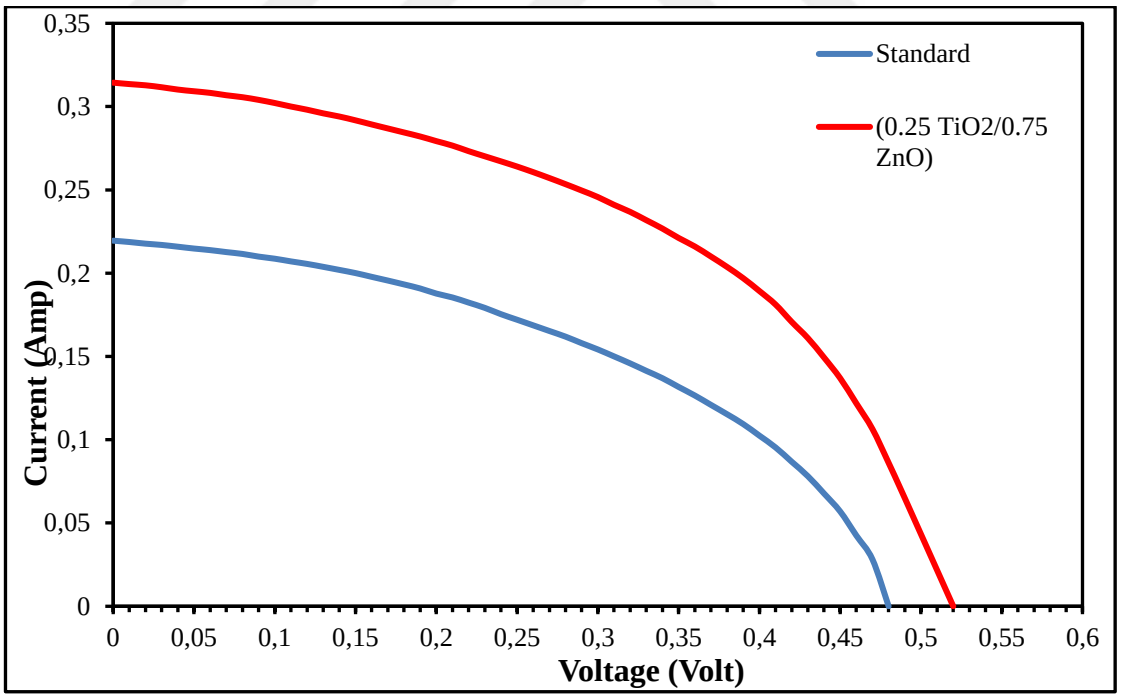

Figure 4.27 I-V characteristics curve of $0.25TiO_2/0.75ZnO$/a-Si compared to a-Si

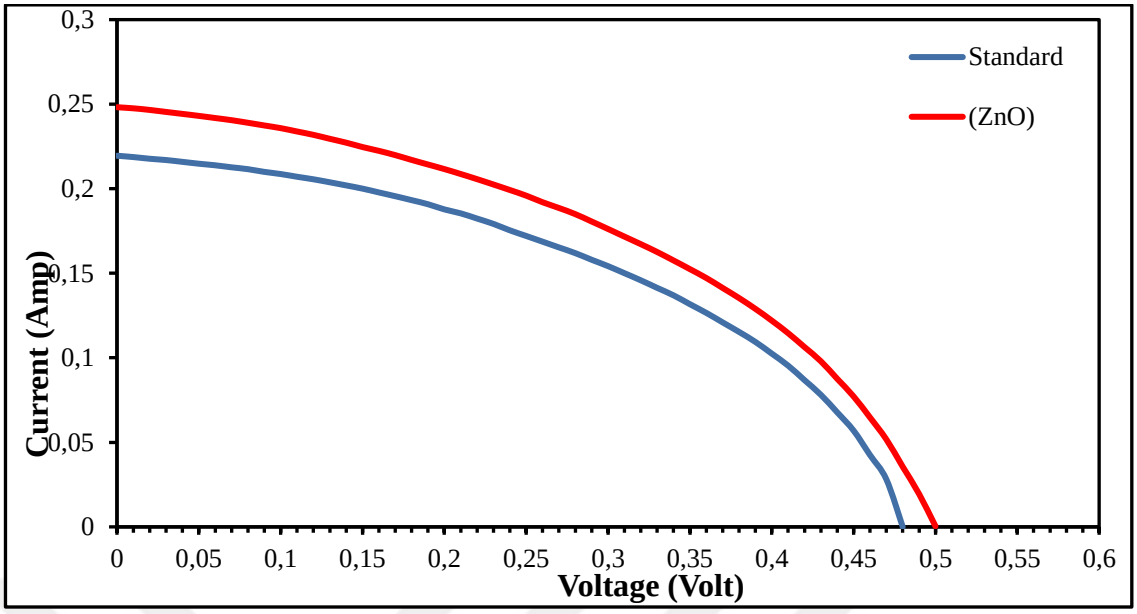

Figure 4.28 I-V characteristics curve of ZnO/a-Si compared to a-Si

Figures 4.24-4.28 show the I-V characteristics curve of TiO_2, ZnO and TiO_2/ZnO/a-Si compared to a-Si, and their efficiencies are listed in Table 4.4. As can be seen from Figure 4.24 to 4.28, both the standard and the film coated solar cells have almost the similar voltage reading. In fact, higher voltage reading was recorded for the $0.75TiO_2/0.25ZnO$ composite sample and the $0.25TiO_2/0.75ZnO$ composite sample with a prominent difference of about 0.03 V and 0.04 V, respectively, indicating that the self-cleaning coating did not deteriorate the performance of the solar cell.

Solar cell efficiency has unsystematic behavior with increasing concentration of ZnO content in TiO_2/ZnO composite (Table 4.4). However, the optimum TiO_2/ZnO weight ratio was found out to be 0.25/0.75 wt./wt. because this sample had minimal reflection and high transparency in the visible light range especially between 400-600 nm. Higher energy gap and lower refractive index allow to absorb more light in the UV-visible range. In addition, the specified composite sample exhibited low dielectric constant and extinction coefficient values in the visible light region of 400-600 nm. The improvement in the solar cell efficiency might be attributed to the fact that little amount of the visible radiation was absorbed by the TiO_2/ZnO composite sample, whereas this film absorbed the UV range of incident light. Combining the metal oxide with another

metal oxide increases the solar cell efficiency, because combining the two semiconductors can increase the total internal reflection, leading to an increase in the solar cell efficiency. The TiO_2/ZnO film acted as Luminescent Solar Concentrators (LSC).

The fill factor is also an important factor exhibiting the solar cell efficiency. The fill factor is mainly affected by the cell's resistances and diode losses. In particular, the series and shunt resistances of the cell are important factors that determine the output power of the cell. Any effect that increases the shunt resistance and decreases the series resistance results in a higher fill factor and solar cell efficiency (Green 2016). According to Table 4.4, higher fill factor value was obtained with the ZnO film, the $0.75TiO_2$/0.25ZnO composite film and the $0.25TiO_2$/0.75ZnO composite film compared to uncoated solar cell, exhibiting the efficiency of the coated film in terms of the solar cell efficiency.

Table 4.4 Solar cells efficiency

Sample	**V_m (V)**	**I_m (A)**	**V_{oc}**	**I_{sc}**	**F.F**	**A (m^2)**	**J_m**	**P_{out} (W/m^2)**	**P_{in} (W/m^2)**	**η**
Standard	0.27	0.165	0.49	0.219	0.415	0.0007	236	63.75	1000	6.375
TiO_2	0.29	0.151	0.5	0.224	0.391	0.0007	215.965	62.630	1000	6.263
$0.75TiO_2$/0.25ZnO	0.29	0.203	0.5	0.267	0.442	0.0007	290	84.422	1000	8.422
$0.50TiO_2$/0.50ZnO	0.27	0.153	0.49	0.206	0.408	0.0007	218.078	58.881	1000	5.888
$0.25TiO_2$/0.75ZnO	0.3	0.246	0.5	0.314	0.469	0.0007	350.978	105.293	1000	10.529
ZnO	0.29	0.181	0.5	0.248	0.422	0.0007	258	74.81	1000	7.481

The prepared films have multifunctionality, especially the $0.25TiO_2$/0.75ZnO composite film, i.e. the self-cleaning properties imparted to it due to hydrophilicity, which helps to solve the problem of dust accumulation and ARCs on the photovoltaic cell and primarily helps to reduce reflection loss. As well as, the prepared composite film acts as Luminescent Solar Concentrators (LSC).

5. CONCLUSIONS

1. The titanium dioxide (TiO_2) and zinc oxide (ZnO) nanoparticles were successfully synthesized using sol-gel techniques.
2. The X-Ray diffraction spectrum of TiO_2 and ZnO films patterns showed the same peaks as standard cards for TiO_2 and ZnO powders, which means that the preparation method and the film coating technique do not affect the crystal structure of the materials.
3. FTIR study indicate the functional groups and all bonds of synthesized TiO_2, ZnO NPs and TiO_2/ZnO films with varying ZnO content.
4. Field emission scanning electron microscopy (FESEM) showed that the TiO_2 particles were larger than the ZnO particles, this made the ZnO film appear smoother than the TiO_2 film. Since the small particles of ZnO close the pores of TiO_2 film, the composite film appeared more smoother, which indicated the good results of mixing these two nanoparticles.
5. The effect of the ZnO content of the composite films on the optical properties was investigated. The TiO_2 film and the $0.75TiO_2/0.25ZnO$ composite film exhibited indirect band gap transition while the ZnO film, the $0.5TiO_2/0.5ZnO$ composite film and the $0.25TiO_2/0.75ZnO$ composite film showed direct band gap transition. The optical energy gap exhibited non-systematic variation with the ZnO content.
6. In contact angle measurement with different UV irradiation time periods, the zero angles were approached after 15 minutes, and the super-hydrophilicity property was obtained. These results are very important and convenient in terms of self-cleaning and photocatalytic effect.
7. The optimum value of the sliding angle was obtained with the $0.25TiO_2/0.75ZnO$ composite film sample.
8. When compared with a-Si solar cell efficiency (6.375), the best efficiency (10.529) was obtained by the solar cell coated with the $0.25TiO_2/0.75ZnO$ composite film.

5.1 Suggestions for Future Work

1. Study the effect of film thickness of the $0.25TiO_2/0.75ZnO$ composite sample on the self-cleaning activity and solar cell efficiency.
2. Study the use of TiO_2/ZnO composites in photocatalytic removal of trace metals ions from wastewater.
3. Combining TiO_2/ZnO with organic additives could promise the stability of the synthesized particles and increase the efficiency of self-cleaning under visible light.

REFERENCES

Abazovic, N. D., Čomor, M. I., Dramićanin, M. D., Jovanović, D.J., Ahrenkiel, S. P. and Nedeljković, J. M. 2006. Photoluminescence of anatase and rutile TiO2 particles. The Journal of Physical Chemistry B, 110(50), 25366-25370.

Abdelraheem, W. H. M., Patil, M. K., Nadagouda, M. N. and Dionysiou, D. D. 2019. Hydrothermal synthesis of photoactive nitrogen- and boron- codoped TiO2 nanoparticles for the treatment of bisphenol A in wastewater: Synthesis, photocatalytic activity, degradation byproducts and reaction pathways. Applied Catalysis B: Environmental, 241(598), 598-611.

Abdulaziz, A., Alarifi, I. M., Khan W. S. and Asmatulu, R. 2016. Highly Hydrophilic Electrospun Polyacrylonitrile/ Polyvinypyrrolidone Nanofibers Incorporated with Gentamicin as Filter Medium for Dam Water and Wastewater Treatment. Journal of Membrane and Separation Technology 5, 38-56.

Abdullah, H., Khan, M. M. R., Ong, H. R. and Yaakob, Z. 2017. Modified TiO2 photocatalyst for CO2 photocatalytic reduction: an overview. Journal of CO2 Utilization, 22, 15-32.

Acayanka, E., Tarkwa, J. B., Nchimi, K. N., Voufouo, S. A., Tiya-Djowe, A., Kamgang, G. Y. and Laminsi, S. 2019. Grafting of N-doped titania nanoparticles synthesized by the plasma-assisted method on textile surface for sunlight photocatalytic self-cleaning applications. Surfaces and Interfaces, 17, 100361.

Agbe, H., Nyankson, E., Raza, N., Dodoo-Arhin, D., Chauhan, A., Osei, G. Kumar, V. and Kim, K. H. 2019. Recent advances in photoinduced catalysis for water splitting and environmental applications. Journal of Industrial and Engineering Chemistry, 72, 31-49.

Ahmad, D., Boogaert, I., Miller, J., Presswell, R. and Jouhara, H. 2018. Hydrophilic and hydrophobic materials and their applications. Energy Sources, Part A: Recovery, Utilization, and Environmental Effects, 40(22), 2686-2725.

Akın, S. and Sönmezoğlu, S., 2012. Nanostructured TiO2 thin films: synthesis and characterisations. Materials Technology, 27(5), pp.342-349.

Amir, R. M., Anjum, F. M., Khan, M. I., Khan, M. R., Pasha, I. and Nadeem, M. 2013. Application of Fourier transform infrared (FTIR) spectroscopy for the identification of wheat varieties. Journal of food science and technology, 50, 1018-1023.

Anonymous. 2023a. Web Sitesi: https://www.pdhengineer.com/courses/r/M-4016.pdf, Erişim Tarihi: 15.01.2023.

Anonymous. 2023b. Web Sitesi: https://kipdf.com/photovoltaic-solar-energy-generation_5ac855041723dd7c32229036.html, Erişim Tarihi: 18.01.2023.

Anonymous. 2023c. Web Sitesi: https://energy-models.com/basic-photovoltaic-principles-and-methods, Erişim Tarihi: 25.01.2023.

Anonymous. 2023d. Web Sitesi: https://pubmed.ncbi.nlm.nih.gov/31067802/, Erişim Tarihi: 02.02.2023.

Anonymous. 2023d. Web Sitesi: https://pubmed.ncbi.nlm.nih.gov/31067802/, Erişim Tarihi: 10.02.2023.

Appasamy, J. S., Kurnia, J. C., Assadi, M. K. 2020. Synthesis and evaluation of nitrogen-doped titanium dioxide/single walled carbon nanotube-based hydrophilic self-cleaning coating layer for solar photovoltaic panel surface. Solar Energy, 196, 80-91.

Ayati, A., Ahmadpour, A., Bamoharram, F. F., Tanhaei, B., Mänttäri, M. and Sillanpää, M. 2014. A review on catalytic applications of Au/TiO2 nanoparticles in the removal of water pollutant. Chemosphere 107, 163-174.

Barakat, M. A. and Kumar, R. 2016. Photocatalytic Activity Enhancement of Titanium Dioxide Nanoparticles: Degradation of Pollutants in Wastewate, In Springer Briefs in Green Chemistry for Sustainability. Sharma, S. K. (ed), Springer, 1-23, New York.

Barshilia, H. C., Tej, K. S., Devi, L. M. and Rajam, K. S. 2010. Nanometric multiscale rough Zn–ZnO superhydrophobic thin films: Self-diffusion of zinc and effect of UV irradiation. Journal of Applied Physics, 108(7), 074315.

Barthlott, W. and Neinhuis, C. 1997 Purity of the Sacred Lotus, or Escape from Contamination in Biological Surfaces. Planta, 202, 1-8

Bhandari, A., Panwar, N. S. 2021. Optical properties of [Ta2O5](1-x)[TiO2](x,) (x=0.08) thin films. Ferroelectrics Letters Section, 48(1-3), 20-30.

Bhange, P. D., Awate, S. V., Gholap, R. S., Gokavi, G. S. and Bhange, D. S. 2016. Photocatalytic degradation of methylene blue on Sn-doped titania nanoparticles synthesized by solution combustion route. Materials Research Bulletin, 76, 264-272.

Binas, V., Stefanopoulos, V., Kiriakidis, G. and Papagiannakopoulos, P. 2019. Photocatalytic oxidation of gaseous benzene, toluene and xylene under UV and visible irradiation over Mn-doped TiO2 nanoparticles. Journal of Materiomics, 5(1), 56-65.

Boningari, T., Inturi, S. N. R., Suidan, M. and Smirniotis, P. G. 2018. Novel one-step synthesis of sulfur doped-TiO2 by flame spray pyrolysis for visible light photocatalytic degradation of acetaldehyde. Chemical Engineering Journal, 339, 249-258.

Brendel, R. 2003. Thin-Film Crystalline Silicon Solar Cells, Physics and Technology. Wiley, Mörlenbach, Germany.

Bumajdad, A. and Madkour, M. 2014. Understanding the superior photocatalytic activity of noble metals modified titania under UV and visible light irradiation. Physical Chemistry Chemical Physics, 16(16), 7146-7158.

Burns, G. 1985. Solid State Physics, Academic Press, 755, New York.

Chapin, D. M., Fuller, C. S. and Pearson, G. L. 1954. A New Silicon P-N Junction Photocell for Converting Solar Radiation into Electrical Power. Journal of Applied Physics, 8, 676.

Chen, S. F., Zhao, W., Liu, W. and Zhang, S. J. 2008. Preparation, characterization and activity evaluation of p-n junction photocatalyst p-ZnO/n-TiO2. Applied Surface Science, 255(5), 2478-2484.

Chen, S. F., Zhao, W., Liu, W., Zhang and S. J. 2009. Preparation, characterization and activity evaluation of p-n junction photocatalyst p-NiO/n-ZnO. Journal of Sol-Gel Science and Technology, 50, 387-396.

Chen, Y. W. and Hsu, Y. H., 2021. Effects of reaction temperature on the photocatalytic activity of TiO2 with Pd and Cu cocatalysts. Catalysts, 11(8), 966.

Cho, S. and Choi, W. 2001. Solid-phase photocatalytic degradation of PVC–TiO2 polymer composites. Journal of Photochemistry and Photobiology A: Chemistry, 143(2-3), 221-228.

Chopra, K. 1969. Thin Film Phenomena, Mc Graw-Hill, 736, NewYork.

Clark, P. E., Curtis, S. A.; Minetto, F. A. and Keller, J. 2007. Finding a dust mitigation strategy that works on the lunar surface, 38th Lunar and Planetary Science Conference, 12-16 March, 1175, League City, Texas.

Cuerda-Correa, E. M., Alexandre-Franco and M. F., Fernández-González, C. 2020. Advanced oxidation processes for the removal of antibiotics from water. An overview. Water, 12(1), 102.

Deng, Q. R., Xia, X. H., Guo, M. L., Gao, Y. and Shao, G. 2011. Mn-doped TiO2 nanopowders with remarkable visible light photocatalytic activity. Materials Letters, 65(13), 2051-2054.

Desai, R., Gupta, S. K., Mishra, S., Jha, P. K. and Pratap, A. 2011. The synthesis of TiO2 nanoparticles by wet-chemical method and their photoluminescence, thermal and vibrational characterizations: effect of growth condition. International Journal of Nanoscience, 10(06), 1249-1256.

Devi, L. G. and Kavitha, R. 2013. A review on non metal ion doped titania for the photocatalytic degradation of organic pollutants under UV/solar light: Role of photogenerated charge carrier dynamics in enhancing the activity. Applied Catalysis B: Environmental, 140, 559-587.

Devi, L. G. and Kavitha, R. J. M. C. 2014. Enhanced photocatalytic activity of sulfur doped TiO2 for the decomposition of phenol: a new insight into the bulk and surface modification. Materials Chemistry and Physics, 143(3), 1300-1308.

Dietze, E. C., Keller, W., Muhlbauer, W., Dietl, A., Helmreich, J., Sirtl, D. 1981. Crystals: Growth, Properties and Applications. Vol. 5, Springer, 57.

Elliot, R. and Gibson, A. I. 1974. An Introduction to Solid State Physics and Application, Macillian Inc., 490, London.

Elminir, H. K., Ghitas, A. E., Hamid, R. H., El-Hussairly, F., Beheary, M. M. and Abdel-Moneim, K. M. 2006. Effect of dust on the transparent cover of solar collectors. Energy Conversion and Management, 47(18-19), 3192-3203.

Feng, X., Wang, P., Hou, J., Qian, J., Ao, Y. and Wang, C. 2018. Significantly enhanced visible light photocatalytic efficiency of phosphorus doped TiO2 with

surface oxygen vacancies for ciprofloxacin degradation: Synergistic effect and intermediates analysis. Journal of hazardous materials, 351, 196-205.

Firdaus, C.M., Rizam, M.S., Rusop, M. and Hidayah, S.R. 2012. Characterization of ZnO and ZnO: TiO2 thin films prepared by sol-gel spray-spin coating technique. Procedia Engineering, 41, 1367-1373.

Foster, H. A., Ditta, I. B., Varghese, S. and Steele, A. 2011. Photocatalytic disinfection using titanium dioxide: spectrum and mechanism of antimicrobial activity. Applied Microbiology and Biotechnology, 90(6), 1847-1868.

Fujishima, A., Rao, T. N., Tryk, D. A. 2000. Titanium dioxide photocatalysis. Journal of photochemistry and photobiology C: Photochemistry reviews, 1(1), 1-21.

Gaier, J., Davis P. and Marabito M. 1990. Aeolian removal of dust types from photovoltaic surfaces on Mars, 16th AIAA/NASA/ASTM/IES Space Simulation Conference, Albuquerque.

Gaier, J. and Davis, P. 1992. Effect of particle size of Martian dust on the degradation of photovoltaic cell performance, International Solar Energy Conference, 4-8 April, Maui, Hawaii.

Ganesan, P., Vanaki, S. M., Thoo, K. K. and Chin, W. M. 2016. Air-side heat transfer characteristics of hydrophobic and super-hydrophobic fin surfaces in heat exchangers: A review. International Communications in Heat and Mass Transfer, 74, 27-35.

Ganesh, I., Gupta, A. K., Kumar, P. P., P. S. Chandra, S. K., Radha, K., Padmanabham, G., Sundararajan, G. 2012. Preparation and characterization of Co-doped TiO2 materials for solar light induced current and photocatalytic applications. Materials Chemistry and Physics, 135(1), 220-234.

Garip, Ş. 2005. The Characterization of Bacteria with Fourier Transform Infrared (FTIR) Spectroscopy. Msc Thesis, Middle East Technical University, The Graduate School of Natural and Applied Sciences, Biology, 83, Ankara.

Goetzberger, A. and Hoffmann, V. U. 2005. Photovoltaic Solar Energy Generation. Springer, New York.

Green, M. A. 2016. Accurate expressions for solar cell fill factors including series and shunt resistances. Applied physics letters, 108(8), 081111.

Grenier, R. 1961. Semiconductor Device, Electronic Energy Series, McGraw-Hill, London, 99-101.

Gul, S. R., Khan, M., Wu, B. and Yi, Z. 2017. Combined experimental and theoretical study of visible light active P doped TiO2 photocatalyst. Materials Research Express, 4(6), 065502.

Guo, S., Han, S., Haifeng, M., Zeng, C., Sun, Y., Chi, B., Pu, J. and Li, J. 2013. Synthesis of phosphorus-doped titania with mesoporous structure and excellent photocatalytic activity. Materials Research Buletin 48(9), 3032-3036.

Haider, A. J., Alhaddad, R. M. S. and Yahya, K. Z. 2011. Nanostructure Dopants TiO2 Films for Gas Sensing. Iraqi Journal of Applied Physics., 7(2), 27-31.

Hamza, M. A., Khalil, A.S. and Yaseen, H. M., 2013. Synthesis of Yb 3+ Doped TiO 2 Nano Particles Powder as IR Filter via Sol-Gel. Advances in Materials Physics and Chemistry, 2013.

Han, J. K., Choi, S. M., Lee, G. H. 2007. Synthesis and photocatalytic activity of nanocrystalline TiO2-SrO composite powders under visible light irradiation. Materials Letters, 61(18), 3798-3801.

Han, F., Kambala, V. S. R., Dharmarajan, R., Liu, Y. and Naidu, R. 2018. Photocatalytic degradation of azo dye acid orange 7 using different light sources over Fe3+-doped TiO2 nanocatalysts. Environmental Technology & Innovation, 12, 27-42.

Han, R., Liu, J., Chen, N., Wang, G., Guo, Y. and Wang, H. 2019. Synthesis of V-modified TiO2 nanorod-aggregates by a facile microwave-assisted hydrothermal process and photocatalytic degradation towards PCP-Na under solar light. RSC advances, 9(60), 34862-34871.

Harris, D. C. and Bertolucci, M. D. 1989. Symmetry and Spectroscopy: an Introduction to Vibrational and Electronic Spectroscopy. Dover Publications, 284, New York.

He, G., Zhou, C. and Li, Z. 2011. Review of Self-Cleaning Method for Solar Cell Array. International Workshop on Automobile, Power and Energy Engineering, Procedia Engineering, 16, 640-645.

He, J., Zi, G. L., Yan, Z. Y., Li, Y. L., Xie, J., Duan, D. L., Chen, Y. J. and Wang, J. Q. 2014. Biogenic C-doped titania templated by cyanobacteria for visible-light photocatalytic degradation of Rhodamine B. Journal of Environmental Sciences, 26(5), 1195-1202.

Hersch, P., and Zweibel, K. 1982. Technical Report. Basic photovoltaic principles and methods. United States. https://doi.org/10.2172/5191389

Hinojosa–Reyes, M., Camposeco–Solis, R., Ruiz, F., Rodríguez–González, V. and Moctezuma, E. 2019. Promotional effect of metal doping on nanostructured TiO2 during the photocatalytic degradation of 4-chlorophenol and naproxen sodium as pollutants. Materials Science in Semiconductor Processing, 100, 130-139.

Hoşgün, H. L. and Aydın, M. T. A. 2019. Synthesis, characterization and photocatalytic activity of boron-doped titanium dioxide nanotubes. Journal of Molecular Structure, 1180, 676-682.

Hou, W., Liu, Z., Pavaskar, P., Hung, W. H. and Cronin, S.B. 2011. Plasmonic enhancement of photocatalytic decomposition of methyl orange under visible light. Journal of Catalysis, 277(2), 149-153.

Huang, J., Liu, S., Kuang, L., Zhao, Y., Jiang, T., Liu, S., and Xu, X. 2013. Enhanced photocatalytic activity of quantum-dot-sensitized one-dimensionally-ordered ZnO nanorod photocatalyst. Journal of Environmental Sciences, 25, 2487-2491.

Huggett, J. M. and Shaw, H. F. 1997. Field emission scanning electron microscopy—a high-resolution technique for the study of clay minerals in sediments. Clay Minerals, 32(2), 197-203.

Hull, A. W. 1919. A new method of chemical analysis. Journal of the American Chemical Society, 41(8), 1168-1175.

Ismael, M. 2020. Enhanced photocatalytic hydrogen production and degradation of organic pollutants from Fe (III) doped TiO2 nanoparticles. Journal of Environmental Chemical Engineering, 8(2), 103676.

Ismail, M. A., Taha, K. K., Modwi, A. and Khezami, L. 2018. ZnO nanoparticles: Surface and X-ray profile analysis. J. Ovonic Res, 14(5), 381-393.

Jenei, I. Z. 2012. Scanning electron microscopy (SEM) analysis of tribofilms enhanced by fullerene-like nanoparticles. PhD Thesis, Department of Physics, Stockholm University, Stockholm, Sweden.

Jenkins, T.E. 1995. Semiconductor science: growth and characterization techniques. Prentice-Hall, Inc.

Kaech, A. 2013. An Introduction to Electron Microscopy Instrumentation. Imaging and Preparation. Zurich: Center for Microscopy and Image Analysis, University of Zurich.

Kaschner, A., Haboeck, U., Strassburg, M., Strassburg, M., Kaczmarczyk, G., Hoffmann, A., Thomsen, C., Zeuner, A., Alves, H.R., Hofmann, D.M. and Meyer, B.K. 2002. Nitrogen-related local vibrational modes in ZnO: N. Applied Physics Letters, 80(11), 1909-1911.

Kazmarski, L. L. 1980. Polycrystalline and amorphouse thin films and device, Academic Press, 297, New York.

Khan, M., Cao, W. 2013. Cationic (V, Y)-codoped TiO2 with enhanced visible light induced photocatalytic activity: A combined experimental and theoretical study. Journal of Applied Physics, 114(18), 183514.

Khan, M. Z. H., Das, P. P. and Abdullah, M. 2020. One step synthesis of ZnO nanoparticles with zinc acetate dehydrates and potassium. International Journal of Nanomanufacturing, 16(1), 89-96.

Khan, S. H. and Yadav, V. K. 2021. Advanced Oxidation Processes for Wastewater Remediation: An Overview, In: Removal of Emerging Contaminants Through Microbial Processes. Springer, Singapore.

Khan, S. B., Irfan, S., Zhuanghao, Z. and Lee, S. L. 2019. Influence of refractive index on antireflectance efficiency of thin films. Materials, 12(9), 1483.

Klaysri, R., Ratova, M., Praserthdam, P. and Kelly, P.J. 2017. Deposition of visible light-active C-doped titania films via magnetron sputtering using CO2 as a source of carbon. Nanomaterials, 7(5), 113.

Koerkamp, P. G., Metz, J. H. M., Uenk, G. H., Phillips, V. R., Holden, M. R., Sneath, R. W., Short, J. L., White, R. P. P., Hartung, J., Seedorf, J. and Schröder, M. 1998. Concentrations and emissions of ammonia in livestock buildings in Northern Europe. Journal of Agricultural Engineering Research, 70(1), 79-95.

Kohno, Y., Hayashi, H., Takenaka, S., Tanaka, T., Funabiki, T. and Yoshida, S., 1999. Photo-enhanced reduction of carbon dioxide with hydrogen over Rh/TiO2.

Journal of Photochemistry and photobiology A: Chemistry, 126(1-3), pp.117-123.

Kotani, Y., Matoda, T., Matsuda, A., Kogure, T., Tatsumisago, M. and Minami, T. 2001. Anatase nanocrystaldispersed thin films via sol–gel process with hot water treatment: effects of poly(ethylene glycol) addition on photocatalytic activities of the films. Journal of Materials Chemistry, 11(8), 2045-2048.

König, B. 2013. Chemical Photocatalysis. De Gruyter, Berlin.

Kumaravel, V., Mathew, S., Bartlett, J. and Pillai, S.C., 2019. Photocatalytic hydrogen production using metal doped TiO2: A review of recent advances. Applied Catalysis B: Environmental, 244, 1021-1064.

Kuvarega, A. T., Krause, R. W. and Mamba, B. B. 2014. Comparison between base metals and platinum group metals in nitrogen, M codoped TiO2 (M= Fe, Cu, Pd, Os) for photocatalytic removal of an organic dye in water. Journal of Nanomaterials, 2014, 199-199.

Kwon, Y. G., Choi, S. Y., Kang, E. S. and Baek, S. S. 2000. Ambient-dried silica aerogel doped with TiO2 powder for thermal insulation. Journal of materials science, 35, 6075-6079.

Lansel, S. 2010. Technology and Future of III-V Multi-Junction Solar Cells. Iraqi Journal of Applied Physics, 6(3), 1-6.

Lee, D. H., Swain, B., Shin, D., Ahn, N. K., Park, J. R. and Park, K. S. 2019. One-pot wet chemical synthesis of fluorine-containing TiO2 nanoparticles with enhanced photocatalytic activity. Materials Research Bulletin, 109, 227-232.

Lee, J. H., Youn, J. I., Kim, Y. J., Kim, I. K., Jang, K. W. and Oh, H. J. 2015. Photocatalytic characteristics of boron and nitrogen doped titania film synthesized by micro-arc oxidation. Ceramics International, 41(9), 11899-11907.

Liao, S., Huang, D., Yu, D. G., Yu D. H., Su, Y. L. and Yuan, G. Q. 2004 Preparation and characterization of ZnO/TiO2, SO42-/ZnO/TiO2 photocatalyst and their photocatalysis. Journal of Photochemistry and Photobiology A-Chemistry, 168(1-2), 7-13.

Livage, J., Henry M. and Sanchez C. 1988. Sol-gel chemistry of transition metal oxides. Progress in Solid State Chemistry, 18(4) 259-342.

Manojkumar, P., Lokeshkumar, E., Saikiran, A., Govardhanan, B., Ashok, M. and Rameshbabu, N. 2020. Visible light photocatalytic activity of metal (Mo/V/W) doped porous TiO2 coating fabricated on Cp-Ti by plasma electrolytic oxidation. Journal of Alloys and Compounds, 825, 154092.

Marci, G., Augugliaro, V., Lopez-Munoz, M. J., Martin, C., Palmisano, L., Rives, V., Schiavello, M., Tilley, R. J. and Venezia, A. M. 2001. Preparation characterization and photocatalytic activity of polycrystalline ZnO/TiO2 systems. 2. surface, bulk characterization, and 4-nitrophenol photodegradation in liquid− solid regime. The Journal of Physical Chemistry B, 105(5), 1033-1040.

Marques, J., Gomes, T. D., Forte, M. A., Silva, R. F. and Tavares, C. J. 2019. A new route for the synthesis of highly-active N-doped TiO2 nanoparticles for visible light photocatalysis using urea as nitrogen precursor. Catalysis Today, 326, 36-45.

Martemucci, G., Costagliola, C., Mariano, M., D'andrea, L., Napolitano, P. and D'Alessandro, A. G. 2022. Free Radical Properties, Source and Targets, Antioxidant Consumption and Health. Oxygen, 2, 48-78.

Matsunaga, T., Tomoda, R., Nakajima, T. and Wake, H. 1985. Photoelectrochemical sterilization of microbial cells by semiconductor powders FEMS. Microbiology Letters, 29(1-2), 211-214.

Mazumder, M. K., Sharma, R., Biris, A. S., Zhang, J., Calle, C. and Zahn, M. 2007. Self-cleaning transparent dust shields for protecting solar panels and other devices. Particulate Science and Technology, 25(1), 5-20.

McMurry, J. 2003. Organic chemistry with Biological applications. Brooks and Cole Pub. Co., Stamford, U.S.A.

Millman, J. 1979. Microelectronics, McGraw Hill, 881, Japan.

Mills, A. and LeHunte, S. 1997. An overview of semiconductor photocatalysis. Journal of Photochemistry and Photobiology A: Chemistry, 108(1), 1-35.

Mishra, N., Reddy, R., Kuila, A., Rani, A., Nawaz, A. and Pichiah, S. 2017. A review on advanced oxidation processes for effective water treatment. Current World Environment, 12(3), 469-489.

Miwa, M., Nakajima, A., Fujishima, A., Hashimoto, K., Watanabe, T. 2000. Effects of the Surface Roughness on Sliding Angles of Water Droplets on Superhydrophobic Surfaces. Langmuir, 16(13), 5754-5760.

Modanlu, S. and Shafiekhani, A. 2019. Synthesis of pure and C/S/N co-doped Titania on Al mesh and their photocatalytic usage in Benzene degradation. Scientific Reports, 9(1), 16648.

Mohamed, S. H., El-Hagary, M., Althoyaib, S. 2013. Growth of undoped and Fe doped TiO2 nanostructures and their optical and photocatalytic properties. Applied Physics A-Materials Science & Processing, 111(4), 1207-1212.

Mohseni-Salehi, M. S., Taheri-Nassaj, E. and Hosseini-Zori, M. 2018. Effect of dopant (Co, Ni) concentration and hydroxyapatite compositing on photocatalytic activity of titania towards dye degradation. Journal of Photochemistry and Photobiology A: Chemistry, 356, 57-70.

Mohsin, A. K. 2020. Preparation TiO2 and ZnO/TiO2 nanocomposites locally and use against Staphylococcus aureus. In IOP Conference Series: Materials Science and Engineering, Vol 928, No. 7, 072014.

Mugundan, S., Rajamannan, B., Viruthagiri, G., Shanmugam, N., Gobi, R. and Praveen, P. 2015. Synthesis and characterization of undoped and cobalt-doped TiO2 nanoparticles via sol–gel technique. Applied Nanoscience, 5, 449-456.

Muraca, A. P., Kershis, M. D., Camillone, N. and White, M. G. 2019. Ultrafast dynamics of acetone photooxidation on TiO2(110). Journal of Chemical Physics, 151(16), 161103.

Nakayama, K., Tanabe, K. and Atwater, H. A. 2008. Improved electrical properties of wafer-bonded p-GaAs/n-InPinterfaces with sulfide passivation. Journal of Applied Physics, 103(9), 094503(1-5).

Nanaji, K., Janardhana, R. K. S. K., Rao, T. N. and Anandan, S. 2019. Energy level matching for efficient charge transfer in Ag doped-Ag modified TiO2 for enhanced visible light photocatalytic activity. Journal of Alloys and Compounds, 794, 662-671.

Niu, J., Dai, P., Qi, G., Zhang, Q., Yao, B., Yu, X. and Liu, C. 2016. Preparation of P doped TiO2 nanotubes and its photocatalytic activity. Integrated Ferroelectrics, 176(1), 150-159.

Noorjahan, M., Kumari, V. D., Subrahmanyam, M. and Boule, P. 2004. A novel and efficient photocatalyst: TiO2- HZSM-5 combinate thin film. Applied Catalysis B: Environental, 47, 209-213.

Nyamukamba, P. 2011. Preparation of photocatalytic TiO2 nanoparticles immobilized on carbon nanofibres for water purification. MSc Thesis, University of Fort Hare, Faculty of Science and Agriculture, Chemistry, 149, Alice, South Africa.

O'Regan, B. and Grätzel, M. 1991. A low-cost, high-efficiency solar cell based on dye-sensitized colloidal TiO2 films. Nature 353, 737-740.

Oliveira, A. S., Kaizer, M. R., Azevedo, M. S., Ogliari, F. A., Cenci, M. S. and Moraes, R. R. 2015. (Super)hydrophobic coating of orthodontic dental devices and reduction of early oral biofilm retention. Biomedical Materials 10, 65004.

Oros-Ruiz, S., Gómez, R., López, R., Hernandez-Gordillo, A., Pedraza-Avella, J. A., Moctezuma, E. and Pérez, E. 2012. Photocatalytic reduction of methyl orange on Au/TiO2 semiconductors. Catalysis Communications, 21, 72-76.

Osin, O. A., Yu, T., Cai, X., Jiang, Y., Peng, G., Cheng, X., Li, R., Qin, Y. and Lin, S. 2018. Photocatalytic degradation of 4-nitrophenol by C, N-TiO2: Degradation efficiency vs. embryonic toxicity of the resulting compounds. Frontiers in Chemistry, 6, 192.

Ovodok, E., Maltanava, H., Poznyak, S., Ivanovskaya, M., Kudlash, A., Scharnagl, N. and Tedim, J. 2018. Sol-gel template synthesis of mesoporous carbon-doped TiO2 with photocatalytic activity under visible light. Materials Today: Proceedings, 5(9), 17422-17430.

Pan, T. C., Wang, S. H., Lai, Y. S., Jehng, J. M. and Huang, S. J. 2014. Study of the silver modified TiO2 nanotube array applied to hydrogen evolution. Applied surface science, 296, 189-194.

Pankove, J. I. 1971. Optical Processes in Semiconductors, Dover Puplication Inc., 448, New York.

Pawley, J. B. 1997. The development of field-emission scanning electron microscopy for imaging biological surfaces. Scanning-New York and Baden Baden Then Mahwah-, 19, 324-336.

Pecharsky, V. K. and Zavalij, P. Y. 2009. The powder diffraction pattern. Fundamentals of Powder Diffraction and Structural Characterization of Materials, 151-202.

Pei, L. Z., Wei, T., Lin, N. and Yu, H. Y. 2016. Synthesis of zinc oxide and titanium dioxide composite nanorods and their photocatalytic properties. Advanced Composites Letters, 25(1), 096369351602500102.

Peierls, R. and Peierls, R. E. 1955. Quantum theory of solids. Oxford University Press.

Tanaka, Y. and Matsuo, K. 2011. Non-Thermal Effects of Near-Infrared Irradiation on Melanoma, In: Breakthroughs in Melanoma Research. Tanaka, Y. (ed), InTechOpen, 29-63.

Pintilie, S. C., Tiron, L. G., Lazar, A. L., Vlad, M., Birsan, I. G. and Balta, S. 2018. The Influence of ZnO/TiO. Materiale Plastice, 55(1), 54.

Qu, X. F., Xie, D. D., Cao, L. X. and Du, F. L. 2014. Synthesis and characterization of TiO2/ZrO2 coaxial core-shell composite nanotubes for photocatalytic applications. Ceramics International, 40(8), 12647-12653.

Quesada-Cabrera, R., Sotelo-Vázquez, C., Quesada-González, M., Melián, E. P., Chadwick, N. and Parkin, I. P. 2017. On the apparent visible-light and enhanced UV-light photocatalytic activity of nitrogen-doped TiO2 thin films. Journal of Photochemistry and Photobiology A: Chemistry, 333, 49-55.

Rahimi, N., Pax, R. A. and Gray, E. M. 2016. Review of functional titanium oxides. I: TiO2 and its modifications. Progress in Solid State Chemistry, 44(3), 86-105.

Ramkumar, J., Kumar, L. P., Sivakumar, N., Pandiarajan, A. and Dheendayalan, M. 2018. Synthesis and Characterization of Silver Nanoparticles Using Leaf Extract of "Sansevieria Roxburghiana" and its Application of Water Treatment. - International Journal of Research and Analytical Reviews. 5(4), 195-203.

Ratova, M., Klaysri, R., Praserthdam, P. and Kelly, P. J. 2018. Visible light active photocatalytic C-doped titanium dioxide films deposited via reactive pulsed DC magnetron co-sputtering: Properties and photocatalytic activity. Vacuum, 149, 214-224.

Ray, B. 1969. II-VI Compounds, Pergamon Press, 268, Edinburgh, Great Britain.

Retnaningsih, L. and Muliani, L. 2016, April. The result of synthesis analysis of the powder TiO2/ZnO as a layer of electrodes for dye sensitized solar cell applications. In AIP Conference Proceedings, Vol. 1725, No. 1, 020069.

Richards, B. S., Cotter, J. E., Honsberg, C. B. and Wenham, S. R. 2000. Novel uses of TiO/sub 2/in crystalline silicon solar cells. In Conference Record of the Twenty-Eighth IEEE Photovoltaic Specialists Conference-2000, 375-378).

Rodriguez, M. P. Q. 2000. Fourier transform infrared (FTIR) technology for the identification of organisms. Clinical Microbiology Newsletter, 22(8), 57-61.

Safari, M., Talebi, R., Rostami, M. H., Nikazar, M. and Dadvar, M. 2014. Synthesis of iron-doped TiO2 for degradation of reactive Orange16. Journal of Environmental Health Science and Engineering, 12, 1-8.

Saqib, N. U., Adnan, R. and Shah, I. 2016. A mini-review on rare earth metal-doped TiO2 for photocatalytic remediation of wastewater. Environmental Science and Pollution Research, 23, 15941-15951.

Savio, A. K. P. D., Fletcher, J. and Hernández, F. R. 2013. Sonosynthesis of nanostructured TiO2 doped with transition metals having variable bandgap. Ceramics International, 39(3), 2753-2765.

Scarisoreanu, M., Ilie, A. G., Goncearenco, E., Banici, A.M ., Morjan, I. P., Dutu, E., Tanasa, E., Fort, I., Stan, M., Mihailescu, C. N. and Fleaca, C. 2020. Ag, Au and Pt decorated TiO2 biocompatible nanospheres for UV & vis photocatalytic water treatment. Applied Surface Science, 509, 145217.

Schmidt, M., Korte, L., Laades, A., Stangl, R. and Schubert, C. H. 2007. Physical aspects of a-Si:H/c-Si hetero-junction solar cells.' Thin Solid Films, 515(19), 7475-7480.

Shinde, P. S., Sadale, S. B., Patil, P. S., Bhosale, P. N., Brüger, A., Neumann-Spallart, M. and Bhosale, C. H. 2008. Properties of spray deposited titanium dioxide thin films and their application in photoelectrocatalysis. Solar Energy Materials and Solar Cells, 92(3), 283-290.

Shindume L, H., Zhao, Z., Wang, N., Liu, H., Umar, A., Zhang, J., Wu, T. and Guo, Z. 2019. Enhanced photocatalytic activity of B, N-codoped TiO2 by a new molten nitrate process. Journal of Nanoscience and Nanotechnology, 19(2), 839-849.

Siwinska-Stefanska, K., Kubiak, A., Piasecki, A., Goscianska, J., Nowaczyk, G., Jurga, S. and Jesionowski, T. 2018. TiO2-ZnO Binary Oxide Systems: Comprehensive Characterization and Tests of Photocatalytic Activity, Materials 11(5), 841.

Slade, A. 2003. Boron Tribromide Sourced Boron Diffusions for Silicon Solar Cells. Ph.D. Thesis, UNSW Sydney, Australia.

Smestad, G. P., Germer, T. A., Alrashidi, H., Fernández, E. F., Dey, S., Brahma, H., Sarmah, N., Ghosh, A., Sellami, N., Hassan, I. A. I., Desouky, M., Kasry, A., Pesala, B., Sundaram, S., Almonacid, F., Reddy, K. S., Mallick, T. K., Micheli, L. 2020. Modelling photovoltaic soiling losses through optical characterization. Scientific Reports 10, 58.

Smirniotis, P. G., Boningari, T., Damma, D. and Inturi, S. N. R. 2018. Single-step rapid aerosol synthesis of N-doped TiO2 for enhanced visible light photocatalytic activity. Catalysis Communications, 113, 1-5.

Štengl, V., Bakardjieva, S. and Murafa, N. 2009. Preparation and photocatalytic activity of rare earth doped TiO2 nanoparticles. Materials Chemistry and Physics, 114(1), 217-226.

Subramanian, V., Wolf, E. and Kamat, P. V. 2001. Semiconductor− metal composite nanostructures. To what extent do metal nanoparticles improve the photocatalytic activity of TiO2 films?. The Journal of Physical Chemistry B, 105(46), 11439-11446.

Syafiq, A., Pandey, A. K., Adzman, N. N., Abd Rahim, N. 2018. Advances in approaches and methods for self-cleaning of solar photovoltaic panels. Solar Energy, 2018, 162, 597-619.

Thamaphat, K., Limsuwan, P. and Ngotawornchai, B. 2008. Phase characterization of TiO2 powder by XRD and TEM. Agriculture and Natural Resources, 42(5), 357-361.

Tian, J., Chen, L., Dai, J., Wang, X., Yin, Y. and Wu, P. 2009. Preparation and characterization of TiO2, ZnO, and TiO2/ZnO nanofilms via sol–gel process. Ceramics International, 35(6), 2261-2270.

Tian, J., Li, J., Wei, N., Xu, X., Cui, H. and Liu, H. 2016. Ru nanoparticles decorated TiO2 nanobelts: A heterostructure towards enhanced photocatalytic activity and gas-phase selective oxidation of benzyl alcohol. Ceramics International, 42(1), 1611-1617.

Toghan, A., Taha, K. K. and Modwi, A. 2021. TiO2–ZnO composites fabricated via sonication assisted with gelatin for potential use in Rhodamine B degradation. Journal of Materials Science: Materials in Electronics 32, 2471-2485.

Tsakalakos, L. 2012. Application of Micro- and Nanotechnology in Photovoltaics, In: Comprehensive Renewable Energy. Sayigh, A. (ed), Elsevier, 515-531.

Um, J., and Kim, S. E. 2014. Homo-Junction pn Diode Using p-Type SnO and n-Type SnO2 Thin Films. ECS Solid State Letters, 3(8), 94-98.

Wang, C. C., Chou, P. H., Yu, Y. H. and Kei, C. C. 2018a. Deposition of Ni nanoparticles on black TiO2 nanowire arrays for photoelectrochemical water splitting by atomic layer deposition. Electrochimica Acta, 284, 211-219.

Wang, F., Liang, C. H., Zhang, Y. F. and Zhang, X. S. 2017a. Defrosting performance of superhydrophobic fin-tube heat exchanger. Applied Thermal Engineering 113, 229-237.

Wang, H., Zhou, P., Wang, J., Wang, Y., Wei, J., Zhan, H., Guo, R. and Zhang, Y. 2018. Synthesis and characterization of rectorite/ZnO/TiO2 composites and their properties of adsorption and photocatalysis for the removal of methylene blue dye. Journal of Wuhan University of Technology-Mater. Sci. Ed., 33(3), 729-735.

Wang, Q. Q., Zhu, S. L., Liang, Y.Q., Cui, Z. D., Yang, X. J., Liang, C. Y. and Inoue, A. 2017b. One-step synthesis of size-controlled Br-doped TiO2 nanoparticles with enhanced visible-light photocatalytic activity. Materials Research Bulletin, 86, 248-256.

Wang, S. and Jiang, L. 2007. Definition of superhydrophobic states. Advanced Materials 19, 3423-3424.

Johansson, W., Peralta, A., Jonson, B., Anand, S., Österlund, L. and Karlsson, S. 2019. Transparent TiO2 and ZnO thin films on glass for UV protection of PV modules. Frontiers in Materials, 6, 259.

Williams, R. B., Tanimoto, R., Simonyan, A. and Fuerstenau, S. 2007. Vibration characterization of self-cleaning solar panels with piezoceramic actuation. 48th AIAA/ASME/ASCE/AHS/ASC Structures, Structural Dynamics, and Materials Conference, 23-26 April, 512-520, Honolulu, Hawaii.

Wong, M. S., Sun, D. S. and Chang, H.H. 2010. Bactericidal performance of visible-light responsive titania photocatalyst with silver nanostructures. Plos one, 5(4), e10394.

Xiong, G., Pal, U., Serrano, J. G., Ucer, K. B. and Williams, R. T. 2006. Photoluminesence and FTIR study of ZnO nanoparticles: the impurity and defect perspective. Physica Status Solidi C, 3(10), 3577-3581.

Yang, P., Wang, K., Liang, Z., Mai, W., Wang, C., Xie, W., Liu, P., Zhang, L., Cai, X., Tan, S. and Song, J. 2012. Nanoscale 4, 5755.

Yang, X., Zhu, L. Q., Zhang, Y., Chen, Y. C., Bao, B. Q., Xu, J. L., Zhou, W. W. 2014. Surface properties and self-cleaning ability of the fluorinated acrylate coatings modified with dodecafluoroheptyl methacrylate through two adding ways. Applied Surface Science, 295, 44-49.

Yu, J. G., Zhao, X. J., Chen, W. M., Lin, L., Zhang, A. L. 2001. Photocatalytic activity and hydrophilic property of TiO2/SiO2 composite nanometer thin films. Acta Physico-Chimica Sinica, 17(3), 261-264.

Zafar, Z., Ali, I., Park, S. and Kim, J.O. 2020. Effect of different iron precursors on the synthesis and photocatalytic activity of Fe–TiO2 nanotubes under visible light. Ceramics International, 46(3), 3353-3366.

Zallen, R. and Moret, M. P. 2006. The optical absorption edge of brookite TiO2. Solid State Communications, 137(3), 154-157.

Zhang, J., Xing, Z., Cui, J., Li, Z., Tan, S., Yin, J., Zou, J., Zhu, Q. and Zhou, W. 2018. C, N co-doped porous TiO 2 hollow sphere visible light photocatalysts for efficient removal of highly toxic phenolic pollutants. Dalton Transactions, 47(14), 4877-4884.

Zhao, D., Han, J. F., Cui, J. Y., Zong, X. and Li, C. 2015. A new Pb(IV)-based photocathode material Sr2PbO4 with good light harvesting ability. Journal of Materials Chemistry A, 3(22), 12051-12058.